warwick.ac.uk/lib-publications

THE BRITISH LIBRARY DOCUMENT SUPPLY CENTRE

TITLE
....
COMPTON SCATTERING STUDIES OF SPIN AND CHARGE

MOMENTUM DENSITIES

....

AUTHOR
....
David N. Timms
....

INSTITUTION
and DATE
....
University of Warwick   1989
....

....

COMPTON SCATTERING STUDIES OF SPIN AND CHARGE

MOMENTUM DENSITIES

by

David N. Timms

A thesis submitted for the degree of

Doctor of Philosophy of the University of Warwick.

Department of Physics

University of Warwick

March 1989

ABSTRACT

The ground state electron density distribution can be determined from the Doppler broadening of Compton scattered radiation. It is shown that Compton scattering of unpolarised photons leads to a measurement of the total electron momentum density distribution whereas if circularly polarised photons are used, the electron spin dependent density distribution is isolated. The experimental work reported here illustrates both techniques. Directional Compton profile measurements of an iron nickel alloy, gallium arsenide and lead have been performed with 60keV and 412keV unpolarised γ-radiation and demonstrate the sensitivity of the Compton profile and related functions to changes in the valence electron density resulting from disorder (FeNi), bonding (GaAs) and relativistic effects (Pb). Revision of the data processing procedure has yielded an improvement in the profile symmetry of these results.

A new spectrometer dedicated to magnetic Compton studies has been designed and constructed. It uses circularly polarised radiation obtained by viewing the tangent point of the Daresbury synchrotron wiggler line at a small inclination to the orbital plane. Magnetic Compton profile measurements of polycrystalline iron undertaken with 54keV circularly polarised synchrotron radiation (CPSR) show a larger central dip than predicted by band theory calculations of the electron spin dependent density distribution. Data on polycrystalline cobalt has also been obtained. A transmission scattering geometry and 60keV CPSR have been used to measure, for the first time, directional Compton profiles of the unpaired spin electrons in a single crystal of iron. Separation of the contributions from the majority and minority spin electrons provide a more critical test of band theory than is possible with polycrystalline results.

Contents

MEMORANDUM

This dissertation has been submitted to the University of Warwick in support of my application for the admission to the degree of Doctor of Philosophy. It contains an account of my own independent research except where acknowledged in the text. The work was performed in the Department of Physics under the supervision of Dr. M. J. Cooper during the period from October 1985 to September 1988. Details of research to which I have contributed may be found in the following publications:

1. Assessment of a New Method for Determining Elastic to Compton Ratios in Scattered beam NDE, J. Phys. E20,76, 1986.

2. Spin Dependent Momentum Distribution of Iron Studied with Circularly Polarised Radiation, Phys. Rev., B34, 5984, 1986.

3. The Magnetic Compton Profiles of Iron and Cobalt, J. Phys., F18, L57, 1988.

4. Magnetic Anisotropy in the Electron Momentum Density of Iron, Nature, 333, 151, 1988.

5. Magnetic Compton Profile of Gadolinium, submitted to J.Phys. F., 1989.

ACKNOWLEDGEMENTS

UNITS

Throughout this thesis the system of units adopted, unless otherwise stated, is that of 'atomic units'. In this notation $\hbar=1$, $m=1$ and $c=137.036$ and it follows that,

$$1 \text{a.u. of momentum} = \frac{mc}{137.036} = 1.9929 \times 10^{-24} \text{kgms}^{-1}$$

$$1 \text{a.u. of energy} = \frac{mc^2}{137.036^2} = 4.3598 \times 10^{-18} \text{J}$$

$$1 \text{a.u. of length} = \frac{137.036\hbar}{mc} = 5.2918 \times 10^{-11} \text{m}$$

Chapter 1

PHOTON SCATTERING THEORY.

1.1 Introduction.

In 1923 A.H.Compton discovered an effect which could not be explained within the confines of classical mechanics (Compton 1923). Analysing radiation scattered by a target material he discovered it contained two different frequency components. One had the same frequency as the incident radiation , this was predicted by classical mechanics and another which was shifted to a somewhat lower frequency. To explain this frequency shift Compton used a quantum mechanical description for energy and momentum. Combining conservation of momentum and energy in a 'collision' between a photon of energy ω_1 and a stationary electron, Compton showed that a given scattering angle ϕ leads to a discrete scattered photon energy ω_2, i.e.

$$\omega_2 = \omega_1 \left[1 + \frac{\omega_1}{m_0 c^2}(1 - \cos\phi)\right]^{-1} \tag{1.1}$$

which in terms of photon wavelength is,

$$\Delta\lambda = \lambda_2 - \lambda_1 = \frac{h}{m_0 c}(1 - \cos\phi) \tag{1.2}$$

where λ_1 and λ_2 are the incident and scattered photon wavelengths respectively, c the velocity of light, m_0 the electron rest mass and h is the Planck constant.

Apart from being an early vindication of quantum ideas the Compton shift formula , equation 1.1 is devoid of information about the target. However, a real target contains

1

bound electrons and bound electrons cannot be stationary. In fact, the valence electrons in a solid have velocities in the range 10^5–10^6ms^{-1} and the core electrons in a heavy elements such as gold and lead can attain relativistic velocities.

Jauncey (1925) was the first to suggest that the momentum of the scattering electron may have a bearing on the structure of the Compton scattered beam and that the scattered radiation had a definite frequency distribution. This frequency spread was explained by Dumond (1929) in terms of a Doppler broadening mechanism.

Having linked the spectral distribution of Compton scattered radiation to the electron velocity distribution, it should in principle, be possible to study the motion of the scattering electrons by analysing the Compton lineshape. The following simple argument serves to demonstrate this point, a more rigorous account is given in section 1.3.

When the energy transfer E_{tran}, to the scattering electron is large compared to its binding energy E_{bind}, the interaction is termed impulsive i.e. both the photon and the recoiling electron must have left the atom before it has time to 'relax' from its excited state. The electron is ejected into the continuum as a plane wave. The consequence of this Impulse Approximation (IA) is that the nuclear potential $V(r)$ can be treated as constant throughout the interaction . Under these circumstances the interaction reduces to a binary encounter between the photon and moving electron (see figure 1.1) and only kinetic energy terms feature in the final non relativistic conservation equation i.e.

$$(\omega_2 - \omega_1) = \omega = \frac{(\mathbf{p_1 + K})^2}{2m_0} - \frac{|\mathbf{p_1}|^2}{2m_0} = \frac{|\mathbf{K}|^2}{2m_0} + \frac{\mathbf{K \cdot p_1}}{m_0} \tag{1.3}$$

The nomenclature is the same as that used in figure 1.1 .

The first term in equation 1.3 is the familiar Compton shift given by equation 1.2 . The additional term is linearly dependent upon one component, p_z, of the electron ground state momentum and is sometimes referred to as the Doppler shift term.

If $n(\mathbf{p})$ is the probability of finding an electron with momentum $\mathbf{p}$, then for a given energy ω_2, the scattered intensity is proportional to the number of electrons for which equation 1.3 is satisfied. The Compton lineshape or profile, $J(p_z)$ is therefore a 1-dimensional projection of the 3-dimensional momentum density distribution, $n(\mathbf{p})$ along the scattering vector.
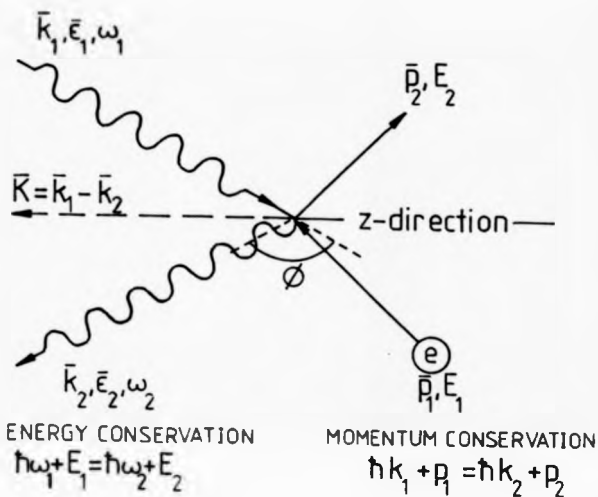
Figure 1.1 Schematic representation of the Compton scattering interaction between a free electron of initial momentum p_1 and energy E_1 and a photon with initial energy $\hbar\omega_1$, wavevector k_1 and of unit polarisation ϵ_1. The scattered photon leaves with an energy $\hbar\omega_2$, wavevector k_2 and unit polarisation ϵ_2 and the electron recoils with an energy E_2 and momentum p_2. The scattering vector is denoted by K and the scattering angle is ϕ.

$$J(p_z) = \int_{p_x} \int_{p_y} \mathrm{n}(p_x, p_y, p_z) dp_x dp_y \tag{1.4}$$

and is subject to the normalisation rule

$$\int_{-\infty}^{+\infty} J(p_z) dp_z = Z \tag{1.5}$$

where Z is the number of electrons.

From equation 1.4 it is evident that the energy spectrum of Compton scattered radiation contains information about the distribution of electron momentum of the scattering material. The attraction of Compton profile measurements is that the Compton lineshape is dominated by the behaviour of the slower moving valence electrons, the core electrons in contrast simply provide an isotropic background. The information obtained is complementary to that obtained from other techniques such as X-ray diffraction, which provide information about the electrons in terms of their position in real space. Over the past 15 years many Compton profile measurements have been made, particularly on the first series transition metals, with unpolarised x-ray and γ-ray sources of radiation (see Cooper, 1985 for a general review). The results obtained have provided a critical test of the ability of band theory calculations to reproduce the momentum distributions of the electrons. The existence of spin dependent terms in the Compton scattering cross section have been realised for many years (Lipps and Tolhoek, 1954). Although under normal experimental circumstances these terms are imaginary to first order and only become real in second order. If circularly polarised radiation is used it is possible to obtain an additional contribution to the Compton scattering cross section. This additional contribution is related to the momentum distribution of the unpaired electron spins of the scatterer, this is discussed in detail in section 1.4 .

Compton scattering is not the only experimental technique for obtaining $n(p)$ and its closest rival is the technique of positron annihilation where the momentum distribution of the positron-electron system just prior to annihilation is obtained directly by momentum conservation from the angular distribution of the two photons created in the annihilation. The technique of positron annihilation for studying momentum densities has two advantages

over Compton scattering namely : superior momentum resolution and the ability to obtain a 2-dimensional slice of $n(\mathbf{p})$. There is a disadvantage. Due to the repulsive force between the positron and the ion core of the atom the positron does not sample the high momentum components of the electron density situated near the ion core. Therefore positron annihilation unlike Compton scattering is suited to probing only the valence electron states near to the Fermi surface.

The first half of this thesis is concerned with extending the extensive study of the momentum densities of electrons in the elements, which have been performed by various workers in this field, by studying simple binary systems such as $Fe_{0.7}Ni_{0.3}$ alloy and GaAs. Results are also presented on Pb where the relativistic behaviour of the core electrons is of particular interest. The remaining chapters describe experiments in which circularly polarised radiation was used to obtain new information about the momentum distribution of the unpaired spins in ferromagnetic iron and cobalt.

1.2 The Interaction of Radiation and Matter

In the x-ray and γ-ray regime below 1MeV, a photon can interact with matter by photoelectric absorption, elastic or inelastic scattering. All of these processes result in a removal of photons from an incident beam. The relative cross sections of each interaction are dependent upon both the incident photon energy, ω_1 and the atomic number of the scatterer, Z. Figure 1.2 shows that for the range of energies and materials involved in Compton scattering studies, photoelectric absorption is the main cause of beam attenuation. The resulting photoelectron decays by emission of bremsstrahlung radiation and when the electron hole is refilled fluorescence radiation is emitted. The elastic interaction is described by the classical Thomson cross section given below,

$$\left[\frac{d\sigma}{d\Omega}\right]_{Th} = \left[\frac{e^2}{m_0c^2}\right]^2 (\epsilon_1.\epsilon_2)^2 \tag{1.6}$$

where $[d\sigma/d\Omega]_{Th}$ is the classical Thomson cross section and $[e^2/m_0c^2]$ is the classical electron radius, r_0. For unpolarised radiation this becomes,

4
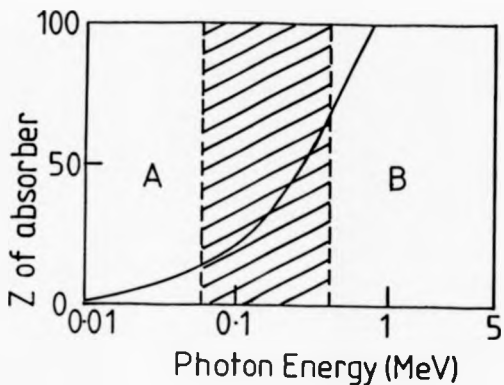
Figure 1.2 The relative importance of photoelectric absorption. To the left of the solid line (region A) the process of photoelectric absorption dominates over Compton scattering but to the right of the solid line (region B) the situation is reversed and Compton scattering is the dominant process. The cross hatched area represents the range of incident energies in general use for Compton scattering studies.

$$\left[\frac{d\sigma}{d\Omega}\right]_{Th} = \frac{r_0^2}{2}(1 + \cos^2\phi). \tag{1.7}$$

This cross section can be extended to describe scattering from a distribution of bound electrons by the inclusion of an atomic scattering factor $f(\mathbf{K})$. This scattering factor takes account of the interference of waves scattered from different parts of the electron distribution, i.e.

$$\left[\frac{d\sigma}{d\Omega}\right] = \left[\frac{d\sigma}{d\Omega}\right]_{Th} |f(\mathbf{K})|^2 \tag{1.8}$$

where $\rho(\mathbf{r})$ is the electron charge density and

$$f(\mathbf{K}) = \int \rho(\mathbf{r}) exp(-i\mathbf{K}.\mathbf{r})d^3\mathbf{r}. \tag{1.9}$$

When the electron distribution is part of a regular array of atoms, for example in a single crystal, the structure factor has non zero values only for specific $\mathbf{K} = \mathbf{G}$-reciprocal lattice vector. This is the condition for Bragg reflections.

Inelastic scattering involves a change in wavevector $\mathbf{k}_1$ and the incoherent scattered intensity from an atomic distribution is simply Z times that form a single electron. Inelastic scattering is not possible if the energy transfer to the recoil electron does not exceed the electron binding energy, or in the case of a conduction metal, the Fermi energy $\hbar k_f$ of the free electron gas, due to of the absence of an unoccupied final state.

When the momentum transfer from the photon to a single electron is conserved the interaction is referred to as Compton scattering, the necessary condition being $E_{tran} \gg E_{bind}$. However when the energy transfer is of the order of the electron binding energy the momentum is not transferred to an individual electron but is absorbed by the whole crystal. This interaction is termed Raman scattering and results in a change in the state of the scattering atom. In the past the resonant enhancement of Raman scattering which occurs when ω_1 is close to the binding energy of one of the core electrons has not been exploited because of the unavailability of sources of radiation with energies near the K shell absorption edge of a suitable material. The arrival of synchrotrons which offer intense, tunable sources of radiation has now triggered an experimental interest in this process (for example see Manninen, Suortti,

Cooper, Chromilier and Loupias, 1986).

1.3 Compton Scattering Theory.

Inelastic scattering is an established technique employed in solid state physics and a variety of probes are available, for example, electrons, neutrons, nucleons, photons etc. (see Platzman, 1972 for a general review). In each case the total flux of scattered particles (or photons) is measured and the differential scattering cross section $d\sigma/d\Omega$ deduced.

When inelastic Compton processes are involved, the spectral distribution of the scattered radiation can be recorded and the double differential scattering cross section $d^2\sigma/d\Omega d\omega$ obtained. The aim of this section is to show how the Compton profile $J(p_z)$, given by equation 1.4, can be extracted from the measured double differential scattering cross section and thus lead to an interpretation of the scattered spectrum in terms of the electronic wavefunctions of the scatterer.

1.3.1 Scattering within the Born Approximation.

If the interaction between the probe and the scattering system is weak, the scattering cross section can be completely characterised by the momentum transfer ($\mathbf{K} = \mathbf{k}_1 - \mathbf{k}_2$) and the energy transfer ($\omega = \omega_1 - \omega_2$). For weak scattering the effects of the scattered probe on the system are negligible and the coupling between the probe and the scattering system may be treated within the first order Born Approximation (see Gasiorowicz, 1974 chapter 24). This approximation enables the double differential scattering cross section to be written as the product of two terms

$$\frac{d^2\sigma}{d\Omega d\omega} = \left[\frac{d\sigma}{d\Omega}\right]_0 S(\mathbf{K}, \omega). \tag{1.10}$$

The function $S(\mathbf{K}, \omega)$ is a generalised scattering factor which describes the dynamics of the scattering particle . It is this term which is the focus of attention in condensed matter physics. The other term $(d\sigma/d\Omega)_0$ characterises the coupling between the probe and the target and for x-rays ($\omega_1 < 10\text{keV}$) it can be represented by the classical Thomson cross

6

section (equation 1.7). For higher photon energies ($\omega_1 \geq 60\text{keV}$ for γ-sources in common use) $(d\sigma/d\Omega)_0$ is better represented by the cross section formulated by Klein and Nishina (1929) for relativistic scattering of unpolarised photons by free, stationary and spinless electrons,

$$\left(\frac{d\sigma}{d\Omega}\right)_{K-N} = \frac{1}{2}r_0^2 \left(\frac{\omega_2}{\omega_1}\right)^2 \left(\frac{\omega_1}{\omega_2} + \frac{\omega_2}{\omega_1} - \sin^2\phi\right). \tag{1.11}$$

In the non relativistic Thomson limit where (ω_1/ω_2) tends to unity this reduces to equation 1.7 .

Writing the double differential cross section in terms of an interaction term and an autocorrelation function describing the dynamics of the interaction is valid for all inelastic scattering experiments and the information obtained is distinguished by the region of $(\mathbf{K}, \omega)$ space accessible to the probe (Williams, 1977 chapter 2.1). For photon scattering the scattering factor $S(\mathbf{K}, \omega)$ is obtained using time dependent perturbation theory via the Golden Rule as,

$$S(\mathbf{K}, \omega) = \frac{\omega_2}{\omega_1} \sum_f \sum_i \left| < f \mid \sum_j \exp i(\mathbf{K}.\mathbf{r}_j) \mid i > \right|^2 \delta(E_2 - E_1 - \omega). \tag{1.12}$$

The energy delta function restricts the summations to those states accessible with energy conservation. $\mid i >$ and $\mid f >$ are the initial and final states of the many body operator $\sum_j \exp(i\mathbf{K}.\mathbf{r}_j)$ which is termed the Born operator and gives the phase of the scattering amplitude of the jth target electron. For Compton scattering the energy transfer must be sufficiently large enough for the final state $\mid f >$ to be a plane wave. Substituting for $S(\mathbf{K}, \omega)$ in equation 1.10 gives the following general scattering formula,

$$\frac{d^2\sigma}{d\Omega d\omega} = \left(\frac{d\sigma}{d\Omega}\right)_0 \frac{\omega_2}{\omega_1} \sum_f \sum_i \left| < f \mid \sum_j \exp(i\mathbf{K}.\mathbf{r}_j) \mid i > \right|^2 \delta(E_2 - E_1 - \omega). \tag{1.13}$$

1.3.2 Scattering from Bound Electrons.

The calculation of the scattering cross section for bound electrons is difficult, however within the IA (see section 1.1) it can be simplified by representing the bound electrons as free electrons moving with the momentum distribution of bound electrons. Much experimental

7

and theoretical effort has been focussed on establishing the effect on the Compton profile when the IA becomes valid, this is discussed in section 1.3.3 but assuming the IA holds (i.e. $E_{tran} \gg E_{bind}$) the final electron state $| f >$ in equation 1.12 can be written as a plane wave, $| f >= \exp(i\mathbf{p_2 . r_j})$, and substituting for the initial ($| i >= \psi_i(\mathbf{r_j})$) and final electron states, the matrix element in equation 1.13 becomes,

$$\left| < f \mid \sum_j \exp(i\mathbf{K.r_j}) \mid i > \right|^2 = \sum_j \left| \exp(-i\mathbf{p_2.r_j}) \exp(i\mathbf{K.r_j}) \int \psi_i(\mathbf{r_j}) d\mathbf{r_j} \right|^2 \quad (1.14)$$

$$= \sum_j \left| \int \psi_i(\mathbf{r_j}) \exp(i(\mathbf{K} - \mathbf{p_2}).\mathbf{r_j}) d\mathbf{r_j} \right|^2. \quad (1.15)$$

Including conservation of momentum ($\mathbf{K} = \mathbf{k_1} - \mathbf{k_2} = \mathbf{p_2} - \mathbf{p_1}$) reduces the matrix element further,

$$= \sum_j \left| \int \psi_i(\mathbf{r_j}) \exp(-i\mathbf{p_1.r_j}) d\mathbf{r_j} \right|^2. \quad (1.16)$$

The integral is simply the Fourier transform of the position space wavefunction which is defined as the momentum space wavefunction $\chi_i(\mathbf{p})$. Just as $|\psi(\mathbf{r})|^2$ is the electron charge density distribution $\rho(\mathbf{r})$, $|\chi(\mathbf{p})|^2$ is the electron momentum distribution $n(\mathbf{p})$ and the matrix element becomes,

$$\sum_f \sum_i \left| < f \mid \exp(i\mathbf{K.r_j}) \mid i > \right|^2 = n(\mathbf{p}). \quad (1.17)$$

Recalling the energy transfer expression, equation 1.3, the delta function in equation 1.13 may be expressed in terms of the scattering vector and the incident electron momentum. Thus within the IA the scattering cross section for the Compton scattering interaction is given by,

$$\frac{d^2\sigma}{d\Omega d\omega} = \left(\frac{d\sigma}{d\Omega}\right)_0 \left(\frac{\omega_2}{\omega_1}\right) \int_{p_x} \int_{p_y} n(\mathbf{p}) \delta \left(\omega - \frac{|\mathbf{K}^2|}{2m} - \frac{\mathbf{K.p}}{m} \right) dp_x dp_y \quad (1.18)$$

or equivalently,

$$\frac{d^2\sigma}{d\Omega d\omega} = \left(\frac{d\sigma}{d\Omega}\right)_o \left(\frac{\omega_2}{\omega_1}\right) \frac{m}{|\mathbf{K}|} \int_{p_x} \int_{p_y} n(\mathbf{p}) dp_x dp_y \tag{1.19}$$

where the double integral is simply the Compton profile integral of equation 1.4. The Compton profile is extracted from the measured energy spectrum where each energy point in the Compton cross section corresponds to scattering from an electron of momentum p_z given by,

$$\frac{p_z}{m_0 c} = \frac{(\omega_2 - \omega_1) + \frac{\omega_1 \omega_2}{m_0 c^2}(1 - \cos\phi)}{(\omega_1^2 + \omega_2^2 - 2\omega_1\omega_2 \cos\phi)^{1/2}} \tag{1.20}$$

1.3.3 The Validity of the Impulse Approximation.

Experimental evidence for the breakdown of the IA has been obtained by various workers Weiss (1975) and Weiss, Cooper and Holt (1977) (x-ray scattering) and Barlas, Ruechner and Wellenstein (1977) (electron scattering) and is in the form of shifts in the Compton peak position relative to the value predicted by equation 1.1. Manninen, Cooper and Cardwell (1986) used 60keV γ-rays to measure the Compton profile of aluminium and graphite and although there was no observed shift in the Compton peak they did observe an asymmetry in the profile at ~1a.u..

Using Exact Hydrogenic (EH) states to describe S-type orbital scattering Eisenberger and Platzman (1970) and Mendelsohn and Biggs (1973) showed that corrections were proportional to $(E_{bind}/E_{tran})^2$, i.e. negligible until $E_{bind} \sim E_{tran}$ and at this point the Impulse Hydrogenic (IH) result exceeded the EH result. Currat, DeCicco and Weiss (1971) extended the theoretical comparison from the hydrogenic atom to the many electron atom and found good agreement with the IA. Compton profile measurements of lithium, graphite, aluminium (Currat, DeCicco and Weiss, 1971) and also directional measurements of beryllium (Currat, DeCicco and Kaplow, 1971) were made with Mo Kα radiation and the core contributions were separated from the valence electron contribution. Fair agreement was found between the measured core electron Compton profiles and the calculated Compton core. Mendelsohn, Bloch and Smith (1973), Bloch and Mendelsohn (1974) and Mendelsohn and Bloch (1975) found that the correction for L-type orbital scattering was opposite to that for S-type orbital scattering i.e. $J_{EH}(0) > J_{IH}(0)$ and it was concluded by Mendelsohn (1975) in a calculation

9

of a total Compton profile that the overall shift in the Compton peak due to the breakdown of the IA would be negligible for a complete atom.

In general, the IA holds for the loosely bound valence electrons but not always for the core electrons. The Compton profile is sensitive to the valence electron distribution and therefore some error in the low, flat, isotropic core contribution can be tolerated particularly since Compton data is usually presented in the form of directional difference profiles which removes the isotropic core contribution of the Compton profile. The breakdown of the IA is easily avoided by using high scattering angles and high incident energies thus ensuring large momentum transfers and that $J(p_z)$ can easily be extracted from the measured cross section.

1.3.4 The Relativistic Compton Scattering Cross Section.

The validity of the IA necessitates high energy transfers and these are achieved in present Compton scattering experiments by utilising the high energy γ-rays emitted from radioactive isotopes such as ^{241}Am(59.5keV) or ^{198}Au(412keV). As ω_1 becomes an appreciable fraction of mc^2 ($\omega_1/mc^2 = 0.80$ for ω_1=412keV) the nonrelativistic treatment of the scattering given in section 1.3.2 must be extended. The scattering cross section for these high energy interactions can only be obtained by a full relativistic quantum mechanical analysis of the interaction.

Jauch and Rohrlich (1955) generalised the Klein Nishina cross section by introducing a distribution of free, moving electrons to arrive at the expression below,

$$\frac{d^2\sigma}{d\Omega d\omega} = \frac{r_0^2 m_0^2 \omega_2}{2E_2} \int \frac{n(p_1)d^3p_1}{\omega_1 E_1} \int X\delta(k_1 + p_1 - k_2 - p_2)d^3p_2. \qquad (1.21)$$

The term X is a flux factor dependent on both the initial electron energy, E_1 and momentum, p_1. Because X can not be removed from the integration it is in general very difficult to extract $J(p_z)$ from this form of the cross section.

Manninen, Paakkari and Kajantie (1974) and Eisenberger and Reed (1974) were able to reduce the cross section to a more suitable form by considering the scattering to be from mildly relativistic electrons with no net spin. The electron energy E_1 is replaced by the rest mass energy (m_0c^2) and in the limit of $\phi \to 180°$, the flux factor $X_{180°}$ becomes independent of E_1 and p_1 and can be removed from the integration.

10

Ribberfors (1975 a, b) extended the approaches used by Eisenberger and Reed and Manninen, Paakkari and Kajantie by integrating by parts their relativistic cross section (equation 1.21) to obtain the double differential cross section in the form of a rapidly converging series expansion. For scattering angles $\geq 165°$ the leading or zeroth term is sufficient to describe the scattering i.e.

$$\frac{d^2\sigma}{d\Omega d\omega} = \frac{r_1^2 m_0^2 \omega_2 c^4}{2\omega_1 |\mathbf{K}| E_1} X' J(p_z)$$ (1.22)

where X' is a more complicated expression than X but reduces to X for $\phi \to 180°$ and is a function of p_1, E_1 and ϕ (see Ribberfors, 1975,b). The zeroth order Ribberfors cross section has been used throughout the first half of this thesis in analysing the experimental results obtained using unpolarised photons.

1.4 Spin Dependent Compton Scattering.

Section 1.3 demonstrated how the electron momentum density distribution $n(p)$ could be extracted from the measured spectrum of scattered radiation. Although a relativistic treatment of the scattering was discussed, neither the electron spin or the photon polarisation were considered. The interaction of x-rays and γ-rays with matter is usually described by the Thomson scattering mechanism. In this case the interaction is considered to arise from the acceleration of the electron by the electric field of the incident photon followed by the electric dipole re-radiation of the scattered field (see figure 1.3a). Note that there is no change in the plane of polarisation. In this classical picture x-rays and γ-rays may seem to be only capable of providing information about the electron charge density and not about its spin density.

A closer examination of the interaction reveals that the magnetic moment of the electron m does interact with the magnetic field of the photon (see figure 1.3b). In this case the same acceleration of the electron by the electric field of the photon results in a magnetic quadrupole re-radiation of the scattered field and in this case there is a change in the plane of the polarisation. As figures 1.3a and b show the two scattered waves are in quadrature and the ratio of magnetic dipole to electric quadrupole radiation is $\sim \hbar\omega_1/m_0 c^2$. The Klein

11
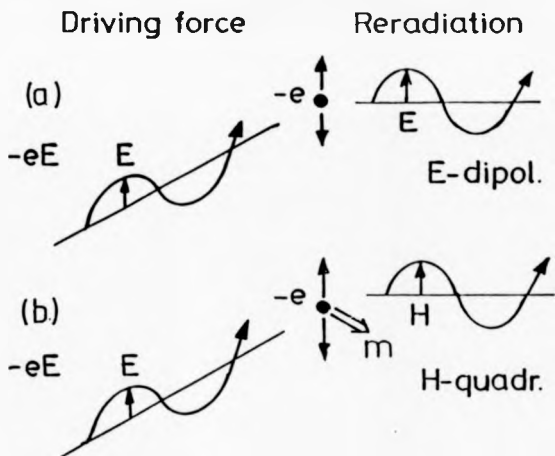
Figure 1.3 The classical mechanism for x-ray scattering

(a) Thomson scattering , the electron charge is set into oscillation by the electromagnetic field of the incident photon and an electric dipole reradiation occurs.

(b) Spin scattering , this time the electron has a magnetic moment m. The oscillation of this moment results in a magnetic quadrupolar reradiation.

from De Bergevin and Brunel (1981)

Nishina formula of equation 1.11 was formed by a quantum mechanical approach and although it takes account of this spin scattering it is concerned with the mean values averaged over all spin states. To calculate the magnetic Compton scattering cross section requires a similar but more complex relativistic treatment than the non-magnetic situation involving both the electron and photon polarisations. Such a complicated relativistic calculation is beyond the scope of this thesis.

The geometrical factors associated with the spin and orbital contributions to the scattering are the focus of attention of the magnetic scattering cross section because they dictate specific experimental parameters. It will be shown that as in the non-magnetic case, the same relationship between the cross section and a 'magnetic Compton profile' is obtained by a non-relativistic treatment of the scattering and that the same geometrically factors are obtained as those defined in a relativistic calculation by Lipps and Tolhoek (1954). The situation can thus be simplified whilst remaining just as illuminating if the scattering is treated nonrelativistically i.e. assuming $|k_1| \sim |k_2|$.

1.4.1   Introduction.

The electron and photon polarisations were first introduced into the scattering cross section calculation by Franz (1938) in his calculation of a cross section for polarised radiation scattered by oriented electrons. Gell-Mann and Goldberger (1954) and Low(1954) also accounted for magnetic effects in their derivation of the cross section for photons and free, charged particles of spin $\frac{1}{2}$. They independently expanded the photon scattering amplitude in a power series in photon frequency, the zeroth term being the classical Thomson cross section equation 1.6. Both authors found the first order term, which was linear in frequency, to be a function of the charge, mass and static magnetic moment of the scattering particle and noted that the first order 'magnetic term' was almost negligible compared to the leading Thomson term.

Using 3-dimensional vectors for the photon and electron polarisations Lipps and Tolhoek (1954a) arrived at an expression for the cross section from which any specific polarisation effect could be obtained by averaging over the unobserved polarisation vectors (Lipps and Tolhoek, 1954b) of the photon or electron. From Lipps and Tolhoek (1954a) equation 4.14,

the complete result for the cross section has the general form,

$$\frac{d^2\sigma}{d\Omega d\omega} = r_0^2 \left(\frac{k_2}{k_1}\right)^2 \Phi(k_1, k_2, \epsilon_1, \epsilon_2, \zeta_1, \zeta_2) \qquad (1.23)$$

where ζ_1 and ζ_2 are the polarisation vectors of the electron before and after the interaction and $k_1, k_2, \epsilon_1, \epsilon_2, r_0$ are as previously defined. $\Phi(k_1, k_2, \epsilon_1, \epsilon_2, \zeta_1, \zeta_2)$ is a linear function of the polarisation vectors and is dependent upon the set of polarisation vectors chosen (see Lipps and Tolhoek 1954b, equations 1.2, 1.3).

The possibility of using the magnetic terms in the cross section to study magnetisation densities was pointed out by Platzman and Tzoar (1970). In particular they showed that incoherent Compton scattering of polarised x-rays could be used to determine the spin dependent momentum distribution function of the unpaired electrons in ferromagnetic materials. They also suggested that Bragg scattering of unpolarised x-rays could be used to determine the magnetic structure of antiferromagnetic solids. The Platzman and Tzoar cross section includes only the leading order magnetic contribution to the Compton scattering cross section i.e. order $\hbar\omega_1/m_0c^2$. The cross section to order $(\hbar\omega_1/m_0c^2)^2$ and p/m_0c^2 has been calculated by a complex quasi-relativistic calculation (Grotch, Kazes, Bhatt and Owen, 1983) which was later confirmed by the same group in a relativistic calculation of the spin dependent Compton cross section (Bhatt, Grotch, Kazes and Owen, 1983). Step by step derivations for the polarisation dependence of the cross section, including magnetic terms have been presented by Lovesey (1987) and Blume and Gibbs (1988). Although both reviews consider the diffraction case i.e. elastic scattering, in the low energy limit $|k_1| \sim |k_2|$ the derivation of the corresponding Compton cross section proceeds via an analogous route.

In the proceeding section the approach of Lovesey is adopted to formulate the polarisation dependent x-ray scattering cross section, including magnetic terms, for the low energy limit.

1.4.2 Polarisation Dependence of the Magnetic Scattering Cross Section.

The polarisation vector of a photon can be represented by the superposition of two orthogonal polarisations chosen in some specified manner. They may be two mutually perpendicular polarisations or circular polarisations of opposite hands. For a photon traveling along the x-

axis of a cartesian coordinate system (see figure 1.4) right hand (+) and left hand (-) circular polarisation $\epsilon^{(\pm)}$ can be written

$$\epsilon^{(\pm)} = \frac{-i}{\sqrt{2}}(\epsilon_x \pm i\epsilon_y) \tag{1.24}$$

Following Lovesey (1987) a density matrix $\mathbf{D}$ is employed to describe states of partial polarisation. The polarisation matrix $\mathbf{D}_{\alpha\beta}$ has the following properties ;

- $\mathbf{D}_{\alpha\beta}$ is Hermitian,

- $Tr(\mathbf{D}_{\alpha\beta}) = 1$,

- $\mathbf{D}_{\alpha\beta}$ is in a plane perpendicular to $\mathbf{k_1}$, i.e. in the x,y plane in figure 1.4,

- $\epsilon^*\mathbf{D}\epsilon$ = the probability the a photon has a specific polarisation ϵ.

For notational convenience the polarisation can be described by 3 real Stokes parameters P_1, P_2 and P_3 which together form the vector $\mathbf{P}$ and the density matrix $\mathbf{D}$ becomes

$$\mathbf{D} = \frac{1}{2}\begin{pmatrix} 1 + P_3 & P_1 - iP_2 \\ P_1 + iP_2 & 1 - P_3 \end{pmatrix}. \tag{1.25}$$

The first application of the Stokes parameters to magnetic x-ray scattering was by de Bergevin and Brunel (1981, a). Their representation is particularly useful as it applies to both completely and partially polarised radiation. For the scattering geometry in figure 1.4, P_1 describes linear polarisation along directions at angles $\pm\pi/4$ to the y-axis, P_2 describes the degree and hand of circular polarisation and P_3 describes the polarisation perpendicular and parallel to the scattering plane. For complete linear polarisation $P_1^2 + P_3^2 = 1$, $P_2 = 0$ and for a completely unpolarised photon $P_1^2 = P_2^2 = P_3^2 = 0$. A practical explanation of the Stokes parameters is given in Hecht and Zajac section 8.12.1.

As any 2×2 matrix can be expressed in terms of the unit matrix $\mathbf{I}$ and Pauli matrices $\check{\sigma}$, thus the density matrix $\mathbf{D}$ can be written,

$$\mathbf{D} = \frac{1}{2}(\mathbf{I} + \mathbf{P}.\check{\sigma}) \tag{1.26}$$

14
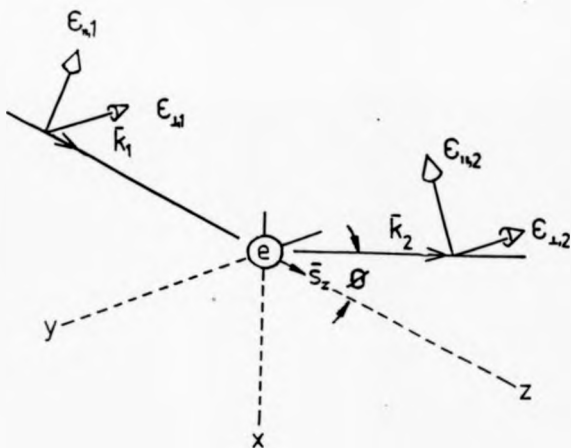
Figure 1.4 Schematic representation of the interaction between a photon with wavevector k_1 and an electron, labelled 'e', which is aligned so that the electron spin is parallel to k_1 and the z-axis of a cartesian coordinate system. The photon polarisation has been decomposed into two mutually perpendicular unit polarisation vectors $\epsilon_{\parallel 1}$ and $\epsilon_{\perp 1}$. Quantities with subscript 2 refer to the scattered photon. The scattering angle is ϕ.

where the Pauli matrices are,

$$\sigma_x = \begin{pmatrix} 0 & 1 \\ 1 & 0 \end{pmatrix} \sigma_y = \begin{pmatrix} 0 & -i \\ i & 0 \end{pmatrix} \sigma_z = \begin{pmatrix} 1 & 0 \\ 0 & -1 \end{pmatrix}. \tag{1.27}$$

Like the density matrix the amplitude for photon scattering (i.e. the Born operator in equation 1.13) may also be written in terms of a 2×2 matrix, M and expressed in terms of the unit matrix and Pauli matrices,

$$M = \hat{\beta}I + \hat{\alpha}.\hat{\sigma} = \begin{pmatrix} \hat{\beta} + \hat{\alpha_3} & \hat{\alpha_1} - i\hat{\alpha_2} \\ \hat{\alpha_1} + i\hat{\alpha_2} & \hat{\beta} - \hat{\alpha_3} \end{pmatrix} \tag{1.28}$$

where $\hat{\alpha} = (\hat{\alpha_1}, \hat{\alpha_2}, \hat{\alpha_3})$ and $\hat{\beta}$ contain the target information and I and $\hat{\sigma}$ are matrices describing the polarisation algebra. According to Tolhoek (1956), McMaster (1961) and Landau and Lifshitz (1982) the scattering cross section may written as,

$$\frac{d\sigma}{d\Omega} = r_0^2 Tr\{DM^*M\}, \tag{1.29}$$

substituting for D, M^* and M gives

$$\frac{d\sigma}{d\Omega} = \frac{r_0^2}{2} Tr(I + P.\hat{\sigma})(\hat{\beta}^*I + \hat{\alpha}^*.\hat{\sigma})(\hat{\beta}I + \hat{\alpha}.\hat{\sigma}). \tag{1.30}$$

As the trace operates only on the polarisation states i.e. I and $\hat{\sigma}$, the trace operation can be performed using the standard properties of Pauli matrices (Lovesey, 1986). The mathematics of this derivation are presented in Appendix A and lead to the following cross section which is valid for any initial photon polarisation,

$$\frac{d\sigma}{d\Omega} = r_0^2(\hat{\alpha}^*.\hat{\alpha} + \hat{\beta}^*\hat{\beta} + \hat{\beta}^*(\hat{\alpha}.P) + (\hat{\alpha}^*.P)\hat{\beta} + iP \ \hat{\alpha}^* \wedge \hat{\alpha}). \tag{1.31}$$

Remember that $\hat{\alpha}$ and $\hat{\beta}$ form the matrix elements of the Born operator M in equation 1.28. Now, according to Platzman and Tzoar (1970) the scattering amplitude M can also be written as a sum of spin dependent and spinless terms, which to leading order in $\hbar\omega_1/m_0c^2$ is

15

$$M = \sum_j \exp(i\mathbf{K}.\mathbf{r}_j)(\epsilon_2.\epsilon_1 - i\frac{\hbar\omega_1}{m_0c^2}\mathbf{s}_j.\mathbf{B}) \qquad (1.32)$$

where $\mathbf{s}_j$ and $\mathbf{r}_j$ are the spin and position of the jth electron. This can be extended (see Grotch, Kazes, Bhatt and Owen, 1983 and Platzman and Tzoar, 1985) to include electron orbital momentum $\mathbf{p}_j$ to give,

$$M = \sum_j \exp(i\mathbf{K}.\mathbf{r}_j)(\epsilon_2.\epsilon_1 - i\frac{\hbar\omega_1}{m_0c^2}[\mathbf{s}_j.\mathbf{B} + \frac{i}{\hbar|\mathbf{K}|^2}(\mathbf{k}_1 \wedge \mathbf{p}_j).\mathbf{A}]) \qquad (1.33)$$

where

$$\mathbf{A} = \begin{pmatrix} 0 & \hat{\mathbf{k}}_1 \\ -\hat{\mathbf{k}}_2 & \hat{\mathbf{k}}_2 \wedge \hat{\mathbf{k}}_1 \end{pmatrix} \qquad (1.34)$$

$$\mathbf{B} = \begin{pmatrix} \hat{\mathbf{k}}_1 \wedge \hat{\mathbf{k}}_2 & -\hat{\mathbf{k}}_2(1 - \cos\phi) \\ \hat{\mathbf{k}}_1(1 - \cos\phi) & \hat{\mathbf{k}}_1 \wedge \hat{\mathbf{k}}_2 \end{pmatrix} \qquad (1.35)$$

and

$$\epsilon_2.\epsilon_1 = \begin{pmatrix} 1 & 0 \\ 0 & \hat{\mathbf{k}}_1.\hat{\mathbf{k}}_2 \end{pmatrix}. \qquad (1.36)$$

$\hat{\mathbf{k}}_1$ and $\hat{\mathbf{k}}_2$ are unit vectors in the direction of $\mathbf{k}_1$ and $\mathbf{k}_2$. The leading term in equation 1.33 represents the photon charge interaction and leads to the familiar Thomson cross section for charge scattering .The remaining two terms can be identified with the spin and orbital momentum operators respectively and together describe the magnetic scattering. Note that the magnetic terms are smaller in amplitude than the charge term by $\hbar\omega_1/m_0c^2$ and are also in quadrature (see figure 1.3a, b). Following the same procedure used in the nonmagnetic case (see section 1.3) to obtain a relationship between the magnetic scattering cross section and a Compton profile, the Born operator is evaluated between the initial and final electron states,

$$< \psi_f \mid M \mid \psi_i > = n(\mathbf{p})\epsilon_2.\epsilon_1 - i\frac{\hbar\omega_1}{m_0c^2}[\mathbf{S}(\mathbf{p}).\mathbf{B} + (1 - \hat{\mathbf{k}}_1.\hat{\mathbf{k}}_2)\mathbf{L}(\mathbf{p}).\mathbf{A}] \qquad (1.37)$$

where $\mathbf{S}(\mathbf{p})$, $n(\mathbf{p})$ and $\mathbf{L}(\mathbf{p})$ are the ground state matrix elements of the spin charge and orbital interaction given by ,

16

$$S(p) = <\psi_f \mid \sum_j \exp(i\mathbf{K}.\mathbf{r}_j)\mathbf{s}_j \mid \psi_i > \qquad (1.38)$$

$$n(p) = <\psi_f \mid \sum_j \exp(i\mathbf{K}.\mathbf{r}_j) \mid \psi_i > \qquad (1.39)$$

$$L(p) = <\psi_f \mid \sum_j \frac{-2}{|K|^2} \exp(i\mathbf{K}.\mathbf{r}_j)(\mathbf{K} \wedge \nabla) \mid \psi_i > \qquad (1.40)$$

The quantities $S(p), n(p)$ and $L(p)$ have been written in an analogous manner to the charge and magnetic structure factors $S(K), n(K)$ and $L(K)$ defined for the diffraction case in Lovesey (1987) by equations 4.13–4.15. By equating the two expressions for M, equations 1.28 and 1.33, then using equation 1.37 it is possible to obtain expressions for $\bar{\alpha}$ and $\bar{\beta}$ in terms of the above quantities. These expressions have been evaluated for the diffraction case by Lovesey (equations 4.16–4.20) and in the x-ray limit ($|\mathbf{k}_1| \sim |\mathbf{k}_2|$), an analogous set of expressions can be formed for the inelastic scattering situation i.e.

$$\bar{\beta} = \frac{1}{2}\left[n(p)(1 + \hat{\mathbf{k}_1}.\hat{\mathbf{k}_2}) - i\frac{\hbar\omega_1}{m_0c^2}[(1 - \hat{\mathbf{k}_1}.\hat{\mathbf{k}_2})L(p) + 2S(p)].(\hat{\mathbf{k}_1} \wedge \hat{\mathbf{k}_2})\right], \qquad (1.41)$$

$$\bar{\alpha}_1 = -\frac{i}{2}\frac{\hbar\omega_1}{m_0c^2}(1 - \hat{\mathbf{k}_1}.\hat{\mathbf{k}_2})S(p).(\hat{\mathbf{k}_1} - \hat{\mathbf{k}_2}), \qquad (1.42)$$

$$\bar{\alpha}_2 = -\frac{1}{2}\frac{\hbar\omega_1}{m_0c^2}(1 - \hat{\mathbf{k}_1}.\hat{\mathbf{k}_2})[S(p) + L(p)].(\hat{\mathbf{k}_1} + \hat{\mathbf{k}_2}), \qquad (1.43)$$

$$\bar{\alpha}_3 = \frac{1}{2}\left[n(p)(1 - \hat{\mathbf{k}_1}.\hat{\mathbf{k}_2}) + i\frac{\hbar\omega_1}{m_0c^2}(1 - \hat{\mathbf{k}_1}.\hat{\mathbf{k}_2})L(p).(\hat{\mathbf{k}_1} \wedge \hat{\mathbf{k}_2})\right]. \qquad (1.44)$$

Within the x-ray limit the scattering cross section for any form of photon polarisation can be obtained by substitution of equations for $\bar{\alpha}$ and $\bar{\beta}$ given above into the general form of the cross section equation 1.31. It should be noted that in the diffraction case the charge and magnetic structure factors are quantities which can be measured experimentally, this is not true for the analogous quantities $S(p), n(p)$ and $L(p)$ defined for the inelastic scattering situation where the initial and final electron states differ. To arrive at a measurable quantity

17

for the inelastic experiment, namely a Compton profile, M must be squared, $S(p)$, $n(p)$ and $L(p)$ must be summed over all final states and the energy conservation delta function must be applied to restrict the summation to those states accessible with energy conservation, i.e. the same procedure as for the nonmagnetic case (see section 1.3).

1.5 The Magnetic Compton Scattering Cross Section.

For ferromagnetic transition metals such as iron, nickel or cobalt the magnetisation is almost entirely due to the spin interaction, the orbital contribution being quenched. Neglecting the orbital term and considering terms to order $\hbar\omega_1/m_0c^2$, $|M|^2$ becomes,

$$|M|^2 = (\epsilon_2.\epsilon_1)^2 - \frac{i\hbar\omega_1}{m_0c^2}(\epsilon_2.\epsilon_1)(s_j.B) + \left(\frac{\hbar\omega_1}{m_0c^2}\right)^2 (s_j^2 B^2). \qquad (1.45)$$

This reveals a contribution from the $i\epsilon_2.\epsilon_1(s_j.B)$ and the $s_j^2 B^2$ components of $|M|^2$. For x-ray Compton experiments ($\omega_1 \ll m_0c^2$) the B^2 term is small compared to the term which is linear in B and is generally neglected. The cross term $i\epsilon_2.\epsilon_1(s_j.B)$ describes the interference between the electron spin and the photon polarisation and this term vanishes for real polarisation vectors. However if the polarisation product $\epsilon_2.\epsilon_1$ is complex, i.e. if circularly polarised radiation is used, this term will make a real contribution to the scattering. For this case, the cross section to order $\hbar\omega_1/m_0c^2$ can be calculated by substituting for $\bar{\alpha}$ and $\bar{\beta}$ given by equations 1.41-1.44 in the previous section, into the general form of the cross section equation 1.31 and by choosing P_2 finite and $P_1 = P_3 = 0$, i.e. circularly polarised light.

This substitution is outlined in Appendix B and leads to the following result,

$$\frac{d\sigma}{d\Omega} = \frac{r_0^2 n(p)}{2}(n(p)(1 + \cos^2\phi) - \frac{2\hbar\omega_1}{m_0c^2}P_2(1 - \cos\phi) \qquad (1.46)$$
$$[S(p).(\vec{k}_1\cos\phi + \vec{k}_2) + \cos^2(\phi/2)L(p).(\vec{k}_1 + \vec{k}_2)])$$

A relativistic treatment of the scattering in the non-magnetic limit i.e. $S(p) = L(p) = 0$ would reduce the first term to the Klein Nishina cross section. Note that the spin and orbital moments are not additive as is the case for neutron scattering (Lovesey, 1986) but have

18

different geometrical factors. This leads to the exciting possibility of separating the spin and orbital contributions to the total magnetisation density by varying the geometrical factors prefacing them.

1.5.1 Spin Scattering.

If the orbital contribution is neglected the scattering cross section can be simplified to

$$
\begin{aligned}
\frac{d\sigma}{d\Omega} &= \frac{r_0^2 n(\mathbf{p})}{2}(n(\mathbf{p})(1 + \cos^2\phi) \\
&\quad - 2\frac{\hbar\omega_1}{m_0 c^2} P_2(1 - \cos\phi)\mathbf{S}(\mathbf{p}).(\hat{\mathbf{k}_1}\cos\phi + \hat{\mathbf{k}_2})).
\end{aligned} \tag{1.47}
$$

This equation has the same geometrical dependence as the analogous expression derived using a full relativistic treatment of the scattering (see equations 2.1, 2.2, 2.6 and 4.1 in Lipps and Tolhoek 1954b). For 100% circular polarisation of the incident photon $P_2^{(\pm)} = \pm 1$ and the spin contribution can be isolated if the difference cross section for two different bands of circularly polarised radiation (CPR) is formed, the charge term cancels as it is independent of P_2.

$$
\begin{aligned}
\left(\frac{d\sigma}{d\Omega}\right)_- &- \left(\frac{d\sigma}{d\Omega}\right)_+ = \left(\frac{d\sigma}{d\Omega}\right)^\Delta \\
&= \frac{r_0^2 n(\mathbf{p})}{2}\left(4\frac{\hbar\omega_1}{m_0 c^2}(1 - \cos\phi)\mathbf{S}(\mathbf{p}).(\hat{\mathbf{k}_1}\cos\phi + \hat{\mathbf{k}_2})\right)
\end{aligned} \tag{1.48}
$$

Platzman and Tzoar (1970) chose the the electron spin and $\hat{\mathbf{k}_1}$ to be parallel to the z-axis, such that, $\mathbf{S}(\mathbf{p}).\hat{\mathbf{k}_1} = s_z$ and $\mathbf{S}(\mathbf{p}).\hat{\mathbf{k}_2} = s_z\cos\phi$ therefore,

$$
\left(\frac{d\sigma}{d\Omega}\right)^\Delta = r_0^2 n(\mathbf{p})\left(4\frac{\hbar\omega_1}{m_0 c^2}(1 - \cos\phi)\cos\phi\right)s_z \tag{1.49}
$$

where s_z is the z component of the spin operation $\mathbf{S}(\mathbf{p})$. The double differential cross section is obtained in the usual way (see section 1.3) as,

$$\left(\frac{d^2\sigma}{d\Omega d\omega}\right)^\Delta = 4\frac{\hbar\omega_1}{m_0c^2}G_s r_0^2 \int f\left|< f|\sum_j \exp(i\mathbf{K}\cdot\mathbf{r}_j)s_z|i >\right|^2 \delta\left(\omega - \frac{|\mathbf{K}|^2}{2m_0} - \frac{\mathbf{K}\cdot\mathbf{p}}{m_0}\right)dp_x\,dp_y \quad (1.50)$$

where $G_s = (1 - \cos\phi)\cos\phi$ is the geometrical factor associated with the spin contribution,

$$= \left(\frac{d\sigma}{d\Omega}\right)^\Delta_{spin} \int \sum_j (n_{j\uparrow}(\mathbf{p}) - n_{j\downarrow}(\mathbf{p}))\delta\left(\omega - \frac{|\mathbf{K}|^2}{2m_0} - \frac{\mathbf{K}\cdot\mathbf{p}}{m_0}\right)dp_x\,dp_y \quad (1.51)$$

where,

$$\left(\frac{d\sigma}{d\Omega}\right)^\Delta_{spin} = 4\frac{r_0^2\hbar\omega_1}{m_0c^2}G_s \quad (1.52)$$

and

$$\int \sum_j (n_{j\uparrow}(\mathbf{p}) - n_{j\downarrow}(\mathbf{p}))\,dp_x\,dp_y = J_{mag}(p_z) \quad (1.53)$$

$n_{j\uparrow}(\mathbf{p})$ and $n_{j\downarrow}(\mathbf{p})$ are the momentum densities of spin up (majority band) and spin down (minority band) electrons respectively. Therefore the magnetic Compton profile $J_{mag}(p_z)$ is a 1-dimensional projection of the 3-dimensional density distribution of the unpaired electron spins. The term $(d\sigma/d\Omega)^\Delta_{spin}$ contributes $\sim z\hbar\omega_1/m_0c^2$ to the total cross section where z is the fraction of unpaired spins (for example $z = 2.2/26$ in iron and 0.7/28 in nickel) and will be largest for $\phi = 180°$ and ω_1 large (Holt and Cooper, 1983). This is illustrated by figure 1.5 which shows (b) the Klein Nishina cross section as a function of scattering angle for various values of ω_1 and (a) the ratio of the spin dependent cross section $d\sigma_{spin}$ to the ordinary Klein Nishina cross section $d\sigma_{K-N}$ of equation 1.11. The figure demonstrates the for $d\sigma_{spin}$ to be significant compared to $d\sigma_{K-N}$ necessitates $\phi \sim 180°$ and $\omega_1 > 25$keV.

1.5.2 Orbital Scattering.

In certain magnetic materials a substantial portion of the magnetisation can arise from the orbital moment of the electron and the net magnetisation is composed of both spin and orbital components. It was suggested earlier that the spin and orbital magnetisation densities could be measured individually by careful choice of experimental parameters. Choosing $\mathbf{L}(\mathbf{p})$ and $\mathbf{k}_1$ to be parallel to the z-axis as for in the spin case, the geometrical factor associated with $\mathbf{L}(\mathbf{p})$ in equation 1.46 becomes $G_l = (\cos^2\phi - 1)\cos^2\frac{\phi}{2}$. Plotting G_l as a function of scattering
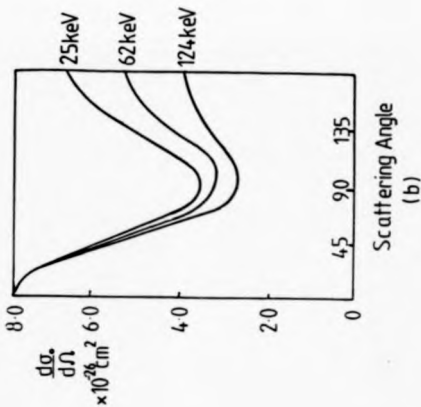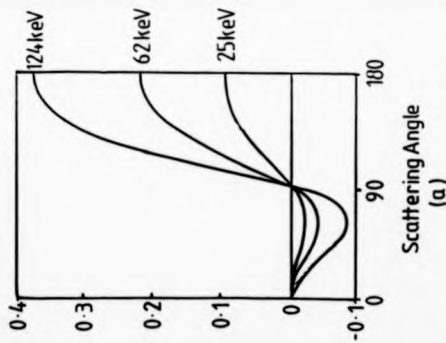
Figure 1.5 Comparison of (a) the ratio of the spin dependent Compton scattering cross section $d\sigma_s$ to the ordinary Klein Nishina cross section $d\sigma_o$ (from Holt and Cooper, 1983) and (b) the Klein Nishina cross section, equation 1.11, both as a function of scattering angle and of incident photon energy.

angle (see figure 1.6) reveals a broad maximum at $\phi \sim 70°$. Shown also in figure 1.6 is the G_s. Clearly, if a scattering angle of 90° is chosen the spin contribution to the scattering can be reduced to zero ($G_s = 0$ for $\phi = 0$) at the expense of only a small reduction ($\sim 10\%$) in G_l. Under these conditions the cross section becomes,

$$\frac{d\sigma}{d\Omega} = \frac{r_0^2}{2}n(\mathbf{p})\left(n(\mathbf{p})(1-\cos^2\phi) - \frac{2\hbar\omega_1}{m_0c^2}P_2 G_l l_z\right) \tag{1.54}$$

where l_z is the z component of the orbital momentum operator $\mathbf{L}(\mathbf{p})$. Forming the difference cross section for two different hands of CPR gives,

$$\left(\frac{d\sigma}{d\Omega}\right)_{orb}^{\Delta} = \frac{r_0^2}{2}n(\mathbf{p})\left(4\frac{\hbar\omega_1}{m_0c^2}G_l l_z\right). \tag{1.55}$$

It should be noted that $\mathbf{L}(\mathbf{p})$ is only meaningful at low energies such that $|\mathbf{k}_1| \sim |\mathbf{k}_2|$. At higher energies $\mathbf{L}(\mathbf{p})$ cannot be interpreted in terms of an orbital electron momentum. This does not rule out the possibility of studying this contribution by Compton scattering as even for $\omega_1 = 60\text{keV}$ $|\mathbf{k}_1|$ may still be sufficiently close to $|\mathbf{k}_2|$.

1.6 Summary

An outline of the theoretical aspects of the Compton scattering process have been presented and the physical conditions under which the measured inelastic scattering cross section can be simply related to the ground state electron momentum distribution of the system have been discussed. A relativistic Compton cross section is quoted. This cross section is appropriate to experiments undertaken with γ-ray sources and suitable for use as a correction function for experiments performed with unpolarised photons.

The analysis is extended to include the polarisation states of the photon and the electron before the interaction. Stokes parameters are employed to describe the initial polarisation of the photon and using density matrix theory a general form of the scattering cross section valid for any arbitrary photon polarisation is obtained. From this cross section the double differential difference cross section for two opposite hands of CPR is formed for pure spin and for pure orbital scattering. The difference cross section for spin scattering, equation 1.51

21
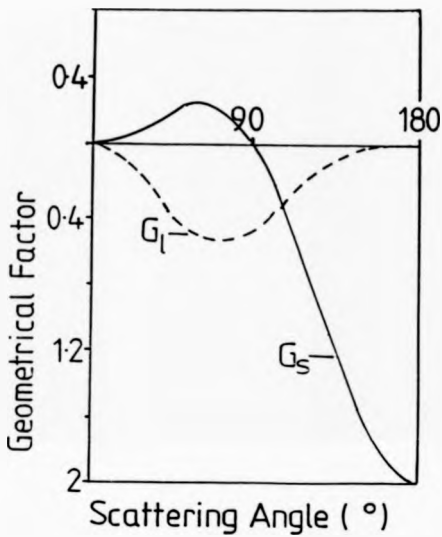
Figure 1.6 Geometrical factors associated with spin (G_s) and orbital (G_l) scattering plotted as a function of scattering angle ϕ. Note at $\phi=90°$ $G_s=0$

is the energy dependent cross section correction function used to correct all the magnetic Compton profiles presented in this thesis.

The next two chapters of this thesis are concerned with obtaining information about the total electron momentum density distribution of materials using unpolarised γ-rays produced by radioisotope sources. The experimental technique employed and the various corrections made to the energy spectra obtained is described in the next chapter. Results on $Fe_{0.7}Ni_{0.3}$, GaAs and Pb are presented in chapter 3. The remaining chapters are dedicated to the study of the momentum density distribution of the unpaired electrons in the magnetised ferromagnetic iron and cobalt. These experiments were performed with circularly polarised synchrotron radiation extracted from the SRS at Daresbury Laboratory.

Chapter 2

ELECTRON MOMENTUM DENSITY AND
GAMMA RAY COMPTON SCATTERING.

2.1 Introduction.

Since the advent of energy dispersive solid state detectors, (some 20 years ago) high en-
ergy (ω_1 >50keV) γ-ray Compton spectroscopy has become an established technique for
determining the momentum distribution of electrons in condensed matter. Existing γ-ray
spectrometers generally employ one of two radioisotope sources: ^{241}Am, which is a low en-
ergy source (60keV) or ^{198}Au which offers a higher photon energy (412keV). The low and high
energy spectrometers used in this study are described in section 2.4. Photoelectric absorp-
tion and IA considerations limit the former to studying low density materials, for an example
see Holt's study of bonding in hydrocarbons (1978). The latter was primarily developed for
studying the directional dependence of $n(p)$ for the 3-d transition metals (see Cooper, 1985
for a review) where the high energy transfers offered (> 250keV) ensure the validity of the
IA, although studies of heavy elements (for example Pb and Au) have also been successfully
made (see Pattison and Schneider, 1979). Detailed and comprehensive descriptions of the
technique of γ-ray Compton scattering can be found in recent Compton scattering thesis by
Holt (1978), Rollason (1984) and Cardwell (1987) and in the monograph edited by Williams
(1977). Therefore, only an introduction is given here.

This chapter begins by describing the complementarity between real and momentum

space wavefunctions. In the following sections the momentum space behaviour of electrons in various systems (for example, freeatoms, metals etc.) and the effect of this behaviour on the Compton profile is discussed. Also included is a brief description of the experimental spectrometers employed in this study and the manipulative data processing procedures used to extract $J(p_z)$ from the measured energy spectrum. Finally, recent improvements to the data processing procedures are discussed in detail.

2.2 The Relationship of Position and Momentum Space.

The information obtained in Compton spectroscopy is complementary to the results of charge density measurements such as X-ray diffraction, because in quantum mechanics, the position and momentum distributions of a physical system are related by the Dirac transformation,

$$\chi_j(p) = \frac{1}{(2\pi)^{\frac{3}{2}}} \int \psi(r_j) \exp(-ip_j.r_j) dr. \tag{2.1}$$

Here $\chi_j(p)$ and $\psi(r_j)$ are the momentum and real space one electron wavefunctions of the jth electron. As $\chi_j^*(p)\chi_j(p)$ is the probability distribution of the jth electron in momentum space, the total momentum density distribution of a many electron system $n(p)$ is given by,

$$n(p) = \sum_j \chi_j^*(p)\chi_j(p) = \sum_j \left| \int \psi_j(r) \exp(ip_j.r_j) dr \right|^2. \tag{2.2}$$

In diffraction experiments the charge density, $\rho(r)$ is obtained by Fourier transforming the measured form factors, $f(K)$. Similarly, it is possible to form a real space representation of $J(p_z)$ by defining a reciprocal form factor, $B(r)$ which is the Fourier transform of $n(p)$, i.e.

$$B(r) = \int n(p) \exp(-ip.r) dp. \tag{2.3}$$

Expressing $B(r)$ and $f(K)$ as autocorrelation functions gives,

$$B(r) = \int \psi^*(r')\psi(r' + r) dr', \tag{2.4}$$

24

$$f(\mathbf{K}) = \int \chi^*(\mathbf{p})\chi(\mathbf{p} + \mathbf{K})d\mathbf{p}, \tag{2.5}$$

where both functions are subject to the normalisation rule, $f(0) = B(0) = Z$.

The quantity $B(r)$ is more commonly termed the 'B-function' and was introduced into Compton scattering by Pattison, Weyrich and Williams (1977). Compton experiments yield only a 1-dimensional projection of $n(\mathbf{p})$ along the z-direction and it is convenient to form $B(z)$ which is the Fourier transform of $J(p_z)$ (see Pattison et al, 1977), i.e.

$$B(z) = \int\int\int n(p_x, p_y, p_z)\exp(-ip_z z)dp_x dp_y dp_z = \int J(p_z)\exp(-ip_z z)dp_z. \tag{2.6}$$

Closer examination of equations 2.4 and 2.6 reveals that the core electrons contribute to the overlap integral only at small displacements, r whereas the dominant contribution to $B(r)$ arises from free, spatially extended valence electrons. This is in contrast to diffraction studies where it is the highly localised core electrons which constitute the dominant contribution to $f(\mathbf{K})$ (see equation 2.5). The valence electrons only contribute to $f(\mathbf{K})$ at low $\mathbf{K}$ values and unlike $B(z)$, which is a continuous function, $f(\mathbf{K})$ can only be measured at Bragg peaks.

Compton profile studies of metals are usually interpreted in terms of the quantity $J(p_z)$ because of its sensitivity to the behaviour of the delocalised conduction electrons and to the effects of electron electron correlations. However, for bonded materials such as semiconductors, the B-function is a more informative representation of the measured energy spectrum than $J(p_z)$, providing specific information about the bonding (see section 2.3.3).

Figure 2.1 (taken from Cooper, 1985) shows how the Dirac transformation, equation 2.1 enables various electron density functions in real (r) and momentum (p) space may be related to one another. It should be pointed out that although knowledge of real and position space wavefunctions enables the charge and momentum density distributions to be derived, the converse is not true. It is not possible to determine $n(\mathbf{p})$ from $\rho(\mathbf{r})$ (or visa versa) without the necessary phase information of the wavefunctions which is lost on formation of the products $\psi^*(\mathbf{r})\psi(\mathbf{r})$ and $\chi^*(\mathbf{p})\chi(\mathbf{p})$.
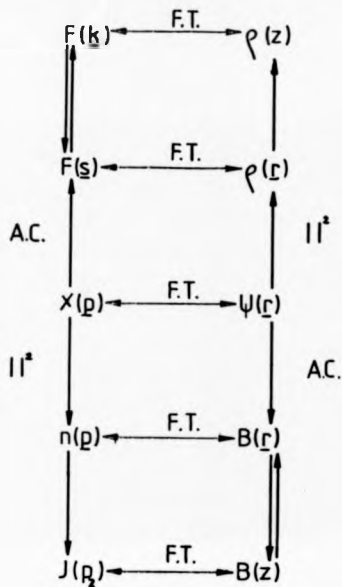
Figure 2.1 The Fourier relationship between various electron density functions in position and momentum space for one electron wavefunctions, where FT represents a Fourier transformation. As indicated, the above properties are derived by the operations of autocorrelation (AC) and squaring the modulus ($||^2$). These operations are irreversible and therefore it is not possible to relate charge density measurements to Compton profile measurements.

2.3 Electron Momentum Distributions.

2.3.1 Free Atoms.

The Compton profile for a single free atom of Fe $(1s^2, 2s^2, 2p^6, 3s^2, 3p^6, 4s^2, 3d^6)$ is shown in figure 2.2. This was calculated numerically in the non-relativistic Hartree Fock approximation from a basis set of independent one electron wavefunctions by Biggs, Mendelsohn and Mann, (1975). The contributions to the total profile from the separate K, L, M and N shells are clearly shown (each has been normalised to the number of contributing electrons) and are the result of the separation of the total electron density into single electron wavefunctions. The corresponding free atom Compton profile of an alloy or molecule would be a composite profile composed from appropriate contributions from electrons belonging to each constituent.

It is apparent from figure 2.2, that the valence electron and core electron contributions to the profile are quite different, the valence electron contribution is a prominent feature, localised about the profile origin whereas the core electron contribution is a relatively flat background extending to high momentum. In general, the independent electron model is unable to provide an accurate description of the valence electron density (except in the inert gases, see Eisenberger and Reed, 1972) as electron correlation and exchange give rise to significant perturbations of the valence electron wavefunctions.

When an atom is 'bound' (i.e. in a solid or molecule), the valence electron contribution to the Compton profile will reflect changes in the electron momentum distribution which occur as a consequence of delocalisation or bond formation. However, the core electron wavefunctions are relatively unaffected by the effects of bond formation and consequently Hartree-Fock free atom Compton profiles can be used to represent core electron momentum distribution. For conduction and valence electrons a more sophisticated representation of the electron density required.

2.3.2 Metals and Metal Alloys.

The simplest theoretical model of an ordered metal alloy describes the electron density as a Hartree-Fock free atom core plus a conduction band formed from a non-interacting, homo-
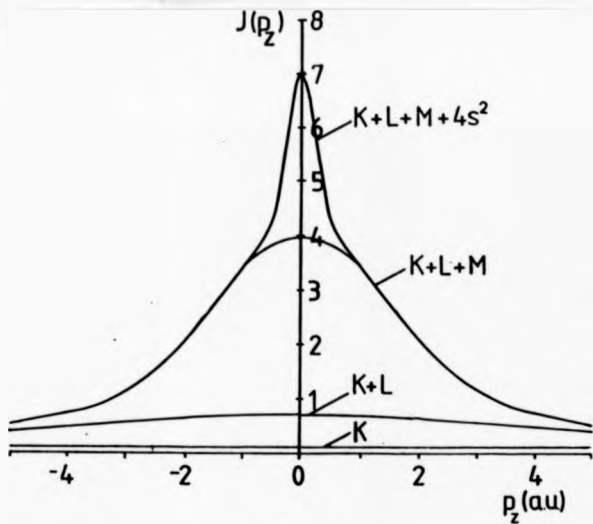
Figure 2.2 The free atom Compton profile of Fe (Z=26) calculated numerically in the non-relativistic Hartree Fock approximation (Biggs et al, 1975). The separate contributions from the individual electron shells are also shown.

geneous, free electron gas. The ground state free electron Fermi distribution is a sphere of radius p_f, with all states below the Fermi surface uniformly occupied (i.e. $n(p)$=constant) and all states outside unoccupied (i.e. $n(p) = 0$). The resulting Compton profile is an inverted parabola of the form,

$$J(p_z) = \begin{cases} \frac{3n}{4} \frac{p_f^2 - p_z^2}{p_f^3} & \text{if } p_z \leq p_f \\ 0 & \text{otherwise} \end{cases} \tag{2.7}$$

where n is the number of conduction electrons (e.g. 8.6 for $Fe_{0.7}Ni_{0.3}$).

The free electron model is a reasonable approximation for metals with a low density of conduction electrons, for example the alkali metals (see Phillips and Weiss, 1968) and the light metals, Al and Mg (see Cooper, Pattison, Williams and Pandey, 1974). However, deviations from free electron behaviour arise as a consequence of electron-electron interactions (electron correlations) and interactions between the electron and the ion cores (band effects). The effect of electron correlations is to promote electrons from momentum states within the Fermi sphere to momentum states outside the Fermi sphere. This affects the Compton profile by reducing the size of the discontinuity at $p_z = p_f$ and producing a characteristic high momentum tail, as shown in figure 2.3a.

In real metals and alloys the conduction electron wavefunctions are weakly perturbed by the periodic potential of the ion cores and may be regarded as 'nearly free'. In this model the electron wavefunctions, $\psi_k(r)$ are represented by a series expansion of Bloch functions, $U_k(r)$, i.e.

$$\psi_k(r) = U_k(r) \exp(\imath k.r) \tag{2.8}$$

where $U_k(r) = \sum_G a_G(k) \exp(\imath G.r)$, G is a reciprocal lattice vector and $a_G(k)$ are the expansion coefficients. The momentum space wavefunction, $\chi_k(p)$ is obtained by Fourier transforming $\psi_k(r)$ as,

$$\chi_k(p) = \int \sum_G a_G(k)(\exp(\imath (k + G).r) \exp(-\imath p.r))dr = \sum_G a_G(k)\delta(p - k - G). \tag{2.9}$$

27

Figure 2.3 (a) The effect of electron correlation on the Compton profile of a homogeneous free electron gas (solid line) and (b) the Seitz model for nearly free electrons in a square lattice. The effect of band structure is to promote electrons from a state k to a state $k + G$. This results in a similar but in general more significant broadening of the profile than that resulting from the effects of electron correlation.
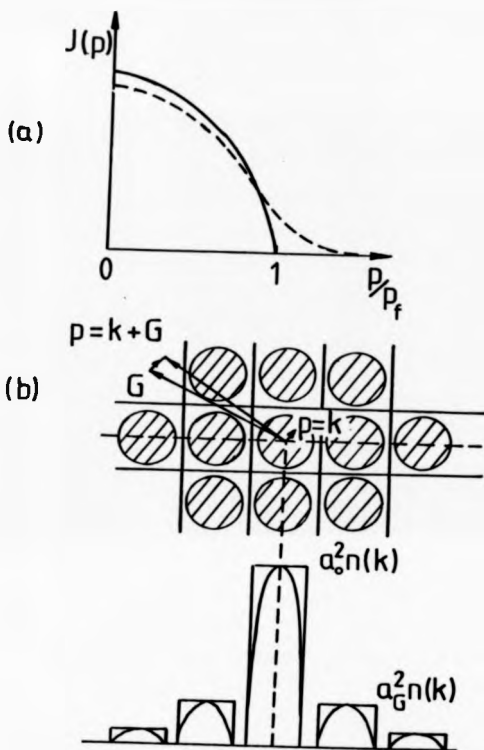
From the above equation it is apparent that there is a contribution from an electron in state $\mathbf{k}$ to $\chi_k(\mathbf{p})$ at momentum $\mathbf{p} = \mathbf{k} + \mathbf{G}$, for all $\mathbf{G}$, of an amount $a_G(\mathbf{k})$. Thus the effect of band structure is to introduce high order components into $\chi_G(\mathbf{k})$, which in turn leads to a broadening in the Compton profile. This broadening is similar but generally more significant than that resulting from the effects of electron correlation.

It can be shown (for example see Rollason, 1984 or Cardwell, 1987), that for a nearly free electron metal, the Seitz model predicts a Compton profile comprising of a central parabola plus a series of equidistant but rapidly diminishing parabolas, which are weighted according to the probability of finding an electron in a high order momentum state, i.e. $|a_G(\mathbf{k})|^2$ (see figure 2.3b). However, the Seitz band model takes no account of exchange or correlation effects. Modern day band theories use the one electron model as their starting point and include all other crystal effects in an effective potential energy, $V(\mathbf{r})$ in the one electron Schrödinger equation. The Schrödinger equation is then solved to find the individual electron wavefunctions.

2.3.3 Semiconductors.

An area where Compton scattering is particularly effective is the study of bonding in solids and molecules. In tetrahedrally bonded semiconductors such as GaAs, ZnSe etc. the bonding is often described as being covalent with a degree of ionicity. A purely covalent solid may be considered as having directional bonds and the valence electrons are drawn into these bonds. The greater the localisation of these electrons in the bond, the greater the anisotropy in the momentum density distribution. An ionic solid may be considered as being composed of two highly charged spheres. In this case, the charge density and hence the momentum density are isotropic. Therefore, by measuring the anisotropy of the electron momentum density, which in a Compton experiment is achieved by measuring the directional difference profiles,

$$\Delta J(p_z)_{aniso} = J_{hkl}(p_z) - J_{h'k'l'}(p_z), \tag{2.10}$$

it is possible to obtain information about bonds and also about the degree of ionicity of the solid. For example, figure 2.4 shows the Compton profile anisotropy 111-110 of diamond
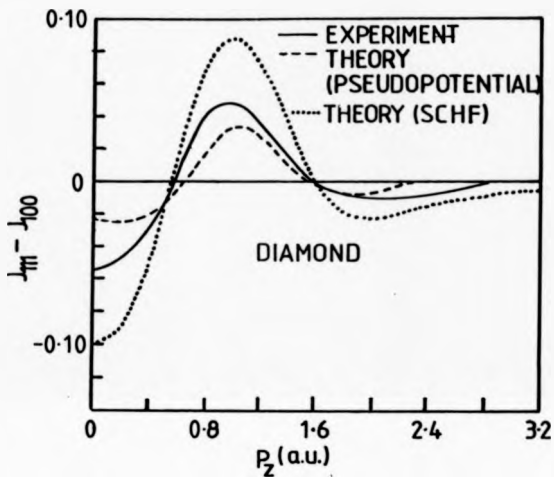
Figure 2.4 The anisotropy in the Compton profile of diamond, $J_{111}(p_z) - J_{100}(p_z)$ (after Reed, Eisenberger, Pandey and Snyder, 1974).

measured by Reed and Eisenberger, (1972) together with the momentum anisotropy predicted by self consistent crystalline Hartree-Fock (SCHF) calculation (Wepfer, Euwema, Surrat and Wilhite (1974)) and that predicted by a pseudopotential calculation by Pandey (1973). From figure 2.4 it is apparent that the pseudopotential calculation underestimates and the SCHF calculation overestimates the scale of the anisotropy. According to Reed, Eisenberger, Pandey and Snyder (1974) this is because the pseudopotential calculation, which starts with a plane wave description of the electron wavefunctions, has not produced a sufficiently localised bond, whereas the SCHF method, which starts with localised atomic orbitals, has not produced a sufficiently diffuse bond. From this example it is apparent that Compton scattering is indeed a sensitive test of band theory and a stringent test of the electron wavefunctions used in band theory calculations.

B-functions of Semiconductors.

Pattison and Schneider (1973) have shown that for semiconducting materials, it can be more informative to analyse Compton scattering data in real space using the B-function (equation 2.6). This representation has the following advantages. Firstly it is conceptually simpler to interpret experimental results in position rather than momentum space. In addition the Gaussian resolution of the experimental data is transformed to a simple multiplicative Gaussian damping factor. More importantly, on transforming to real space, slowly varying functions of momentum for example, residual systematic errors and the uninteresting core electron contribution to $J(p_z)$ are restricted to a small region around the origin of $B(r)$.

For a crystalline solid the overlap integral (equation 2.4) may be written in terms of Bloch functions for the electrons in a particular band. Summing over all k states in each occupied band gives,

$$B(r) = \sum_{k,\mu} n_\mu(k) \int \psi_k^*(r + r')\psi_k(r')dr' \tag{2.11}$$

where $n_\mu(k)$ is the occupation number of the kth state in the μth band. Schülke (1977) showed that by expanding this equation in terms of one electron Bloch functions and evaluating $B(r)$ for any real lattice translation vector $r = R_L$ gives,

$$B(\mathbf{R}_L) = \frac{2}{V_{BZ}} \int_{BZ} n_p(\mathbf{k}) \exp(-i\mathbf{k}\cdot\mathbf{R}_L) d\mathbf{k} \qquad (2.12)$$

where V_{BZ} is the volume of the Brillouin zone. This result is equivalent to the theorem of Lock, Crisp and West (1973) used to reconstruct Fermi surfaces from positron annihilation angular correlation data.

In the case of insulators, all bands are filled and n(k)=constant. Therefore $B(\mathbf{r}) = 0$ for all $\mathbf{r} = \mathbf{R}_L$ and hence the B-function of an insulator will cross the real space axis at all points corresponding to lattice translations. This is illustrated in figure 2.5 which shows the experimental B-functions of Ge and Si taken from Pattison and Schneider (1978). The results clearly show zero passages at $\frac{1}{2}a_{110}$ and even illustrate the small difference (~4%) between the lattice parameters of Si and Ge. The main value of this result is not in the determination of the lattice parameters but in the checks on experiment and theory that it enables for insulators. The experimental zero crossing points of $B(\mathbf{r})$ will be unaffected by the resolution damping and their correct location is a valuable check of the data processing procedure. For theoretical models, the location of lattice zeros provides a stringent test of the extent of the orthogonalisation of the one electron wavefunctions used in the calculation (for example see Pattison and Weyrich, 1979). Other zero passages in figure 2.5 are related to the particular form of the Bloch wavefunctions. The behaviour of the B-function between lattice zeros i.e. its size and sign, may under certain circumstances provide information about the type of bonding between the different elements in an atomic chain. For example, in a study of LiH, Pattison and Weyrich, 1979 noted that a large negative area between lattice zeros implied a region dominated by antibonding orbitals and a large positive area, a region dominated by bonding orbitals.

2.4 Experimental Spectrometers.

The low energy (ω_1=60keV) and high energy (ω_1=412keV) γ-ray Compton spectrometers employed for the non-magnetic Compton studies presented in this thesis are shown schematically in figures 2.6a and 2.6b respectively. The design and experimental details of these spectrom-
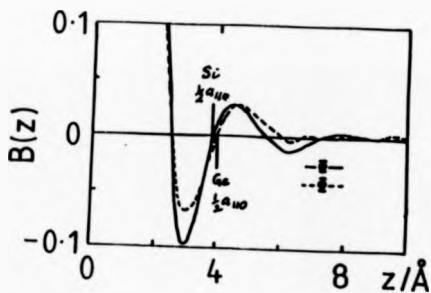
Figure 2.6 The reciprocal form factor, $B(z)$ along the 110 direction in Ge and Si obtained from Compton profile measurements with 412keV γ-radiation by Pattison and Schneider (1978).

60 KEV GAMMA RAY COMPTON SPECTROMETER
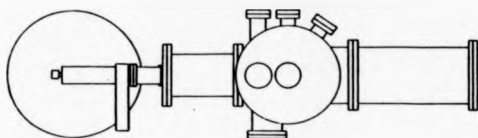
scale
cm   0   10   20   30   40   50

(a)

412 KEV GAMMA RAY COMPTON SPECTROMETER
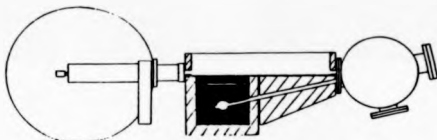
scale
cm   0   10   20   30   40

(b)

Figure 2.0 Schematic diagrams of the Compton spectrometers used during this study. (a) The low energy [241]Am spectrometer (60keV) and (b) the high energy [198]Au spectrometer (412keV).

eters can be found elsewhere (60keV–Holt, 1978, 412keV–Rollason, 1984) and therefore only an outline is given here.

The low energy spectrometer was designed around the use of a 5Ci ^{241}Am annular γ-source, (E_γ=59.54keV) and is located at the University of Warwick. The annular source geometry was chosen to reduce self absorption and hence increase the surface activity of the source. Unfortunately, with this construction it is no longer possible to define uniquely the scattering vector, as K can lie anywhere on the surface of a cone of semi-angle $\sim 5°$ (see Aikala, 1982). Therefore, this spectrometer is not entirely suitable for studying the true directional dependence of $n(p)$ because the directional Compton profiles obtained are averaged over all the crystal directions which lie on the surface of the cone. Although true directional profiles cannot be obtained, fortunately $n(p)$ is relatively isotropic over the range of variance ($\pm 5°$) and the measured directional difference profiles tend to be in agreement with results obtained using a planar source geometry (see chapter 3). The scattering angle of this spectrometer is fixed at 170.5° and with ω_1=59.54keV, the resulting energy transfer, E_{trans} is 11.18keV, i.e. ω_2=48.36keV. The beam cross section is $\sim 530mm^2$ at the sample position, although due to scattered beam collimation the detector sees only an area of 250mm^2. The detector sample separation is 195mm.

The high energy spectrometer is located at the Rutherford Appleton Laboratory and contains a planar, high energy (ω_1=411.80keV), ^{198}Au γ-source. The gold source is composed of a sandwich of 2 gold foils and has dimensions of 6.5mm×2.5mm area, 2mm thick. Immediately prior to each study the source is activated by neutron bombardment, to an initial activity of 150–200Ci, in the DIDO reactor at Harwell (Holt, Cooper, DuBard, Forsyth, Jones and Knights, 1979). This source produces usable intensity for about 12–14 days (the half-life of ^{198}Au is $\sim$2.7days). The spectrometer scattering angle was chosen to be 167°. This enables the detector response function to be measured at the Compton profile peak (ω_2=158.94keV) using a weak ^{123m}Te γ-source (E_γ=159.00keV). The sample detector separation is 484mm and the cross-sectional area of the beam at the sample position is $\sim$250mm^2. Both spectrometers are evacuated (10^{-6} Torr) to reduce air scattering and employ an intrinsic Ge solid state detector to detect the scattered photons and a 4096 multichannel analyser (MCA) coupled to

a personal computer to record, display and manipulate the scattered energy spectra. In both cases the experimental areas are air conditioned to minimise drift in the detector electronics.

Prior to the studies presented in this thesis the following minor alterations to the high energy spectrometer were made; a He–Ne laser was used to accurately define the position and height of the sample centre and the brass sample holder, used in previous studies, was replaced with a perspex holder (low scattering cross section). The result of these simple alterations was an improvement in the Compton count rate of ∼50%.

2.5 Data Reduction and Analysis.

A comprehensive description of the Compton data analysis procedure used to analyse the γ-ray Compton data presented in this thesis can be found elsewhere (see Rollason (1984) and Cardwell (1987)) and therefore only an outline is presented here. However, during this period of research several alterations and improvements were made to the data processing, namely;

- The order of application of the energy dependent corrections was altered.

- A more accurate detector efficiency correction for the high energy spectrometer was formulated based on the prediction of a Monte Carlo simulation of the detector efficiency.

- The existing background correction was modified to remove systematic errors resulting from source independent background radiation.

- The detector response function of the high energy spectrometer was remeasured under conditions which closely resembled the true experimental configuration.

Although the effect of each correction on the final line shape is generally small (typically $< 2\%J(0)$), their application enables the small differences between directional Compton profiles (typically ∼1% for GaAs) to be resolved. These differences, presented in the form of anisotropies are used to provide a critical test of the ability of band calculations to model the electron momentum density.

2.5.1   Outline of the Data Processing.

In the limit of high momentum transfers, the double differential scattering cross section, $D(\omega)$ can be written in terms of the scattered photon energy, ω as,

$$D(\omega) = C(\omega)J(p_z) \qquad (2.13)$$

where $C(\omega)$ is the Ribberfors cross section (equation 1.22). The aim of the Compton data analysis procedure described in this section is to extract $D(\omega)$ from the measured energy distribution, $M(\omega)$. This is achieved by the removal of energy dependent effects which are either determined by the spectrometer design (i.e. detector response, spectrometer response and the background), or by the sample characteristics and the incident photon energy (i.e beam attenuation, multiple scattering and the geometrical resolution). To remove these effects from $M(\omega)$ requires the application of various correction procedures which are either additive, factoral or convolutive. The measured energy spectrum may be described in terms of these corrections as,

$$M(\omega) = R(\omega) \ast E(\omega) \ast S(\omega) \ast A(\omega)[D(\omega) + B(\omega)] \qquad (2.14)$$

where $\ast$ represents a convolution and each correction is defined in figure 2.7. The Compton profile $J(p_z)$ can be extracted from $M(\omega)$ using the following expression which is formulated by rearrangement of equations 2.13 and 2.14, i.e.

$$J(p_z) = NC^{-1}(\omega)A^{-1}(\omega)S^{-1}(\omega) \ast G^{-1}(\omega) \ast E^{-1}(\omega)R^{-1}(\omega)[M(\omega) - B(\omega)] \qquad (2.15)$$

This expression may be interpreted as a series of correction procedures implemented in the reverse order of occurrence (i.e. detector effects are removed first, source effects are removed last) as shown in figure 2.7 for a Compton measurement performed with the high energy spectrometer. The source of each correction in figure 2.7 is identified in table 2.1. Fortunately it is unnecessary to repeat all the measurements and calculations listed in table 2.1 for every Compton study as it is sufficient to repeat the preliminary measurements periodically to

1	Background subtraction	$M(\omega) - B(\omega)$
2	Deconvolution of resolution function	$R(\omega)$
3	Detector efficiency correction	$E(\omega)$
4	Deconvolution of geometrical broadening function	$G(\omega)$
5	Deconvolution of source broadening fuction	$S(\omega)$
6	Absorption correction	$A(\omega)$
7	Cross-section correction	$C(\omega)$
8	Normalisation	N
9	Multiple scattering correction	$J_{multiple}(p_z)$
	Corrected Compton profile	$J(p_z)$

Figure 2.7 The data reduction procedure used to extract $J(p_z)$ from the measured energy spectrum, $M(\omega)$.

	Correction	Subject
Preliminary system measurements	1. Detector efficiency fn., $E(\omega)$	Ba source spectrum
	2. Detector resolution fn., $R(\omega)$	Te source spectrum
Subsiduary calculations	1. Geometrical broadening, $G(\omega)$	Spectrometer collimation
	2. Absorption, $A(\omega)$	Sample density
	3. Source broadening fn., $S(\omega)$	Source geometry
	4. Normalisation, N	Free atom profile
	5. Multiple profile, $J^{multiple}(p_z)$	Sample geometry
Experimental measurements	1. Data, $M(\omega)$	Sample spectrum
	2. Exposure ratio, signal:noise	Exposure timings
	3. Static background, $B_{ST}(\omega)$	Background spectrum, no source
	4. Total background, $B(\omega)$	Background spectrum, with source

Table 2.1 Origin of the corrections used to analyse Compton data measured on the high energy spectrometer system.

assess any changes in the detector response. The subsidiary calculations and measurements listed in table 2.1 are specific to a particular sample and have to be recalculated or remeasured for each Compton profile measurement.

The correction for multiple scattering is applied after the correction procedure given by equation 2.15 (see figure 2.7). At this stage the area of $J(p_z)$ is necessarily equal to the number of electrons, Z, (equation 1.5) and the contribution from multiple scattering is removed from $J(p_z)$ by the following procedure,

$$J(p_z)_{single} = \alpha \; J(p_z)_{total} - J(p_z)_{multiple} \qquad (2.16)$$

where $\alpha = \frac{\int J(p_z)_{single} dp_z - \int J(p_z)_{multiple} dp_z}{\int J(p_z)_{single} dp_z}$. The contribution from multiple scattering is dependent upon the sample composition and scattering geometry and can account for 15–30% of the measured profile, $J(p_z)_{total}$. A Monte-Carlo simulation of the scattering (originally developed by Felsteiner, Pattison and Cooper, 1974) is used to evaluate the multiple profile $J(p_z)_{multiple}$ which is typically a broad, featureless, asymmetrical function of energy. The simulated spectral distribution of 412keV photons which have been multiply scattered from an iron nickel alloy sample (the spectral distributions for 60keV photons are very similar) is shown in figure 2.8. The dashed line in figure 2.8 represents a cubic spline fit to $J(p_z)_{multiple}$ which is employed to remove random statistical fluctuations from $J(p_z)_{multiple}$. This fit has necessarily the same area as $J(p_z)_{multiple}$ and is used to correct the measured Compton profile.

The general reduction procedure outlined in figure 2.7 is also applicable to Compton data measured with the low energy spectrometer. However within the energy regime of the low energy spectrometer, the detector efficiency remains relatively unchanged (<1% variation) and the correction $R(\omega)$ can be assumed negligible. Also in view of the long half life of the ^{241}Am, a static background correction, $B_{ST}(\omega)$ (see section 2.6.3) is unnecessary.

Unfortunately the design of the low energy spectrometer limits the precision of certain correction procedures. For example, exact calculations of $G(\omega)$ and $S(\omega)$ are not possible in view of the complex nature of the source geometry (i.e. annular source) and as a result, residual systematic errors of upto $\sim 5\%J(0)$ remain on the low energy side of the final processed Compton profile. Further additional systematic errors can arise if the small energy
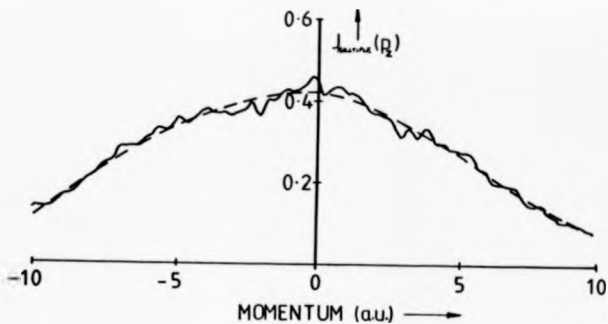
Figure 2.8 The spectral distribution of 412keV radiation multiply scattered from an iron nickel alloy sample. The dashed line is a cubic spline fit to this data.

transfer offered by this spectrometer, i.e. 11.18keV is insufficient to ensure the validity of the IA (see section 1.3.3) for all the atomic electrons involved. In addition, the normalisation condition, equation 1.5 will be no longer applicable.

For the reasons above Compton profiles obtained from the low energy spectrometer are only compared with theory after the residual systematic errors have been reduced by the formation of directional difference profiles. The high energy spectrometer offers the better momentum resolution (typically 0.4a.u. compared with 0.57a.u. for ^{241}Am) and the processed Compton lineshapes generally exhibit sufficient profile symmetry to enable interpretation of the individual profiles as well as the directional differences, (for example, measurements on iron see Rollason, Holt and Cooper, 1983, nickel see Rollason, Schneider, Laundy, Holt and Cooper, 1987 and Chromium see Cardwell and Cooper, 1989).

As the statistical accuracy of Compton profile measurements has improved, (for the high energy spectrometer the statistical errors were $\sim 0.5\%J(0)$ at the start of this research and are currently $\sim 0.2\%J(0)$), it is necessary to review the data reduction procedure and the accompanying subsidiary measurements. The alterations and remeasurements undertaken during this period of research are discussed in the following section.

2.6 Developments in Data Processing.

2.6.1 The Order of the Correction Procedure.

The ideal strategy for removal of systematic errors from Compton data is given by equation 2.15, however this strategy is computationally difficult. In the past the computation has been simplified by changing the order of application of the energy dependent corrections. For this tactic to be feasible the additional errors introduced by this 'incorrectly' sequenced processing must be insignificant compared to the statistical error of the experimental data.

At the beginning of this research the sophistication of the data processing was limited by the slow, unreliable, Intertec Superbrain computer employed to perform Compton data analysis. To achieve 'realistic' processing times (~ 3 hours) it was necessary to use the following strategy, which contains only one deconvolution procedure to extract $J(p_s)$ from $M(\omega)$,

$$J(p_x) = NC^{-1}(\omega)A^{-1}(\omega)R'^{-1}(\omega) * [E(\omega)(M(\omega) - B(\omega))]. \tag{2.17}$$

The correction $R'^{-1}(\omega)$ represents the composite spectrometer response function, $S(\omega) *$ $R(\omega)$, (i.e. a convolution of the source broadening and the detector response function). The source broadening function $S(\omega)$ was calculated using a Monte Carlo simulation (developed by Rollason, private communication) of the multiple scattering within the gold source. In the above strategy, the correction for detector efficiency, $E(\omega)$ is performed before the deconvolution of $R'(\omega)$ and the overall symmetry of the processed data is only modest, i.e. $\sim 1.5\% J(0)$ (for example see Cardwell and Cooper, 1986). This asymmetry in the processed data is indicative of residual uncorrected systematic errors resulting from the incorrectly sequenced processing. To reduce these errors and thereby improve the profile symmetry the above strategy (equation 2.17) was changed to that quoted in equation 2.15. Namely, the efficiency correction is now performed after the convolution of the detector response function is removed and then a separate deconvolution procedure is employed to remove the convolution of the source broadening function with the measured energy spectrum.

To satisfy the increased computational demand, the data processing routines were adapted to run on a more powerful, Olivetti personal computer. Figure 2.9 shows the difference between a directional 100 Compton profile of FeNi alloy measured using the high energy spectrometer, after the application of the original and reordered data processing package. The effect of the reordering is to shift electron density from the left hand side (i.e. negative momentum) to the right hand side (i.e. positive momentum) of the Compton profile, thereby improving the profile symmetry.

As the detector efficiency correction for the low energy spectrometer is negligible, the processed data will be unaffected by this reordering.

2.6.2 Detector Efficiency Correction

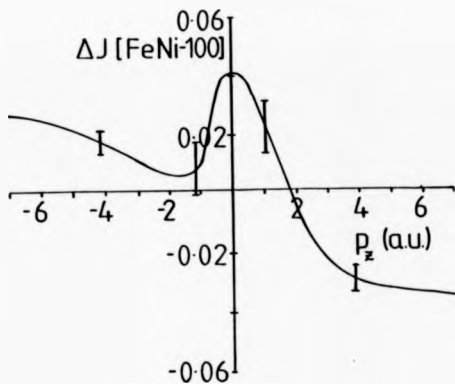The efficiency of a solid state detector to detect photons of energy, ω is defined as,

Figure 2.9 The difference between a 100 Compton profile of $Fe_{0.7}Ni_{0.3}$ measured with the high energy spectrometer and processed with the original and reordered processing procedures respectively.

$$\text{Efficiency(\%)} = \frac{\text{number of photons wholly absorbed in the detector crystal}}{\text{number of photons entering the detector crystal}} \times 100. \quad (2.18)$$

As mentioned earlier, it is unnecessary to perform a detector efficiency correction for data measured with the low energy spectrometer because at the energies involved ($< 60\text{keV}$) the detector is 100% efficient. Therefore, the efficiency correction formulated in this section is only applicable to data measured with the high energy spectrometer.

The efficiency of the solid state detector used in this study has been previously determined (Rollason, 1984) by comparing the measured intensities of the principle γ-emissions of a ^{75}Se radioisotope with predicted values of the relative intensities. The measured efficiency was fitted by substituting an effective thickness, t for the Ge detector crystal into the following simple expression,

$$E(\omega) = 1 - \exp(-\mu(\omega)t) \quad (2.19)$$

where $\mu(\omega)$ is the energy dependent photoelectric attenuation coefficient of Ge. In practice, photons are backscattered and multiply scattered out of the detector crystal, resulting in incomplete photon collection and the simple photoelectric fit given above is inadequate.

The detector efficiency at various given energies has been redetermined experimentally by comparing the measured intensities of the 8 most prominent γ-emissions of a ^{133}Ba radioisotope, with the known relative intensities of the γ-emissions obtained from Lederer, Hollander and Perlman (1967). The radiation from the source was collimated to mimic the spectrometer scattered beam collimation. The observed detector efficiencies are represented by the filled circles in figure 2.10, but unfortunately, due to the scarcity of data points in the Compton profile region, (i.e. 140–180keV) it is not possible to determine from these results alone, the energy dependence of the efficiency in this region. Also shown in figure 2.10 are a Monte-Carlo simulation of the detector efficiency (D. Laundy, private communication, open circle on solid line) and the efficiency calculated using equation 2.19 with $t=0.7\text{mm}$ (filled squares on dashed line). The Monte-Carlo simulation of the efficiency is in excellent agreement with the observed values and vindicates the use of this calculation for correcting Compton data
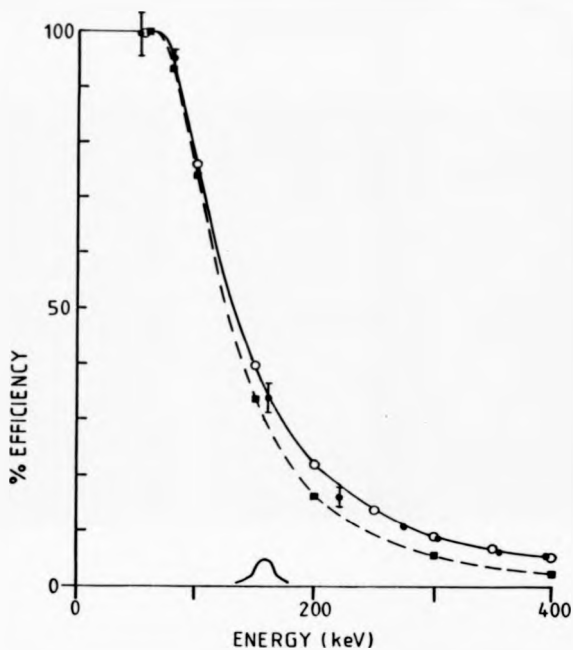
Figure 2.10 The detector efficiency deduced from the observed γ-lines of ^{133}Ba (filled circles), calculated by a Monte Carlo simulation (solid line, open circles) and calculated using equation 2.19 (dashed line, filled squares). The schematic Compton profile denotes the profile peak position for the high energy spectrometer system.

measured with the high energy spectrometer. From figure 2.10 it is apparent that as expected the detector efficiency is not governed by the simple exponential relationship which was traditionally used to correct Compton data.

In order to correct the measured intensity at each point in the profile, the efficiency correction must be in the form of an analytical function of the photon energy. The analytical expression now used in the data analysis is of the form,

$$E(\omega) = z_1 \exp(-z_2\omega) \qquad (2.20)$$

where z_1 and z_2 are constants determined from the results of the Monte-Carlo simulation of the detector efficiency (see figure 2.11).

2.6.3 Background Correction.

The measured energy spectrum $M(\omega)$ in a typical Compton experiment contains a certain degree of noise or background, $B(\omega)$ which must be removed before the remaining data reduction procedures can be implemented. This background is comprised from three main contributions: Scattering of the primary radiation from the sample holder and/or the walls of the spectrometer chamber, detection of radiation directly from the source and natural radiation e.g. cosmic rays and radiation from adjacent laboratories (the latter is more significant at RAL because the γ-lab. is situated next to many radioactive, decommissioned synchrotron magnets).

The magnitudes of the first two contributions are dependent upon the activity of the source and together form the 'dynamic background', $B_{DY}(\omega)$. The third contribution is independent of the source activity and will be termed the 'static background', $B_{ST}(\omega)$. For measurements of short duration and/or where the signal/noise ratio ($\frac{S}{N}$) is high ($> 100 : 1$), the static background contribution can be neglected. However, in a recent study on lead single crystals (see chapter 3), measurement times were long (>10 days), $\frac{S}{N}$ values were low (i.e. 15:1 (412keV), 7:1 (60keV)) and the static background formed $\sim$65% of the total background of the high energy spectrometer, ($B(\omega) = B_{ST}(\omega) + B_{DY}(\omega)$). Under these circumstances it is necessary to account for the static background contribution to both $M(\omega)$ and $B(\omega)$.
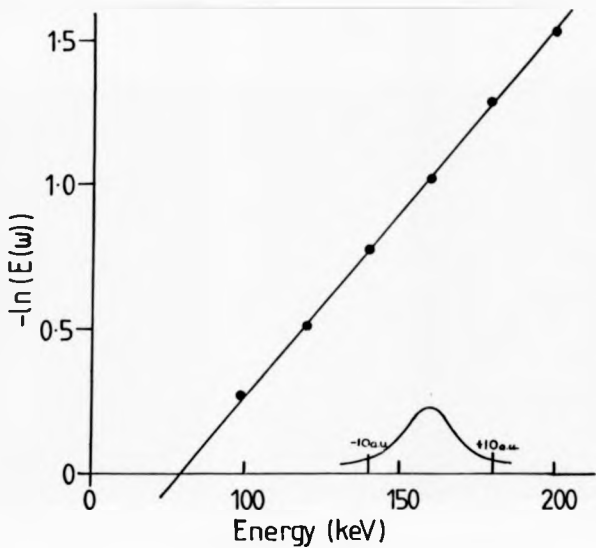
38

Figure 2.11 The detector efficiency correction function for the high energy spectrometer system, equation 2.20 which is based on the prediction of a Monte Carlo simulation of the efficiency.

Due to the long half life of ^{241}Am (458 years), measurements performed using the low energy spectrometer are not susceptible to the effects of source decay and the measured distributions $M(\omega)$ and $B(\omega)$ contain equivalent contributions from $B_{ST}(\omega)$. In this case the static background contribution is eliminated by the conventional background subtraction, i.e. $M(\omega) - bB(\omega)$, where b is a suitable normalisation constant. For measurements performed using the high energy spectrometer, it is necessary to subtract a static background from both $M(\omega)$ and $B(\omega)$ before correcting for source decay, i.e.

$$M'(\omega) = M(\omega) - b_1 B_{ST}(\omega) \tag{2.21}$$

$$B'(\omega) = B_i(\omega) - b_2 B_{ST}(\omega) \tag{2.22}$$

where $M'(\omega)$ represents the corrected raw data and replaces $M(\omega)$ in equation 2.15, b_1 and b_2 are suitable normalisation constants and $B_{ST}(\omega)$ is measured independently of the measured experiment by recording an energy spectrum with the ^{198}Au source removed. The corrected background, $B'(\omega)$ is removed from $M'(\omega)$ by a point by point subtraction.

2.6.4 The Detector Response Function.

The response of a solid state detector to a photon of energy ω_1 is not a delta function, but is composed of a characteristic, approximately Gaussian photopeak centered about ω_1 and a low energy tail falling away from the photopeak. The tail arises as a consequence of incomplete absorption of incoming radiation in the active region of the detector crystal.

An objective of the data processing is to remove the effects produced by the detector response tail from the measured data, leaving the profile with a simple Gaussian resolution. Ideally, this would be achieved by deconvoluting each point in the measured profile with a separately measured, energy dependent, detector response function. However, in the absence of a suitable, tunable, monochromatic source of radiation, the measurement of the detector response is restricted to the Compton peak energy (159keV) for the high energy spectrometer and at the primary photon energy (60keV) for the low energy spectrometer. In the latter

39

case the detector response function at 59.54keV overestimates the FWHM at the Compton peak energy (48.4keV) by ~11%, which has been estimated to correspond to the additional broadening resulting from beam divergence (see Holt, 1978).

The vindication for using a energy independent resolution function has been justified by Rollason (1984), who convoluted a symmetric free atom profile of vanadium with a variable width Gaussian and calculated the 'introduced' asymmetry to be $< 0.03\%J(0)$, i.e. more than an order of magnitude less than the statistical errors.

Both spectrometer response functions were remeasured during this period of research. Within the approximation mentioned above, the low energy spectrometer response function was unchanged and only a discussion of the high energy spectrometer response function will be given here.

The High Energy Spectrometer Response Function.

As mentioned earlier, the high energy spectrometer design is such that the Compton peak energy coincides with the principle γ-emission of the ^{123}Te radioisotope (159keV). Multiple inelastic scattering within the ^{123}Te source results in a broadening of the 159keV emission and to minimise this source broadening it is necessary to employ a small (~1mm^2), low activity (a few μCi), radioisotope source.

Traditionally the detector response function was measured by placing a small, uncollimated source close to the detector window (Rollason, 1984). However, according to Cardwell, (1987) the response function tail is very sensitive to the area of the detector crystal used, for example, at 60keV the tail increases from 1% of the peak area for pin hole collimation to 40% when the whole detector crystal is viewed. Therefore, the experimental collimation must be exactly reproduced if the correct detector response function is to be measured. Ideally, a point source should be placed at the sample position but in practice the low activity of the source necessitates that the source is positioned close to the detector.

The portion of the detector crystal actually illuminated in the experiment is shown as A in figure 2.12 where the scattered beam passes through a series of 12mm collimators (only 1 is shown). The second figure (B) indicates how approximately the same portion of the
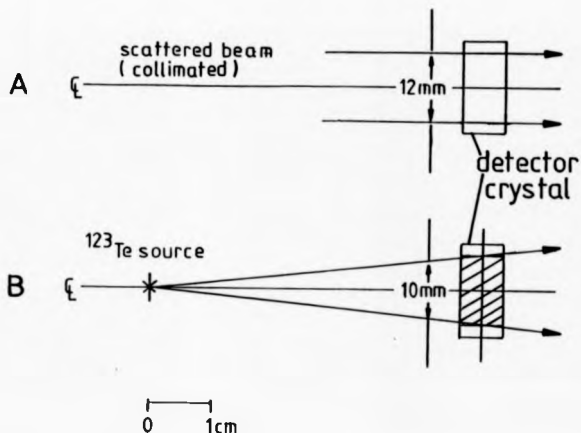
Figure 2.12 Measurement of the high energy spectrometer response function. Diagram A shows the portion of the detector crystal illuminated in the experiment. Diagram B shows how approximately the same conditions can be reproduced if a small ^{123}Te source is placed 45mm from a 10mm collimator which in turn is positioned 5mm from the detector crystal.

detector crystal can be viewed if a point source is placed 45mm from a 10mm collimator, which in turn is 5mm from the detector crystal. Using this experimental arrangement and a 10μCi ^{123}Te powder radioisotope source, the detector response functions were measured with no collimation (RF1), 12mm collimation (RF2) and 10mm collimation (RF3). The powder source was dispersed inside a glass ampoule in an attempt to minimise source broadening and for each measurement, intensity was recorded over a period of 10 days. Figure 2.13a shows the measured response functions, which have been normalised to 10^7 counts in the elastic peak channel, the peak to tail ratios are given in table 2.2.

The sensitivity of the profile symmetry to each of the response functions is indicated in figure 2.13b which shows the asymmetry of a 100 Compton profile of $Fe_{0.7}Ni_{0.3}$ alloy processed with each response function in turn. There has been no correction for multiple scattering applied to this data. The varying degrees of collimation employed enable 100% (RF1), 90% (RF2) and 40% (RF3) of the surface area of the detector crystal to be irradiated. As the irradiation area is increased the probability of photons and electrons escaping from the crystal edges is also increased. The outcome is RF1 and RF2 overestimate the size of the tail of the response function (RF1 more than RF2) and result in an overcorrection of the profile, i.e. a positive asymmetry.

The profile asymmetry of data processed using RF3, after a correction for multiple scattering has been applied is shown as the dashed line in figure 2.13b. The corrected profile is now symmetric to within $\pm 1.0\% J(0)$ at low momentum and within $\pm 0.5\% J(0)$ at intermediate and high momentum, the residual asymmetry results from the inadequacy of the data processing to remove all systematic errors for $M(\omega)$. However, this still represents a significant improvement over recent measurements of iron (Rollason, Holt and Cooper, 1983) and aluminium (Cardwell and Cooper, 1988) where profile symmetries in the range 1-2% $J(0)$ were obtained.

In view of the high degree of profile symmetry now available with the high energy spectrometer it is possible to form a theoretical comparison of data based on both sides of the measured Compton profile. In addition, it is possible to improve the statistical accuracy of the results without introducing significant systematic errors, by forming left-right average of

41
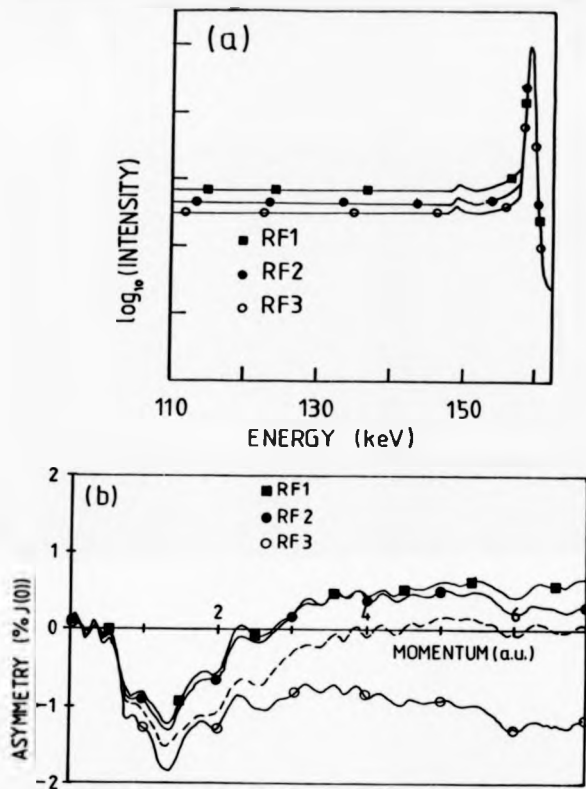
Figure 2.13 (a) The high energy response function measured with no collimation (RF1), 12mm collimation (RF2) and 10mm collimation (RF3) positioned as shown in figure 2.12 and (b) the residual asymmetry in the 100 profile of $Fe_{0.7}Ni_{0.3}$ processed with each of the above response functions. The dashed line is the RF3 asymmetry after the application of a multiple scattering correction.

Detector response function	Collimation/mm	Peak $\times 10^6$ counts	Peak:tail ratio
RF1	none	6.10	141:1
RF2	12	0.24	224:1
RF3	10	1.10	301:1

Table 2.2 Peak:tail ratios of the response functions RF1, RF2 and RF3 shown in figure 2.12.

the measured Compton profiles. The latter tactic is chosen for the results presented in this thesis.

Chapter 3

MEASUREMENTS ON IRON-NICKEL ALLOY, GALLIUM ARSENIDE AND LEAD.

3.1 Introduction.

The previous chapter demonstrated how valuable information about the electronic structure of solids can be obtained from Compton profile measurements. This chapter is concerned with γ-ray Compton profile measurements on single crystals of an iron-nickel alloy, gallium arsenide and lead performed using the high and low energy spectrometer systems outlined in section 2.4. In each case a review of related work is presented followed by a brief description of the experimental details and finally the results are interpreted using appropriate theoretical models of the electron density distributions.

3.2 Iron Nickel Alloy.

3.2.1 Introduction.

The objectives of this study are to obtain accurate directional Compton profiles of the disordered alloy $Fe_{0.7}Ni_{0.3}$ in order to investigate the viability of two recent calculations of its electron momentum density.

Fe-rich FeNi alloys are known to exhibit many intriguing physical properties. For example, neutron scattering measurements of the average magnetic moment show a drastic reduction in the moment from $\sim 1.9\mu_B$ to almost zero within the small concentration range, 65–75% atomic

Fe, while for lower Fe concentrations the moment follows a linear behaviour (see Crangle and Hallam, 1963 and Dupré, Menzinger and Saccetti, 1981). Fe-rich alloys are often termed Invar alloys because they exhibit an anomalously small thermal expansion coefficient at room temperature. This behaviour has been interpreted in terms of a large volume magnetostriction (see Ono, 1979).

The structure of $Fe_{0.7}Ni_{0.3}$ is fcc, although the alloy becomes bcc for iron concentrations of less than 65 at.%. The lattice parameter of the alloy used in this study was determined using the Laué technique as 3.561 ± 0.005Å. $Fe_{0.7}Ni_{0.3}$ exists in a ferromagnetic state and has an average bulk magnetic moment of $\sim 1.7\mu_B$ (see Johnson, Pinski and Staunton, 1987) however, the Compton profiles obtained with unpolarised γ-radiation in the present study will be independent of magnetic effects.

The application of Compton scattering to the study of transition metal alloys is a natural extension of the extensive work already undertaken on the parent elements and is likely to be of particular importance in the field of disordered and concentrated alloys due to the inapplicability of such standard Fermi surface probes as the De Haas Van Alphen method. Furthermore, other electron density probes such as x-ray diffraction and positron annihilation, may also be unapplicable to the study of certain alloys because unlike Compton scattering, they require a degree of crystalline perfection which may be difficult or impossible to achieve in the alloys. Also, the positively charged positron is excluded from the positively charged ion cores of the solid and therefore does not sample the whole electron density. This problem was highlighted in the recent Compton profile study of Ni_3Ga (Itoh, Cooper, Holt, Laundy, Cardwell and Kawamiya, 1984) from which the Compton and positron directional difference profiles reproduced in figure 3.1 have been taken. The Compton profile anisotropies (a) show high momentum oscillations which originate from the d-like electrons which exist partially within the ion cores. In the analogous positron annihilation result (b) the anisotropy is restricted to low momentum as the positively charged positron is unable to sample the high momentum components of the d-electrons within the ion cores.

There are only a few Compton profile measurements of transition metal alloys and the majority of these studies have been concerned with ordered intermetallic compounds. Chad-
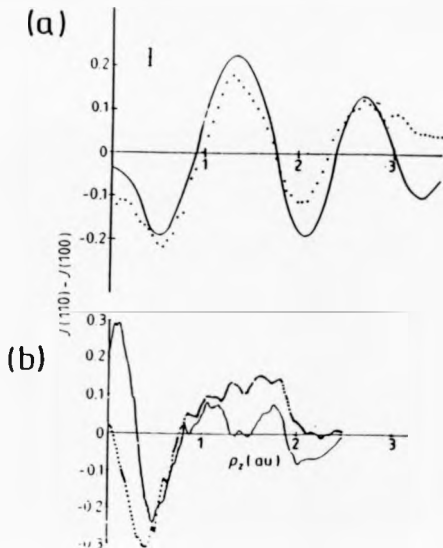
44

Figure 3.1 Directional difference profiles for Ni_3Ga (from Itoh et al, 1984), (a) shows the experimental Compton profile result (filled circles) and the prediction of an APW calculation by Wakob and Kubo (1983) (solid line) and (b) shows the analogous positron annihilation result. Note the resolution is almost an order of magnitude better than the Compton experiment.

dah and Sahni (1978) and Manninen, Sharma, Paakkari, Rundquist and Richardson (1981) have performed Compton profile measurements on a range of transition metal-aluminium intermetallic compounds in order to investigate the d-band occupancy and suspected transfer in these materials. Manninen et al showed that the charge transfer to the transition metal was largest for CoAl and decreased with higher or lower atomic numbers. This trend was in agreement with that obtained from X-ray emission experiments and melting point measurements of these compounds. Podloucky and Neckel (1979) have used the Atomic Plane Wave (APW) method to calculate the directional Compton profiles of FeAl and note a marked anisotropy even at high momentum.

Isotropic Compton profiles of FeTi have been measured by Lasser, Lengeler and Arnold (1980) and Bauer, Schneider and Welter (1984) using 320keV and 412keV photons respectively. In both cases the data were analysed in terms of a renormalised free atom model and the best agreement between experiment and theory was obtained for a configuration $Fe(3d^6 4s^2) Ti(3d^3 4s^2)$. X-ray emission spectroscopy measurements of TiNi were explained by Kallne (1974) in terms of a reorganisation in Ti from $3d^3 4s^1$ to $3d^2 4s^2$ and in Ni, from $3d^8 4s^1$ to $3d^8 4s^2$. The Compton profiles of TiNi were measured by Paakkari and Manninen, (1974) and found to be in good agreement with the superposition of the Compton profiles of Ti $(3d^3 4s^1)$and Ni $(3d^8 4s^1)$. This indicated that metallic bonding in the alloy is similar to the bonding in the pure metals which contradicts a reorganisation hypothesis.

The first comprehensive Compton profile study of a disordered alloy system was performed by Benedek, Prasad, Manninen, Sharma, Bansil and Mijnarends (1985) for a series of 5 polycrystalline $Cu_x Ni_{1-x}$ alloys. Isotropic Compton profiles calculated using the Korringa-Kohn-Rostocker coherent potential approximation (KKR-CPA, see section 3.2.2) were found to reproduce the main features of the observed Compton profiles. No experimental studies of directional or isotropic Compton profiles of an FeNi alloy exist in the literature although a study of the momentum density of the disordered alloy $Fe_{0.3} Ni_{0.7}$ is presently underway at the University of Warwick (Brahmia, private communication).

3.2.2 Theoretical Models for $Fe_{0.7}Ni_{0.3}$
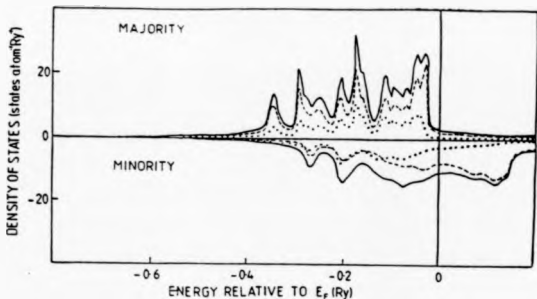
The density of states (DOS) of $Fe_{0.7}Ni_{0.3}$ calculated using the KKR-CPA method by Staunton (private communication) is shown in figure 3.2a where the dashed, dotted and solid lines represent the Fe and Ni and the alloy DOS respectively. From this figure it is apparent that the DOS of the Fe and Ni majority spin electrons are similar in shape and are scaled according to the respective concentrations of the constituent Fe and Ni atoms (i.e. 0.7:0.3). However, the DOS of the minority electrons are very different with a large concentration of Ni states below E_f and a large concentration of Fe states above E_f. This observation suggests that the lattice site potentials for the majority spin electrons of Fe and Ni are similar, i.e. $V_{Fe,maj}(r) \sim V_{Ni,maj}(r)$, whereas the minority spin lattice potential is strongly species dependent, i.e. $V_{Fe,min}(r) \neq V_{Ni,min}(r)$. A consequence of this is that, in general, the majority electrons will be free to hop to any neighbour, whereas the minority electrons will be confined to one species.

Wakoh (private communication) employed the rigid band approximation and used the APW method (RB-APW) to calculate the electron momentum distribution of $Fe_{0.7}Ni_{0.3}$. The rigid band approximation assumes a constant DOS which is filled to a Fermi level determined solely by the number of valence electrons. This calculation was based on the fcc Ni lattice (Fe is bcc) which was adjusted to have the same lattice parameter as the alloy (3.561Å). Assuming $V_{Fe,maj}(r) \sim V_{Ni,maj}(r)$, the majority spin band can be adequately described by a rigid band model. However, as $V_{Fe,min}(r) \neq V_{Ni,min}(r)$, Wakoh chose to formulate the alloy minority spin band from two independent rigid bands for Fe and Ni respectively filled to a common Fermi surface (see figure 3.2b).

In density functional band calculations like the KKR-CPA and APW calculations, the exchange correlation is written in terms of the electron charge density, $\rho(r)$. It has been shown (Hohenberg and Kohn, 1964 and Kohn and Sham, 1965) that solution of the resulting equation yields the correct ground state energy and charge density of the many bodied system however, the pseudo-wavefunctions obtained are not one electron functions and cannot be simply fourier transformed to yield momentum eigenfunctions. Bauer (1984) has shown how a correlation correction can be determined within the local density approximation but this correction has yet to be incorporated into density functional band calculations. As mentioned earlier, the consequence of neglecting electron correlation is an over estimation of the scale of Compton profile anisotropy.

The APW method does not account for the alloy disorder whereas the KKR-APW method accounts for the random assignment of atoms to sites by defining an 'effective' lattice which reproduces the electronic properties of the actual alloy. However, the APW method is the more established technique used for calculating $J(p_z)$. In order to include all the electron density, it was necessary to add a Hartree Fock composite free atom core to the RB-APW theoretical Compton profiles.

(a)

(b)
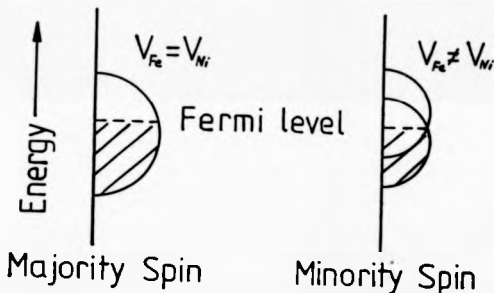
Figure 2.2 (a) The calculated majority and minority density of states (DOS) of ferromagnetic $Fe_{0.7}Ni_{0.3}$. For each spin the solid line gives the total DOS. The dashed and dotted lines represent the contributions from iron and nickel sites respectively. (b) A schematic representation of the bands in $Fe_{0.7}Ni_{0.3}$ used by the RB-APW model. The majority band is described by one rigid band whereas the minority band is composed from the superposition of two rigid bands filled to a common Fermi level.

3.2.3 Experimental Details.

This experimental study was performed on three single crystals of $Fe_{0.7}Ni_{0.3}$ alloy obtained from Metals Research, Cambridge. The composition of the samples were determined as $71.4\pm0.4\%Fe$ $28.6\pm0.4\%Ni$ using an electron microscope to analyse the Fe and Ni X-ray fluorescence yields. After weighing the crystals in air and then mercury, the density was determined as $8.15\pm0.05gcm^{-3}$. All three disc shaped samples were $2.15\pm0.02mm$ thick, area $\sim130mm^2$ and were mounted onto the perspex sample holder by thin strands of adhesive tape. For the high energy spectrometer, individual spectra were accumulated over a period of 3 to 6 days, depending on the initial source activity, to record $\sim 2.1 \times 10^8$ counts in the Compton peak channel (0.05keV, 0.03a.u.). For the low energy spectrometer where the emitted flux is essentially constant, measurement times of ~11 days resulted in $\sim 1.8 \times 10^5$ counts in the Compton peak channel (0.02keV, 0.03a.u.).

This investigation was undertaken over a period of 6 months during which time five gold sources were used. The energy spectrum for one orientation plus a background spectrum were accumulated with each new gold source, the 110 and 111 orientations were measured twice to ensure reproducibility of the results. The measured background contribution at the Compton peak of the high energy data was small ($\sim0.5\%$) and therefore a static background correction was deemed unnecessary. The corresponding background for the low energy spectrometer was $\sim0.2\%$ of the Compton peak. No electronic drift was observed during any of the measurements, i.e. observed fluorescence lines were not wider than the detector response function.

The processing procedures outlined in chapter 2 were applied to the data and the corrected profiles were extracted on a momentum grid of 0.05a.u. . The spectral distribution of multiply scattered photons was determined by a Monte Carlo simulation and contained 8.2×10^4 and 1.3×10^3 photons from an input of 30 million and 15 million photons for the high and low energy spectrometers respectively. The corresponding values of α were 1.205 and 1.119 respectively over the momentum range -7a.u. to 7a.u.. After application of the multiple scattering correction the high energy data were normalised to the composite free atom value

47

of 11.710 in the momentum range 0–7a.u. and were found to be in agreement to within $\pm 0.2\% J(0)$ of the freeatom value in the high momentum limit (see figure 3.3). However, the low energy profiles exhibited considerable asymmetry over the entire momentum range (typically $2\% J(0)$ at 2a.u.). This may be attributed in part to a breakdown in the IA assumed in the data processing (see chapter 2) which complicates the normalisation of these profiles. The K-shell binding energies of Fe and Ni are 7.11keV and 8.33keV respectively and Compton profiles measured with 60keV γ-radiation exhibit 'binding edges' at 6.37a.u. (Fe) and 4.45a.u. (Ni). At momentum values greater than the binding edge the 1s electrons of Fe and Ni fail to contribute to the profile and the high momentum tail lies below the free atom value. In view of these and other limitations imposed by the data processing (see chapter 2), the low energy data is only presented in the form of directional differences.

3.2.4   Results and Discussion.

Difference Profiles.

The profile anisotropies predicted by the KKR-CPA (solid line) and RB-APW (dashed line) calculations are shown in figure 3.4 after convolution with a Gaussian of FWHM=0.4a.u. which mimics the resolution of the high energy spectrometer. The directional difference profiles derived from measurements on both spectrometer systems are shown in figure 3.5 from which it is apparent that both data sets are in mutual agreement within the statistical error ($\sim \pm 0.2\% J(0)$).

A comparison of figures 3.4 and 3.5 reveals that the KKR-CPA theory of Staunton fails to predict the frequency of the oscillations and overestimates the scale of the anisotropy by more than a factor of 3. The RB-APW calculation of Wakoh is somewhat more successful at predicting the frequency although the magnitude of the anisotropy is still overestimated by almost a factor of 2. This calculation has been convoluted with a Gaussian of the appropriate width and is included along side the experimental results in figure 3.5. The overestimation of the profile anisotropy is a feature of band calculations of transition metals and it has been attributed to the exclusion of electron correlation effects from the calculation. This overestimation is illustrated by figure 3.6 which shows the measured 100-110 anisotropy in

48
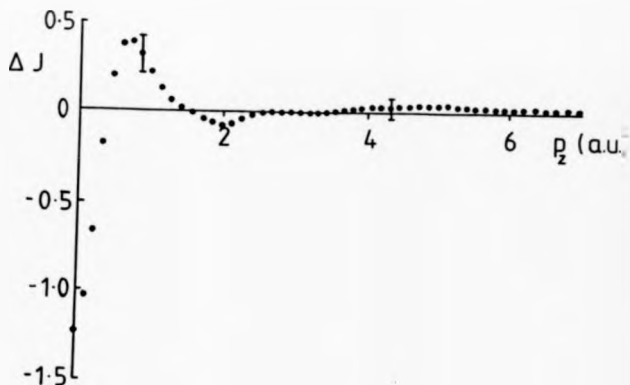
Figure 3.3 Experiment - free atom for the 100 Compton profile of $Fe_{0.7}Ni_{0.3}$ measured on the high energy spectrometer. The form of this curve is characteristic of the other directional profiles. The experiment approaches the free atom value at high momentum.
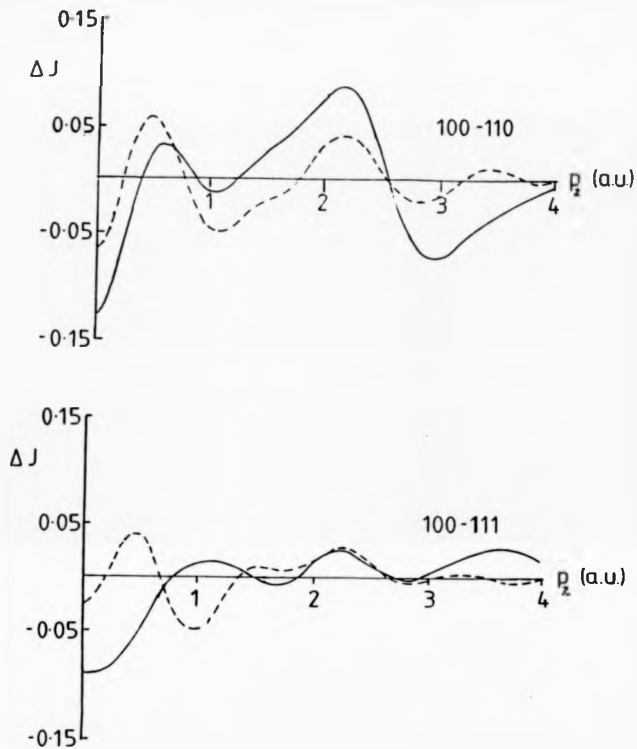
Figure 3.4 Theoretical profile anisotropies for the KKR-CPA (solid line) and RB-APW (dashed line) respectively. Both theories have been convoluted with a Gaussian of FWHM=0.4a.u.
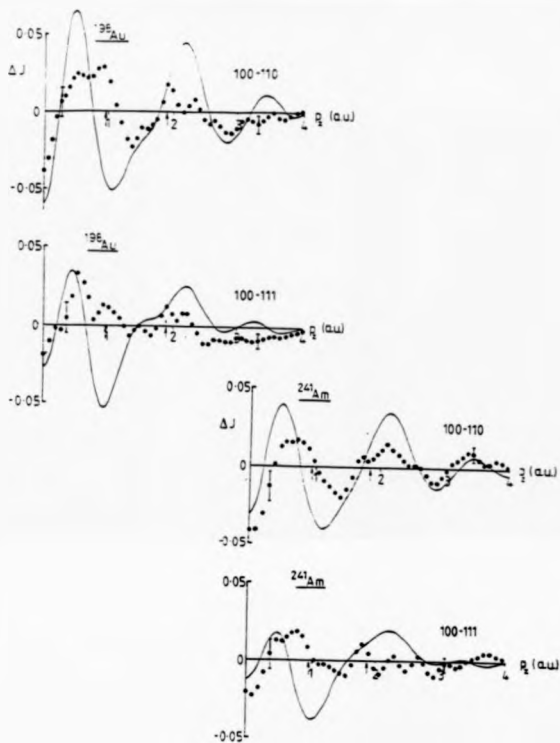
Figure 3.8 The experimental directional difference profiles of $Fe_{0.7}Ni_{0.3}$ derived from Compton profile measurements on the high and low spectrometer systems. The solid line is the RB-APW prediction of the anisotropy. The theory has been convoluted with a Gaussian of FWHM=0.4a.u. and 0.57a.u. for comparison with the ^{198}Au and ^{241}Am profiles respectively. The arrow denotes the positions of the 100 planes in the $Fe_{0.7}Ni_{0.3}$ reciprocal lattice i.e. $p_z = 0.93a.u.$ and $1.86a.u.$.
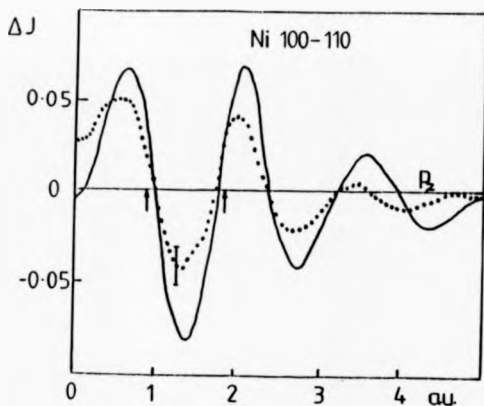
Figure 3.6 Comparison of the experimental (filled circles) and theoretical (solid line) 100-110 anisotropy in nickel. The experimental result was obtained from Compton scattering measurements with 412keV γ-radiation (Rollason et al, 1986). The linear combination of Gaussian orbitals (LCGO) calculation of Wang and Callaway (1975) has been convoluted with a Gaussian of FWHM=0.4a.u. to match the experimental resolution. The positions of 100 planes in the Ni reciprocal lattice (p_z=0.94a.u.) are indicated by the arrows.

Ni (Rollason, Schneider, Laundy, Holt and Cooper, 1987) and the theoretical anisotropy calculated using a linear combination of Gaussian orbitals (LCGO) (Wang and Callaway, 1975).

The experimental profiles show only small anisotropy with differences amounting to only $\sim \pm\frac{1}{2}\%J(0)$, in contrast to the parent elements for which differences upto $2\%J(0)$ have been observed for Fe (Rollason, Holt and Cooper, 1983) and upto $1\%J(0)$ for Ni (see figure 3.6). This implies the alloy Fermi surface has a higher degree of sphericity than the parent elements. The arrows in figure 3.5 indicate the position of 100 planes in the alloy reciprocal lattice. At these values of p_z i.e. 0.93a.u., 1.86a.u. etc., the 100 directional profile exhibits a relative maximum as confirmed by the 100-110 difference profiles. Similar maxima occur in the 110 profile at p_z values of 1.32a.u., 2.64a.u. etc. and in the 111 profile at p_z values of 0.81a.u., 1.62a.u. etc. although as for Ni (see Rollason et al, 1987), the anisotropies show no clear evidence of the 111 maximum. It is interesting to note that Rollason et al only observed evidence of the second maxima in the 100 profile of Ni (see figure 3.6), whereas the first and second maxima are observed in the alloy 100 profile. No such maximum is predicted by either the APW calculation of Ni or the RB-APW calculation of the alloy, however at the present time it is not understood were the origin of this difference lies.

The ^{196}Au, RB-APW directional Compton profiles and the Hartree Fock composite free atom profiles are listed in table 3.1. All theoretical profiles have been convoluted with a Gaussian of FWHM=0.4a.u..

The Absolute Profiles.

Figure 3.7 shows the difference $\Delta J(p_z) = J^{Theory}(p_z) - J^{expt}(p_z)$ for the 100 directional profile measured on the high energy spectrometer and the KKR-CPA calculation of $J(p_z)$. The form of this curve is characteristic of all three directional measurements. It is evident from figure 3.7 that the KKR-CPA model underestimates the magnitude of the profile at low momentum ($p_z < 1$a.u.) by almost $20\%J(0)$ and overestimates the profile at intermediate momentum values ($1 < p_z < 3.5$a.u.). Furthermore, the profile significantly deviates from the free atom limit at high momentum ($p_z > 4$a.u.). These gross discrepancies prompted

Table 3.1 Experimental and theoretical Compton profiles of $Fe_{0.7}Ni_{0.3}$ measured with the high energy spectrometer, along 100, 110 and 111. The rigid band theory of Wakoh (private communication) has been convoluted with a Gaussian of FWHM 0.4 a.u. to mimic the experimental resolution half width.

p_z	100		110		111		Free atom
	Exp.	RB-APW	Exp.	RB-APW	Exp.	RB-APW	
0.0	5.127 ± 0.013	5.227	5.181	5.283	5.143	5.257	6.429
0.1	5.125	5.216	5.163	5.258	5.131	5.293	6.286
0.2	5.084	5.180	5.097	5.186	5.082	5.186	5.905
0.3	4.998	5.111	5.008	5.075	4.998	5.095	5.400
0.4	4.887	4.998	4.869	4.934	4.871	4.967	4.893
0.5	4.738	4.838	4.707	4.768	4.705	4.807	4.467
0.6	4.553	4.639	4.524	4.585	4.518	4.624	4.149
0.7	4.351	4.418	4.315	4.392	4.334	4.429	3.925
0.8	4.146	4.193	4.124	4.199	4.142	4.230	3.763
0.9	3.949	3.981	3.933	4.011	3.925	4.032	3.633
1.0	3.749	3.785	3.742	3.829	3.733	3.838	3.514
1.2	3.373	3.434	3.377	3.474	3.366	3.464	3.271
1.4	3.010	3.103	3.026	3.124	3.011	3.109	3.003
1.6	2.688	2.774	2.702	2.787	2.691	2.772	2.721
1.8	2.396	2.471	2.384	2.464	2.388	2.465	2.443
2.0	2.131	2.207	2.094	2.171	2.124	2.190	2.177
2.5	1.587	1.652	1.601	1.645	1.599	1.645	1.618
3.0	1.219	1.237	1.228	1.249	1.224	1.238	1.221
4.0	0.798 ± 0.004	0.795	0.799	0.801	0.798	0.795	0.773
5.0	0.587	0.521	0.590	0.527	0.591	0.528	0.551
6.0	0.457		0.456		0.456		0.417
7.0	0.352		0.346		0.351		0.204

Figure 3.7 The difference between the KKR-CPA theory and the experimental 100 Compton profile measured with the high energy spectrometer. The form of this curve is characteristic of all three directions which have been excluded for clarity. The experimental error is contained within the size of each data point (i.e. $\sim \pm 0.2\% J(0)$) and $\Delta J = 1.0 \sim 20\% J(0)$. The theory has been convoluted with a Gaussian of FWHM=0.4a.u. before comparison with experiment.

Staunton to check the computational method used to obtain $J(p_z)$ which brought to light the following computational error: having obtained $n(\mathbf{p})$, Staunton calculated $J(p_z)$ using equation 1.4. but limited the infinite 2-D integral of $n(\mathbf{p})$ to $|\mathbf{p}| < 10 \text{a.u.}$ As a consequence of restricting the integration, a significant fraction of the high momentum components of $n(\mathbf{p})$ were omitted from $J(p_z)$. This resulted in a deficit of $\sim 16\%$ in the area of $J(p_z)$. The integration still captures all the valence electron contribution to $n(\mathbf{p})$ (i.e. $p_z < 5 \text{a.u.}$) and as the core electron contribution is isotropic, the directional differences shown in figure 3.4 will be relatively unaffected by this error.

Figure 3.8 shows $\Delta J(p_z)$ (theory - experiment) for all three directional profiles measured with 412keV γ-radiation and the corresponding RB-APW profiles. All three curves follow a similar trend and it clear that the RB-APW calculation overestimates the electron density at low momentum ($p_z < 3 \text{a.u.}$) and underestimates the density at high momentum ($p_z > 3 \text{a.u.}$) This discrepancy may be attributed to the neglect of electron correlation effects from the APW calculation. In general, the effect of electron correlation is to transfer electron density from occupied regions below the Fermi surface to the unoccupied regions of reciprocal space above it, i.e. a transfer of density from low to high momentum. A closer examination of figure 3.8 reveals a periodic structure in $\Delta J(p_z)$ coinciding with the arrows marked on the p_z axis. As in figure 3.5, these arrows denote the positions of reciprocal lattice vectors along the appropriate crystallographic directions. The difference between experiment and theory in many single element metals e.g. Cr, Al, Ni etc. has been partially resolved by calculation of correlation effects within the local approximation by the so-called Lam Platzman correction (see Cardwell, 1987). However, whilst the Lam Platzman correction considerably improves the agreement between experiment and theory, it is isotropic. To explain the periodic fine structure in $\Delta J(p_z)$ (figure 3.8) and the overestimation of the profile anisotropies (figure 3.5) requires an anisotropic correction term similar to the Lam Platzman term but derived from non-local effects. A method of modeling such anisotropic correlation corrections has recently been developed by Wakoh and Matsumoto (1988) and was found to reconcile the differences between experiment and APW Compton profiles of Cr (see Cardwell, Cooper and Wakoh, 1989)
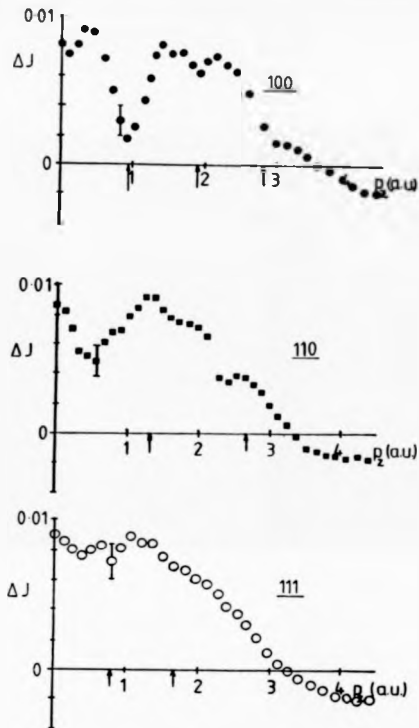
Figure 3.8 The difference between the RB-APW theory and all three directional profiles of $Fe_{0.7}Ni_{0.3}$ measured on the high energy spectrometer. The arrows denote the positions of appropriate planes in the reciprocal lattice. The theory has been convoluted with a Gaussian of FWHM=0.4a.u..

3.3 Gallium Arsenide.

3.3.1 Introduction.

The aim of this study was to investigate the bonding nature in tetrahedrally bonded semi-conductors. The directional Compton profiles of the compound semiconductor GaAs were measured with 412keV and 60keV γ-radiation and the results compared with theoretical calculations based on the pseudo-potential method. The structure of GaAs at room temperature is fcc (zinc blende type structure) with a lattice parameter of 10.64Å.

Many Compton scattering studies of tetrahedrally bonded semiconductors are reported in the literature although the majority have been concerned with the pure covalent semiconductors C, Si and Ge. One of the earliest γ-ray Compton profile studies on these materials was undertaken by Reed and Eisenberger (1972) who measured five directional Compton profiles of diamond, Si and Ge. These results prompted a profusion of theoretical calculations of $J(p_z)$ for these materials to be undertaken by a variety of methods, for example Hartree Fock (Wepfer, Euwema, Surrat and Wilhite, 1974), Linear Combination of Atomic Orbitals (LCAO) (Seth and Ellis, 1977) and pseudopotential (Nara, Shindo and Kobayashi, 1979). Diamond, Si and Ge have common crystal structure but exhibit quite different electronic properties. Therefore it is possible to determine whether the anisotropy in the profile is dependent only on the lattice structure or whether it depends on the physical properties of the elements (for example, see Reed and Eisenberger, 1972).

Pattison and Schneider (1978) used 412keV γ-radiation to measure the Compton profiles of Si and Ge along the 110 direction and analysed the long range autocorrelations of the electronic wavefunctions obtained directly from the B-function (equation 2.6). The B-function of Si was found to be in excellent quantitative agreement with a LCAO calculation (Seth and Ellis, 1977) and the zero passages in the B-functions of Si and Ge clearly illustrated the expansion of the valence electron wavefunctions resulting resulting from the different lattice constants (refer to figure 2.5).

Pattison, Hansen and Schneider (1981) reconstructed the 3 dimensional electron momentum density n(p) from theoretical directional Compton profiles of diamond and Si. The
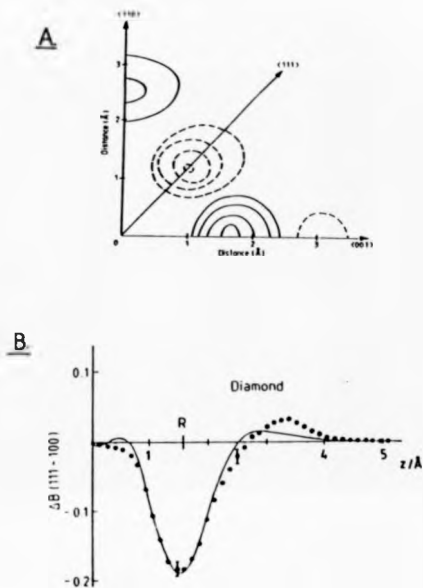
Figure 3.9 (a) The anisotropy in $B(r)$ for diamond derived from Compton profile calculations by Seth and Ellis (1977). The contours are given in intervals of 0.05 electrons. The strong negative depression along 111 is at a separation of 1.54Å, i.e. the nearest neighbour distance. (b) The solid line is the difference between $B(r)$ along 111 and 100 in diamond derived from the Compton profile anisotropy calculated by Seth and Ellis (1977). The experimental result was obtained by Fourier transforming the experimental profile anisotropy measured by Reed and Eisenberger (1972). The theory has been multiplied by an appropriate resolution damping function and the bond distance along 111 is marked R, (from Pattison et al, 1981).
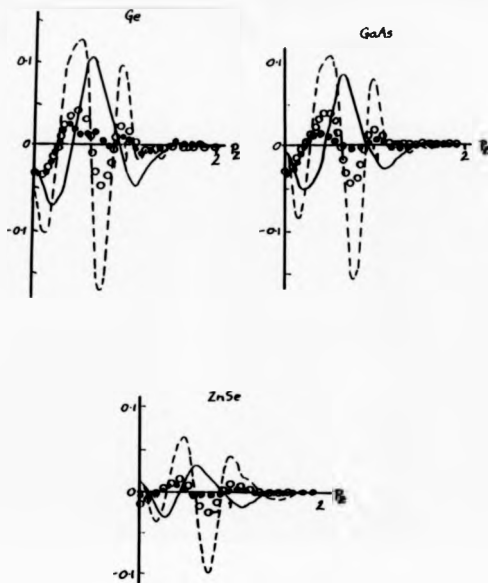
Figure 3.10 The Compton profile anisotropies for Ge, GaAs and ZnSe calculated by Nara et al (private communication) using the pseudopotential method. $J_{111} - J_{100}$ (—), $J_{111} - J_{110}$ (- - -), $J_{111} - J_{112}$ (●●●) and $J_{111} - J_{221}$ (OOO).

strongest feature of the $B(r)$ reconstruction was the negative region at the bond length along the 111 crystallographic direction (see figure 3.9a, taken from Pattison et al 1981). The strong minimum in $B(r)$ at $r = \mathbf{R}_L$ is the consequence of an overlap between a $2p\sigma$ orbital on one atom and an identical, antiparallel orbital on the next atom along the chain. This bond anisotropy can also be observed experimentally as illustrated by figure 3.9b (from Pattison et al 1981).

The electron momentum density of Si has recently been reconstructed from six directional profiles measured with 412 keV $\gamma$-radiation (Hansen, Pattison and Schneider, 1984) and the results were found to be in good agreement with momentum density reconstructed from the directional Compton profiles of Seth and Ellis (1977).

Only recently has attention deviated from pure semiconductors to compound semiconductors such as GaAs, ZnSe etc. Recent pseudopotential calculations for the compound semiconductors GaAs, InSb, CdTe and ZnSe (Nara, Kobayashi and Shindo, private communication) indicate a decrease in anisotropy according to the serial order of the IV, III-V and II-VI semiconductors which is consistent with the increasing ionicity of the bonding character. This is illustrated by figure 3.10, where the Compton profile anisotropies from Ge, GaAs and ZnSe, calculated using the pseudopotential method (Nara et al) are reproduced.

The pseudopotential calculation was performed using an inversion technique based on a Fourier transform method. The momentum density was written in terms of the pseudovalence wave functions (equation 3 in Nara, Shindo and Kobayashi, 1979) which was then Fourier inverted to obtain $B(r)$ (equation 2.3). Once $B(r)$ had been calculated for various directions of r, the corresponding Compton profiles were obtained for an arbitrary fine mesh of p_z by Fourier transforming $B(z)$.

Nageswar, Mohapatra, Panda and Padhi (1985) measured the directional Compton profiles of the compound semiconductor GaP but were unable to draw any quantitative conclusions from their data due to the unavailability of a suitable theoretical model. This study will therefore represent the first comprehensive directional Compton profile study of a tetrahedrally bonded compound semiconductor.

82

3.3.2 Experimental Details.

Five directional Compton profiles (100, 110, 111, 112 and 221) of GaAs were deduced from measurements on the high energy spectrometer and three (100, 110 and 111) from measurements on the low energy spectrometer. The single crystal samples used for this study were cut and shaped into discs, diameter 15.10 ± 0.05mm and average thickness 1.82 ± 0.02mm.

The individual energy spectra were accumulated over a period of 2–5 days (high energy spectrometer) depending upon the source activity and 15 days for measurements on the low energy spectrometer. This enabled a total of 6.4×10^6 (7.5×10^5 for the 112 and 221 profiles) and 1×10^6 counts to be recorded in the respective Compton peak channels (0.03a.u.). Three gold sources were used during this study and two orientations plus a background were measured with each source. The 110 direction was measured twice to check the reproducibility of the results which was found to be well within the statistical error of $\pm0.2\%J(0)$ (see figure 3.11). The static background contribution to the total background was estimated to be $\sim 40\%$ at the Compton peak channel and was removed using the correction procedure outlined in chapter 2.

A Monte Carlo simulation was employed to determine the multiple scattering contribution present in the high energy data. An input of 17.7×10^6 photons resulted in approximately 2.6×10^3 counts under $J^{multiple}(p_z)$ over the momentum range -7a.u. to 7a.u. and an α value of 1.148. As for $Fe_{0.7}Ni_{0.3}$ a cubic spline fit to $J^{multiple}(p_z)$ was used to correct $J(p_z)$. The low energy data was not corrected for multiple scattering and therefore this data is only presented in the form of directional difference profiles.

After data processing the high energy data were normalised to the free atom value of 25.318 over the momentum range $0 < p_z < 7$a.u. and as for $Fe_{0.7}Ni_{0.3}$, the resulting profiles were all found to reduce to the free atom value at high momentum (see figure 3.12). Similarly the low energy data were normalised to a free atom value of 24.861. This value accounts for the binding edges of Ga (49.17keV, 1.275a.u.) and As (47.97keV, -0.59a.u.). As for $Fe_{0.7}Ni_{0.3}$ these profiles were found to exhibit poor profile symmetry which has been attributed to residual systematic errors in the processed data.
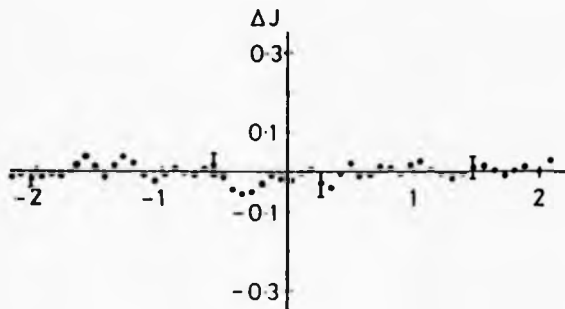
Figure 3.11 Reproducibility of data. The difference between two measurements of the 110 Compton profile of GaAs made with the high energy spectrometer.
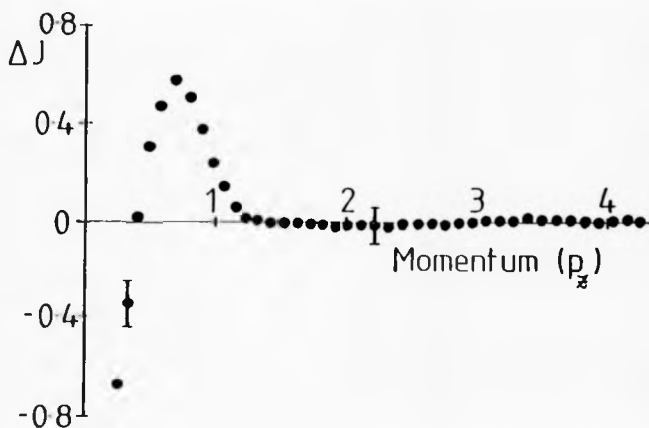
Figure 3.12 Experiment - free atom for the 100 Compton profile of GaAs measured on the high energy spectrometer system. As for $Fe_{0.7}Ni_{0.3}$, the experiment approaches the free atom value for high momentum.

3.3.3 Results and Discussion.

Difference Profiles.

The experimental difference profiles derived from measurements with 60keV and 412keV γ-radiation are shown in figure 3.13. The pseudopotential profile anisotropies have been convoluted with Gaussians of the appropriate widths and included as the solid lines in figure 3.13. The experimental profiles are identical beyond $|p_z| = 2$ a.u. and have been normalised to the free atom area out to this momentum. Examination of the two independent data sets obtained from the high and low energy spectrometer systems reveal excellent mutual agreement. The low energy anisotropies are of slightly poorer quality (typically $\pm0.27\%J(0)$) than the high energy anisotropies ($\pm0.23\%J(0)$) and the additional resolution broadening of the low energy spectrometer (0.57a.u. compared to 0.4a.u.) is evident as a damping on the scale of the anisotropies.

The pseudopotential theory is in excellent agreement with all the experimental anisotropies, correctly predicting both the scale and the oscillation frequency of the anisotropies. This is in contrast to a recent pseudopotential calculation for the Compton profiles of Si and Ge (Nara, Shindo and Kobayashi, 1979), where the scale of the anisotropy was correctly predicted but the oscillation frequency was somewhat shorter than that observed experimentally (Reed and Eisenberger, 1972).

The arrows in figure 3.13 indicate the positions of the 111 reciprocal lattice vector. The theory predicts a build up of momentum density at these values of p_z i.e. 0.511a.u., 1.022a.u. etc., this is also observed experimentally. The experimental 111-100 Compton profile anisotropy of Ge obtained by Reed and Eisenberger (1972) is included as the filled squares in figure 3.13. A comparison of the 111-100 anisotropies of Ge and GaAs illustrates that, as predicted by Nara et al (see figure 3.10), the scale of the anisotropy decreases from Ge–GaAs. This trend was observed for all the experimental directional difference profiles and as mentioned earlier, this decrease has been attributed to an increase in ionic bond character.
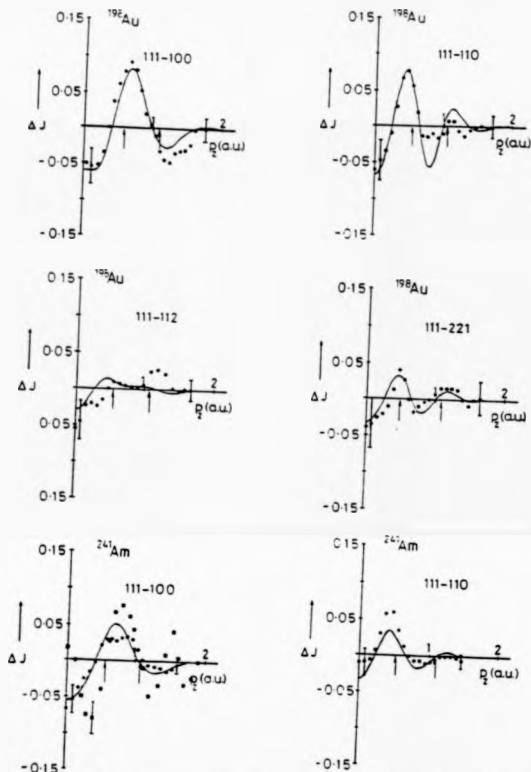
Figure 3.13 The experimental directional difference profiles of GaAs derived from Compton profile measurements on both spectrometer systems. The solid line shows the corresponding pseudopotential difference profiles which have been convoluted with a Gaussian of the appropriate width. The filled squares in the low energy 111-100 anisotropy represent the 111-100 anisotropy of Ge obtained in a Compton scattering study by Reed and Eisenberger, 1972).

The Individual Profiles.

The absolute directional profiles of GaAs deduced from measurements with 412keV γ-radiation are listed in table 3.2. Also included are the pseudopotential directional profiles and a composite free atom profile of GaAs. To include the total electron momentum density a Hartree Fock free atom core has been added to the pseudopotential profiles and all theories are convoluted with a Gaussian of FWHM=0.4a.u..

Figure 3.14 shows the difference between the pseudopotential calculation and the 111 directional profile of GaAs measured with 412keV γ-radiation. The form of this curve is characteristic of the other directional profiles which have been excluded from this figure for clarity. The calculated curve is some 5% larger than the experimental values at low momentum and is smaller at high momentum. According to Nara (private communication) this is understandable because the calculation neglects the core-orthogonalisation terms which are responsible for the high momentum tail of the Compton profile.

In the true solid the electron wavefunctions are simple and smoothly varying in the regions between the ion cores, but in the region of the ion cores, the valence wavefunctions are complicated by the strong, rapidly varying ion core potential. In the pseudo-solid the crystal potential energy in the core region, $V_{crystal}$ is replaced by an effective potential, the pseudopotential, V_{pseudo} which gives rise to the same electron wavefunctions outside the core as does the actual potential. Furthermore, in the core region the pseudopotential is almost zero thereby enabling the core states to be eliminated from the calculation. Unfortunately, the pseudopotential method does not account for the large, local deviations in the valence wavefunctions which occur near the ion cores. These deviations give rise to the high momentum components of the wavefunction which in turn are responsible for the long tail of the Compton profile. This tail reduces the value of the Compton profile for small values of momentum.

Nara et. al. (1979) have shown that although the effect of the core-orthogonalisation terms on the absolute Compton profile is large, it is generally isotropic. Therefore, any discrepancies in the absolute profiles will be removed upon formation of the directional difference profiles.

Table 3.2

p_z	100		110		111		112		221		Free atom
	Exp	Pseudo	Exp	Pseudo	Exp	Pseudo	Exp	Pseudo	Exp	Pseudo	
0.0	12.056 ± 0.020	12.754	12.118	12.754	11.965	12.743	12.153	12.794	12.096	12.814	13.468
0.1	11.987	12.734	12.044	12.734	11.939	12.678	12.070	12.720	12.022	12.722	13.316
0.2	11.867	12.591	11.840	12.591	11.753	12.487	11.866	12.495	11.825	12.489	12.831
0.3	11.498	12.282	11.505	12.282	11.468	12.192	11.556	12.168	11.529	12.174	12.098
0.4	11.052	11.809	11.064	11.809	11.083	11.767	11.189	11.735	11.102	11.699	11.217
0.5	10.498	11.109	10.538	11.109	11.003	11.165	10.641	11.147	10.561	11.075	10.296
0.6	9.832	10.233	9.952	10.295	9.924	10.393	9.994	10.389	9.970	10.383	9.477
0.7	9.132	9.313	9.297	9.237	9.237	9.461	9.305	9.465	9.292	9.543	8.668
0.8	8.481	8.220	8.596	8.551	8.349	8.284	8.614	8.290	8.588	8.353	8.044
0.9	7.882	7.526	7.958	7.691	7.907	7.534	7.973	7.527	7.942	7.530	7.548
1.0	7.376	7.154	7.428	6.971	7.378	7.137	7.420	7.108	7.397	7.089	7.161
1.2	6.674	6.546	6.663	6.507	6.626	6.504	6.650	6.514	6.638	6.503	6.606
1.4	6.208	6.076	6.215	6.087	6.181	6.066	6.236	6.070	6.311	6.071	5.850
1.6	5.833	5.723	5.858	5.713	5.831	5.731	5.832	5.729	5.824	5.731	5.850
1.8	5.477	5.353	5.455	5.388	5.458	5.398	5.507	5.398	5.483	5.396	5.501
2.0	5.108 ± 0.015	3.035	5.141	5.039	5.108	5.034	5.137	5.004	5.097	5.004	5.140
2.5	4.227		4.235		4.215		4.249		4.234		4.248
3.0	3.409		3.419		3.437		3.436		3.426		3.429
4.0	2.348 ± 0.011		2.229		2.234		2.220		2.264		2.277
5.0	1.563		1.537		1.567		1.531		1.533		1.572
6.0	1.174		1.139		1.175		1.124		1.165		1.109
7.0	0.998		0.861		0.903		0.854		0.867		0.535

Table 3.2 Experimental and theoretical Compton profiles of GaAs measured along 100, 110 and 111 with the high energy spectrometer. The pseudopotential theory of Saxena (private communication) has been convoluted with a Gaussian of FWHM 0.4a.u. to mimic the experimental resolution half width.
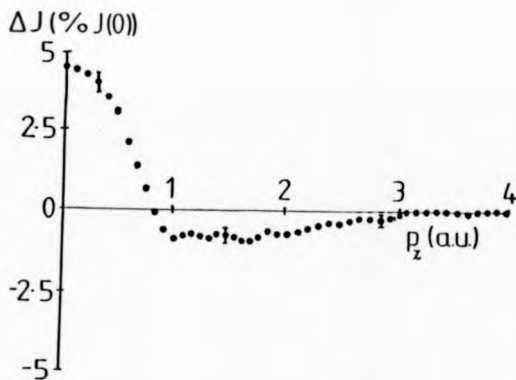
Figure 3.14 The difference between the pseudopotential calculation and the 111 directional profile of GaAs measured with the high energy spectrometer. The theory has been convoluted with a Gaussian of FWHM=0.4a.u. before comparison with experiment.

B-functions.

The reciprocal form factors of the 110 directional profile of GaAs obtained by Fourier transforming the high energy data and the pseudopotential calculation respectively are shown in figure 3.15. The theory has been convoluted to match the experimental resolution of 0.4a.u. which in position space corresponds to a Gaussian damping function with FWHM=7.3Å. At the origin the autocorrelation is complete and $B(0)$ is equivalent to the normalisation of the wavefunctions i.e. $B(0)$=64 for GaAs. According to Pattison and Schneider (1976) the statistical error in $B(z)$ is constant across the whole range of z and is given by $\sigma = \frac{B(0)}{\sqrt{N_{tot}}}$, where N_{tot} is the total number of photons collected under the profile.

The 110 direction was chosen because it exhibits the most prominent oscillations of all the crystallographic directions measured. The theory is in good agreement with the experiment which indicates that the omission of the core-orthogonalisation terms in the former does not influence the B-function over the spatial range shown. Both experiment and theory have a zero passage at the first and possibly the second lattice translation distances (z=3.98Å and 7.96Å respectively) which are indicated by the arrows in figure 3.15.

The largest interatomic separation in GaAs is found along the 100 crystallographic direction. The overlap of the electron wavefunctions will be a minimum for this direction and a maximum for the nearest neighbour direction i.e. the 111 direction. Therefore the difference $\Delta B(111 - 100)$ should reveal the strongest effects of bond anisotropy. From figure 3.16 it is clear that the striking bond anisotropy for GaAs predicted by the theory, can also be observed experimentally. The arrow denotes the nearest neighbour bond distance (i.e. $\frac{\sqrt{3}a}{4}$=2.44Å). The positive feature in the experimental data at ~0.8a.u. is not produced by the theory and was also absent from both the observed and calculated $\Delta B(111 - 100)$ anisotropy of diamond (see figure 3.9b and Pattison, Hansen and Schneider, 1981). This feature is ~ 4 standard deviations in magnitude and was also observed in the low energy data, however at present, its origin is unknown.

It is apparent from this study that the pseudopotential approach is well suited to describing the moment anisotropy and the real space behaviour of the valence electron density of
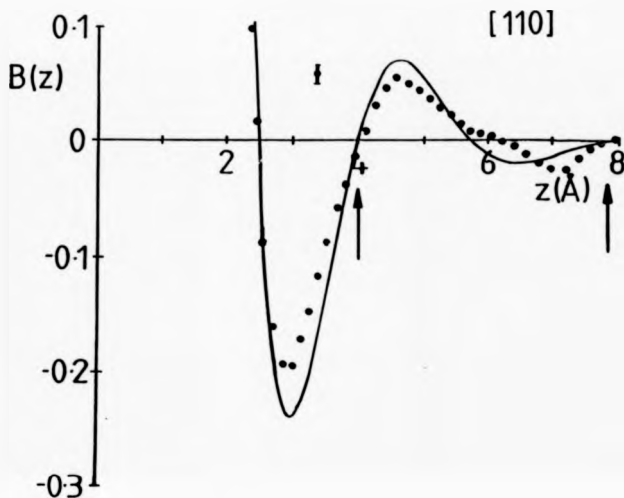
Figure 3.15 The reciprocal form factor, $B(z)$ along the 110 direction in GaAs measured on the high energy spectrometer system. The pseudopotential theory has been multiplied by a Gaussian of FWHM=0.4a.u. before comparison with the experiment. The arrows denote the first and second lattice translation distance i.e. $z=3.98\text{Å}$ and 7.96Å.
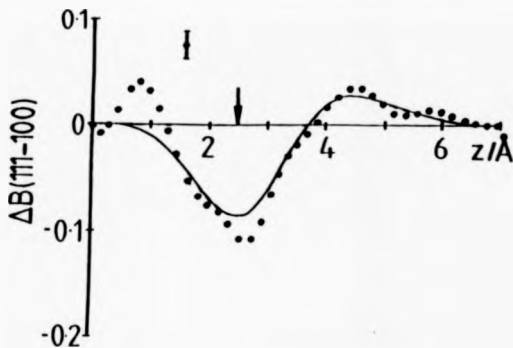
Figure 3.16 The theoretical and experimental difference $\Delta B(111 - 100)$ for GaAs. The theoretical curve has been multiplied by the appropriate Gaussian resolution function. The arrow denotes the bond distance along the 111 nearest neighbour direction i.e. $\frac{\sqrt{3}a}{4} = 2.44$Å.

GaAs. However, the theory is unsuccessful in describing the total electron density distribution.

3.4 Lead.

3.4.1 Introduction.

The main objective of the experiment is to investigate the effect the relativistic core electrons have on the Compton profile of lead.

Relativistic Hartree Fock (RHF) Compton profile calculations of heavy elements by Mendelsohn, Mann and Biggs (1973) and Mendelsohn, Biggs and Mann (1974), have demonstrated that relativistic effects are not limited to electrons situated near to the nucleus. They found that the relativistic spatial wavefunctions of the rapidly moving electrons in the inner orbitals are pulled in towards the nucleus when compared with nonrelativistic Hartree Fock (HF) wavefunctions. This relativistic contraction of the core electron distribution leads to a more effective screening of the nuclear charge and has been attributed to the mass variation of the tightly bound core electrons. The more sharply peaked position space wavefunction of the core electron leads to a flatter momentum space wavefunction and thus a flatter core electron momentum distribution. This is illustrated by figure 3.17 which is taken from Biggs, Mendelsohn and Mann (1975) and shows the RHF and HF electron and momentum densities of the 4s state of lead. The inner 1s, 2s and 2p orbitals of heavy elements are significantly affected by relativistic effects and for the electron wavefunctions to be orthogonal, the outer s and p orbitals must also be affected. Furthermore, due to the normalisation condition, equation 1.5, the relativistic Compton profile must be higher in the tails and hence lower in the peak than the nonrelativistic profile. The importance of relativistic effects in heavy metals is emphasised in a first principles calculation of the crystal structure of lead (Christensen, Sapathy and Pawlowska, 1986) where the omission of relativistic effects lead to the diamond structure of lead being more stable than the observed fcc structure.

A measure of the relativistic flattening is provided by the quantity $J_{RHF}(p_z) - J_{HF}(p_z)$ at $J(0)$. Mendelsohn et al (1974) cite the following results: Ar, 0.187% ($Z = 18$), Kr, 0.712%
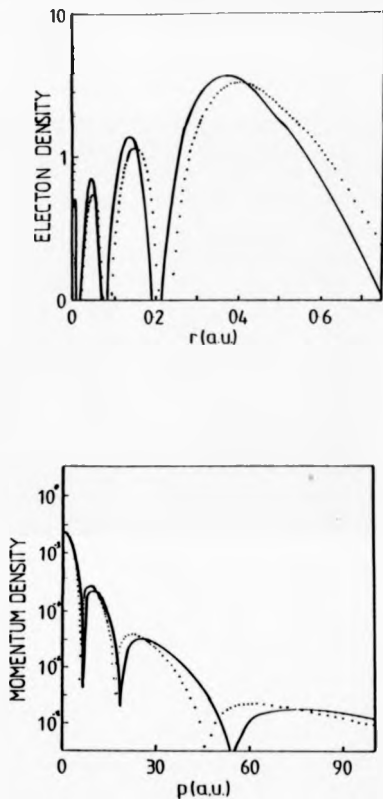
Figure 3.17 Comparison of nonrelativistic Hartree Fock (· ·) and relativistic Hartree Fock(——), (a) electron densities and (b) momentum densities for the 4s state of lead.

$(Z = 36)$ and Pb,5.24% $(Z=82)$.

Eisenberger and Reed (1972) used ^{123m}Te γ-radiation to measure the Compton profile of the rare gases Ar and Kr and compared their results with relativistic and nonrelativistic calculation. However, the relativistic effects in these gases are small and it was not possible to distinguish between the calculations within the statistical accuracy of their results. The effects of relativistic flattening in Pb have been studied by Holt (1979), although the experimental results were of poor statistical accuracy ($\pm4\% J(0)$), low signal to noise ratio and contained a large multiple scattering contribution ($>20\%$ of the total intensity). However, the results did tend to favour a RHF calculation of Pb.

Pattison and Schneider (1979) used 412keV γ-radiation to measure the Compton profiles of Pb and Au up to momentum values of 110a.u.. They limited their interpretation to the momentum range 60–110a.u. where the profile is dominated by the behaviour of the relativistic core electrons. The K- and L-shell binding edges contained within this momentum region were clearly resolved in this experiment and well matched by a RHF calculation of the profile. The good agreement strongly supports the relativistic cross section derived by Ribberfors (1975a and b), (equation 1.22).

3.4.2 Experimental Details.

The 111, 110 and 100 directional Compton profiles of Pb were deduced from Compton scattering measurements on single crystal slices at γ-ray source energies of 412 and 60keV. The individually oriented single crystal discs, diameter 15.0 ± 0.1mm, were cut from a large cylindrical single crystal bar and planed to a common thickness (1.60 ± 0.05mm) using spark erosion techniques. The samples were then etched to remove surface damage using a solution of 20% glacial acetic acid, 30% 100 vol. H_2O_2, 50% methanol, poured over the samples at a rate of 10mls^{-1}.

Individual energy spectra were accumulated over a period of ~260 hours (412keV) and ~400 hours (60keV), enabled $\sim 80 \times 10^3$ and $\sim 40 \times 10^3$ counts to be recorded in the respective Compton peak channels (i.e. 50eV and 20eV, 0.03a.u.). These low count rates (<0.1cps compared for 0.5cps for $Fe_{0.7}Ni_{0.3}$) are a consequence of the high photoelectric absorption

58

cross section of Pb (4.3gcm^{-3} @ 60keV compared to 1.6gcm^{-3} for $Fe_{0.7}Ni_{0.3}$). The total background contribution at the profile centre was $\sim 3.5\%$ and $\sim 14\%$ for the high and low energy spectrometers respectively. The static background contribution was established to be $\sim 65\%$ of the integrated total background of the high energy data and was removed using the procedure outlined in chapter 2.

As usual, a Monte Carlo simulation was employed to determine the energy distribution of the multiple scattering contribution and a cubic spine fit to $J^{multiple}(p_z)$ was used to correct $J(p_z)$. Inputs of 14 million and 5.5 million photons resulted in multiple profiles containing $\sim 8 \times 10^3$ and $\sim 10^3$ photons over the momentum range -13.5a.u.$< p_z <13.5$a.u. and α values of 1.135 and 1.037 respectively. These small values of α (cf 1.205 and 1.119 for $Fe_{0.7}Ni_{0.3}$) are a further consequence of the large photoelectric absorption cross section of lead.

After application of the modified data processing the high energy data were normalised to the free atom value of 29.226 over the momentum range 0-7a.u.. The K, L and M shell binding energies of Pb are 88.01keV, 13.0-15.9keV and 2.5-3.8keV respectively. Hence, it was not possible to excite the 1s electrons in Pb with 60keV radiation and the 2s and 2p electrons did not contribute to the profile for momentum values greater than ~ 7a.u. and $\sim +11$a.u. respectively. These binding edges were accounted for in the normalisation of the low energy data.

3.4.3 Results and Discussion.

The experimental directional Compton profiles measured on the high energy spectrometer and the isotropic RHF and HF theoretical profiles are listed in table 3.3. Both theoretical profiles have been convoluted with Gaussians of FWHM=0.4a.u.

Figure 3.18 shows the differences between the directional profiles of lead obtained from measurements with 412keV and 60keV γ-radiation. Taking into account the poor quality of the low energy data (i.e. $\pm 0.62\%J(0)$) and modest statistical accuracy of the high energy data ($\pm 0.39\%J(0)$), it can be seen that both measurements are in mutual agreement.

The experiment exhibits only a small anisotropy ($\sim 1\%J(0)$) which is just distinguishable within the statistical error. Examination of figure 3.18 reveals that the anisotropy appears

P_z	Experiment 100	Experiment 110	Experiment 111	Relativistic Free atom	Nonrelativistic Free atom
0.0	10.252 ± 0.040	10.095	10.141	10.980	11.470
0.1	10.177	10.018	10.169	10.881	11.346
0.2	10.64	9.869	10.100	10.598	10.991
0.3	9.837	9.684	9.897	10.175	10.461
0.4	9.519	9.443	9.620	9.669	9.839
0.5	9.218	9.062	9.259	9.140	9.213
0.6	9.773	8.653	8.825	8.637	8.650
0.7	8.281	8.293	8.310	8.193	8.181
0.8	7.862	7.886	7.839	7.820	7.809
0.9	7.471	7.479	7.449	7.510	7.512
1.0	7.148	7.109	7.123	7.248	7.265
1.2	6.683	6.687	6.639	6.799	6.833
1.4	6.221	6.209	6.239	6.370	6.409
1.6	5.846	5.887	5.845	5.926	5.966
1.8	5.400	5.370	5.403	5.476	5.513
2.0	5.025	5.055	4.973	5.043	5.077
2.5	4.053	4.082	4.129	4.130	4.185
3.0	3.489 ± 0.031	3.474	3.506	3.513	3.569
4.0	2.843	2.844	2.847	2.842	2.852
5.0	2.484	2.844	2.847	2.399	2.377
6.0	2.805	2.099	2.085	1.990	1.990
7.0	1.737	1.770	1.715	1.016	1.044

Table 3.3 Experimental and theoretical Compton profiles of lead along 100, 110 and 111 measured on the high energy spectrometer. The relativistic and nonrelativistic free atom values are taken from Biggs et al (1975) and Mendelsohn et al (1974) respectively. Both theories have been convoluted with a Gaussian of FWHM 0.4a.u. to mimic the experimental resolution half width.
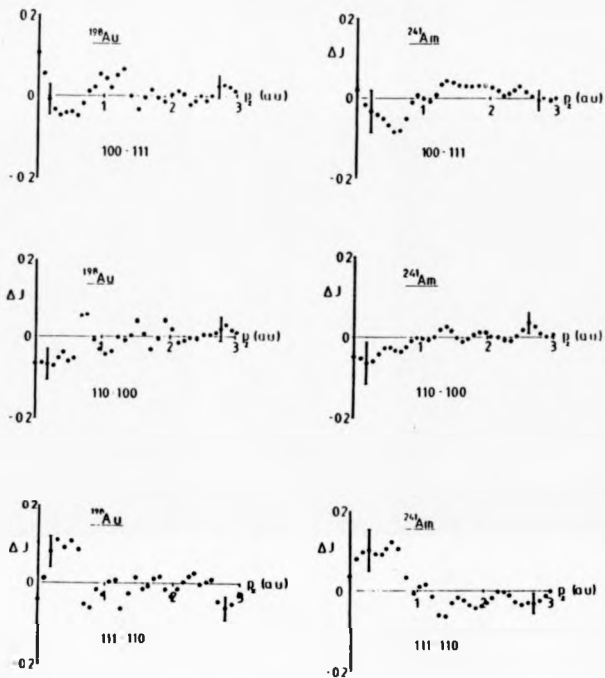
Figure 3.18 The profile anisotropies of lead measured with 412keV and 60keV γ-radiation.

to be associated with the 111 direction and corresponds to a shift in electron density from the region $0.75 < p_z < 1.5$a.u. to the region $p_z < 0.75$a.u.

Figure 3.19 shows the difference between a spherical averaged experimental profile formed from the weighted average, $\frac{6\times[100]+12\times[110]+8\times[111]}{26}$ and the theoretical profiles. All three profiles are identical at high momentum but the experiment clearly favours the relativistic calculation at low momentum. Relativistic flattening of the momentum distribution is evident here as a shift of electron density from the low momentum region, $p_z < 0.4$a.u. to the region $0.4 < p_z < 1.0$a.u. .

3.5 Conclusions.

Until recently, Compton scattering research has been, in general, concerned with the systematic study of the periodic table, in particular the first series transition metals. An understanding of the many complex energy dependent corrections employed to extract $J(p_z)$ from the measured energy spectrum has enabled Compton profiles to be deduced with high statistical accuracy (typically $\sigma \leq \frac{1}{2}\%J(0)$). The experimental results presented in this chapter demonstrate that Compton scattering research is not limited to 'simple' elemental systems and that high precision profiles (for example $\sigma < \frac{1}{2}\%J(0)$ for GaAs) may be obtained from disordered alloy systems (e.g. $Fe_{0.7}Ni_{0.3}$), compound semiconductors (e.g. GaAs) and even very heavy elements (e.g. Pb).

Excellent agreement is observed between the experimental profile anisotropies and B-functions of GaAs and those derived from the pseudopotential calculation. Although the pseudopotential approach is well suited to describing the momentum anisotropy and real space behaviour of the valence electron density of GaAs, this study shows that the theory is unsuccessful in describing the total electron density distribution. This may be attributed to the omission of the core orthogonalisation terms from the pseudo-valence electron wavefunctions.

The rigid band approximation portrays a much simplified representation of the electron density of $Fe_{0.7}Ni_{0.3}$ however, it still enables a qualitative description of the observed features
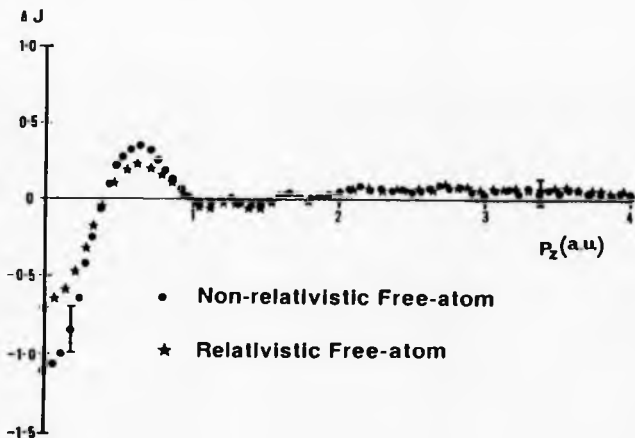
Figure 2.19 The difference between the experimental and theoretical absolute Compton profiles of lead.

of the measured profiles. A corrected KKR-CPA calculation of the directional Compton profiles of this alloy is presently underway and will hopefully, enable a more quantitative interpretation of these data.

The experimental spherical average Compton profile of Pb clearly favours the RHF profile over the HF profile. The RHF profile was also favoured over a profile constructed from a RHF core plus a contribution from a conduction band ($6s^2 6p^2$) formed from a noninteracting homogeneous free electron gas with a Fermi momentum of p_f=0.835a.u.. The two free atom theories enable only a qualitative interpretation of these data and a relativistic band structure calculation of the electron momentum density is necessary before a quantitative interpretation of these data is possible. Kubo and Yamishita (1986) have already calculated a self consistent relativistic band structure of lead at normal and high pressure using the symmetrised relativistic APW method and as a result of this work, the directional Compton profiles of Pb are presently being calculated (Kubo, private communication).

Chapter 4

MAGNETIC COMPTON SCATTERING.

4.1 A Review of Magnetic Photon Scattering.

The existence of spin dependent terms in the x-ray scattering cross section provide a means to study the properties of the spin oriented electrons in magnetic materials. Spin dependent scattering was first used by nuclear physicists to determine the net circular polarisation of γ-rays created by a nuclear reaction or by a decaying nucleus. The degree of circular polarisation P_3 was obtained by monitoring the magnetic field dependence of the total intensity of radiation Compton scattered by polarised electrons in a piece of magnetised iron (Biedenharn, Rose and Arfken , 1951).

Recall from section 1.5, the expression for $|\mathbf{M}|^2$ (equation 1.45) obtained for the situation where the electron orbital momentum is completely quenched. In this case $|\mathbf{M}|^2$ becomes,

$$|\mathbf{M}|^2 = (\epsilon_2 . \epsilon_1)^2 - i\frac{\hbar\omega_1}{m_0 c^2}(\epsilon_2 . \epsilon_1)(\mathbf{s}_j . \mathbf{B}) + \left(\frac{\hbar\omega_1}{m_0 c^2}\right)^2 (s_j^2 B^2). \tag{4.1}$$

Note that the spin dependent terms appear imaginary when considered to first order (i.e. $\hbar\omega_1/m_0 c^2$) and only make a real contribution when taken to second order (i.e. $(\hbar\omega_1/m_0 c^2)^2$) . It is this second order term which is responsible for magnetic effects observed with unpolarised or linearly polarised radiation.

In the past 30 years various photon scattering experiments have been devised to study the behaviour of polarised electrons in ferro-, ferri- and antiferromagnetic systems by measuring the first and second order spin dependent contributions to the x-ray scattering cross section.

A review of these experiments will now be presented. For convenience it is split into two sections. The former deals with the experiments concerned with second order spin dependent effects and the latter with experiments which study first order spin dependent scattering (magnetic Compton scattering falls into this category).

4.1.1 Second Order Magnetic Scattering.

The $s^2 B^2$ term in equation 4.1 represents pure magnetic scattering and for x-ray energies this term is small. For example, for $\omega_1 = 10$keV, the factor $(\hbar\omega_1/m_0 c^2)^2$ represents almost a four order of magnitude reduction in scattered intensity compared with the leading Thomson term. Aside from this factor the magnetic scattering amplitude is further reduced by the fact that only the magnetic electrons contribute to this scattering. The ratio R of magnetic to charge scattering cross sections is,

$$R = \frac{\sigma_{magnetic}}{\sigma_{charge}} = \left(\frac{\hbar\omega_1}{m_0 c^2}\right)^2 <s>^2 \left(\frac{N_m}{Z}\right)^2 \qquad (4.2)$$

where $<s>$ is the average electron spin and N_m is the number of magnetic electrons.

The existence of the $s^2 B^2$ term was established by Gunst and Page (1953) by measuring the transmission of 2.62MeV unpolarised γ-rays through a piece of iron magnetised along the transmission direction. Gunst and Page isolated the spin contribution from the non-magnetic scattering by forming the ratio $\sqrt{(I_m - I_{nm})/I_m}$ where I_m and I_{nm} are the transmitted intensities through the magnetised and unmagnetised iron sample respectively. They proved that this ratio is directly proportional to the spin dependent part of the total Compton cross section.

In 1970 Platzman and Tzoar predicted that very weak but observable superlattice peaks, similar to those obtained in neutron diffraction experiments on antiferromagnetic materials, would be obtained in x-ray diffraction experiments. Using unpolarised radiation from a 1kW copper anode x-ray tube de Bergevin and Brunel (1972) observed two such superlattice x-ray diffraction peaks $((\frac{1}{2}, \frac{1}{2}, \frac{1}{2}),$ and $(\frac{3}{2}, \frac{3}{2}, \frac{3}{2}))$ which disappeared above the Néel point (250°C), from antiferromagnetic NiO. The intensities of the superlattice peaks were 4×10^{-8} smaller than the normal diffraction peaks in line with the predictions of Platzman

and Tzoar (1970). This pioneering experiment confirmed the existence of photon diffraction by electronic spins. The experiment was repeated (Brunel and de Bergevin, 1981) for the antiferromagnet hematite (Fe_2O_3) using a 1.1kW rotating anode source and again magnetic superlattice Bragg reflections were observed.

Using a 12kW rotating anode source Gibbs, Moncton and D'Amico (1985) measured the temperature dependence of the magnetic satellites of the antiferromagnetic phase of holmium and then repeated the experiments using synchrotron radiation from the 54-pole wiggler beam line at the Stanford synchrotron radiation source (Gibbs, Moncton, D'Amico, Bohr and Grier, 1985). As the synchrotron radiation was predominantly linearly polarised in the horizontal plane a post sample germanium monochromator with a Bragg angle 45° could be used to eliminate the Thomson scattering. The high flux, highly collimated photon beam associated with synchrotron radiation resulted in a factor of 30 improvement in the resolution over the laboratory x-ray experiment and lead to the discovery of a spinslip system (see Bohr, Gibbs, Moncton and D'Amico, 1986 for an explanation of the spin slips and lattice modulations on holmium and Moncton, Gibbs and Bohr, 1986 for a review of their results on holmium with the emphasis on the experimental aspects). Furthermore, when the incident photon energy was tuned through the L_3 absorption edge (8.067keV) of holmium a surprising fifty fold resonant enhancement in the magnetic signal was observed (Gibbs, Harshman, Isaacs, McWhan, Mills and Vettier, 1988). This magnetic resonance has been attributed to electron multipole transitions to unoccupied orbitals. These transitions result in an exchange interaction which is sensitive to the f and d band magnetisation (Hannon, Trammell, Blume and Gibbs, 1988). Hannon et al predict that for rare earth metals this enhancement of the magnetic scattering cross section will also occur at the L_2, M_2 and M_3 absorption edges. More recently a similar high resolution x-ray scattering study of the magnetic structure of the rare-earth erbium has been performed and a further spin slip discovered (Gibbs, Bohr, Axe, Moncton and D'Amico, 1986) although the effect was not as large as in holmium.

4.1.2 First Order Interference Effects.

The ratio R given by equation 4.2 is small, 10^{-5}-10^{-6} for pure magnetic scattering . Fortunately in antiferromagnetic materials the magnetic and charge distributions do not coincide in reciprocal space and the small magnetic contribution to the scattering can be separated from the dominant charge scattering. However for ferro- and ferrimagnetic systems the two distributions do coincide and the pure magnetic scattering is indistinguishable from the charge scattering.

It was mentioned in section 1.5 that a real first order magnetic contribution to the scattering can be obtained if the polarisation product $\epsilon_2.\epsilon_1$ is made complex. Then, a further real contribution arises due to the interference of the charge and magnetic scattering terms which is proportional to the $i(\epsilon_2.\epsilon_1)(\mathbf{a}_j.\mathbf{B})$ term in equation 4.1. Using this term to study magnetism in preference to the second order term somewhat alleviates problems associated with the small size of the second order term but it does introduce another. How can $\epsilon_2.\epsilon_1$ be made complex ?

In a diffraction experiment $\epsilon_2.\epsilon_1$ would be complex if the atomic structure was non-centrosymmetric however most common ferromagnets, in particular elemental ferromagnets, are centrosymmetrical. In such centrosymmetrical structures it is still possible for the scattering amplitude to be complex under the conditions of anomalous dispersion. Using the fortuitous proximity of the CuKα x-ray energy ($E_{K\alpha}$=8.04keV) and the Fe K shell binding edge (E_K=7.11keV) de Bergevin and Brunel (1981) were able to measure the large anomalous scattering of the CuKα radiation in ferromagnetic iron and ferrimagnetic Zn substituted magnetite. For example, for the 222 reflection of iron, $\frac{f''}{f_0} = \frac{1}{2}$ and the flipping ratios obtained upon reversal of the magnetic field amounted to parts in 10^3. The same principle was applied by Vettier, McWhan, Gyorgy, Kwo, Huntschub and Batterman (1986) but using a tunable synchrotron source instead of a fixed wavelength x-ray source to determine the modulation in the magnetic moment in a superlattice composed of alternating regions of ferromagnetic Gd and nonmagnetic Y. Here flipping ratios of the order of 1% were found upon reversal of the spin direction in the 40 layer interface. The above methods for obtaining a real overlap

term in the scattering cross section are unsuitable for magnetic Compton scattering studies because firstly , $n(p)$ is always centrosymmetric, even when $\rho(r)$ is not and secondly the IA is invalid (see section 1.3.3) under the condition of anomalous dispersion.

A further possibility for forcing the polarisation product to be complex is to use circularly polarised radiation (CPR). Platzman and Tzoar (1970) demonstrated that with such a probe Compton scattering could be employed to measure the momentum distribution of electrons with unpaired spins. The first such experiment was performed by Sakai and Ono (1976, 1977) using a cooled oriented radioisotope source (^{57}Co) as a source of 122keV circularly polarised γ-radiation. The activity of the source was limited to 10mCi by heating effects caused by self-absorption which prevented cooling below ~50mK. In this experiment photons were scattered through 135° by a 1cm thick magnetised polycrystalline iron sample. The magnetising field was reversed in an asynchronous cycle and the Compton scattered radiation for each reversal was recorded. Only 4×10^6 counts were accumulated in the difference profile in 140 hours of measurement. The central dip of the difference profile was approximately three times that predicted by an APW calculation (Wakoh and Kubo, 1977) although the significance of the dip could not be established due to the poor statistical accuracy of their results (error in the peak of the difference profile was approximately $\pm 28\% J_{mag}(0)$).

More recent experiments employing a similar method to that described above have been employed by Sakai, Terashima and Sekizawa (1984) and Sakai and Sekizawa (1987). In these experiments nuclear orientation in the ^{191m}Ir isotope was used to provide a slightly higher energy source (129keV) of circularly polarised radiation. This new isotope was chosen because the ^{191m}Ir nuclei can be sufficiently aligned at 100mK to produce γ-radiation with a higher degree of circular polarisation than the ^{57}Co isotope ($P_3 \sim 0.8$ compared with ~ 0.3) used in the initial experiment. This enabled a higher activity source (40mCi) to be used. With this source Sakai et al were able to remeasure the magnetic Compton profile of iron with an improvement in precision of almost two orders of magnitude (6.4×10^8 in 165 hours) and were also able to make the first measurements of a ferrimagnet (manganese ferrite). Simon and Daniel (1977) also obtained CPR from a cooled radioisotope source (^{191m}Ir) and used it to measure the spin dependence of the Rayleigh scattering cross section. They report the spin

66

dependent part of the cross section to be of the same sign as the spin dependent Compton scattering cross section.

It is possible to create CPR by converting linearly polarised radiation, which synchrotrons produce in abundance, to CPR with the aid of an x-ray quarter wave plate. Such a device was developed by Golovchenko, Kincaid, Levesque, Meixner and Kaplan (1986), at the Cornell high energy synchrotron source (CHESS) but the device was limited to a 15% conversion efficiency and an energy of 17.5keV. A similar device but operating at a higher photon energy of 40keV has since been used to measure the magnetic Compton profiles of ferromagnetic Fe, Ni, Co and Gd (Mills, 1988), the gadolinium being cooled below its Curie temperature T_c (293 K). These devices can offer only limited tunability and are therefore unsuitable for diffraction experiments. Compton studies do not require a tunable source but would benefit from an improvement in the conversion efficiency and an extension of the ω_1 range of the device.

Although synchrotron radiation is generally described as being almost completely linearly polarised in the plane of the orbiting electron, out of this plane the radiation is elliptically polarised. Both Holt and Cooper (1983) in a feasibility study of magnetic Compton studies and Brunel, Patrat, de Bergevin, Rousseaux and Lemmonier (1983) in a diffraction study of zinc ferrite ($Zn_{0.5}Fe_2O_4$) realised this was a potential source of CPR and set about extracting it by viewing the radiation emitted off axis from a bending magnet i.e. at a small angle to the orbital plane. This 'inclined view method ' for obtaining circularly polarised synchrotron radiation (CPSR) is described in detail in section 4.2.3 .

The first magnetic Compton study using this technique was performed at the SRS at Daresbury Laboratory on polycrystalline ferromagnetic iron (Holt, Laundy, Cardwell, Cooper, Naylor, Manninen and Hatton, 1986) . The high photon energies required for Compton studies were obtained by viewing the radiation emitted 'off axis' from an asymmetric superconducting 5T wiggler magnet for which the critical wavelength is a quarter ($\lambda_c = 0.83\lambda$ at 5T) of the critical wavelength of a bending magnet ($\lambda_c = 3.9\lambda$ at 1.2T). This first magnetic Compton profile measurement served only to demonstrate the viability of the inclined view method for obtaining a significant flux of high energy CPSR. The development of the tech-

nique and subsequent measurements constitute the remainder of this thesis and include; the first established magnetic Compton profile lineshape of ferromagnetic iron (Cooper, Laundy, Cardwell, Timms, Holt and Clark, 1986), the magnetic Compton profile of cobalt (Timms, Brahmia, Collins, Collins, Cooper, Kane, Clark and Laundy, 1988) and the first measurement of the magnetic anisotropy in the electron momentum density of iron (Cooper, Collins, Timms, Brahmia, Kane, Holt and Laundy, 1988).

The inclined view method has also been used at the DORIS storage ring to obtain CPSR which was used to study the small spin dependent contribution to the photoabsorption cross section (Schütz, Wagner, Wilhelm, Kienle, Zeller, Frahm and Materlik, 1987) in iron by magnetic EXAFS (extended x-ray absorption fine structure) and XANES (x-ray absorption near edge structure). The experiment is possible because the circular polarised photon creates a partially polarised photoelectron from the unpolarised 1s state and the transition probability for this polarised photoelectron is different for transitions to spin up states and spin down states. This kind of experiment is only possible with a tunable source of circularly polarised radiation such as CPSR.

It is apparent from the review that the existence of spin dependent terms in the x-ray scattering cross section was established both experimentally and theoretically more than a quarter of a century ago. However because of the small cross sections involved and the requirement for polarised beams or polarisation analysis of the scattered beam, the magnetic effects produced by these terms have until recently remained unexploited. Many different experiments have been reviewed, the attention of this thesis will now return to the Compton interaction. In the next section the magnetic Compton experiment is introduced and the technique employed for obtaining CPSR is discussed.

4.2 Magnetic Compton Scattering with CPSR.

4.2.1 Introduction.

If the total electron momentum density distribution is to be studied, polarised photon beams and polarisation analysis of the scattered beam are unnecessary. Such experiments are per-

formed with either conventional x-ray sources or more usually radioisotope γ-ray sources such as those described in chapter 2. However the advent of storage rings capable of producing high fluxes of hard x-radiation has meant high resolution focusing crystal x-ray spectrometers (e.g. 0.05a.u. compared with 0.4a.u. for the best γ-ray spectrometers) are now becoming feasible (see Loupias and Petiau, 1980 and Sakai et al, 1989) Obviously it would be advantageous if similar information could be obtained just about the behaviour of the electrons responsible for the ferromagnetism in magnetic materials.

As shown in section 1.5, it is possible to isolate scattering from the unpaired electron spins in a ferromagnet. However this necessitates the use of circularly or elliptically polarised photon beams and unfortunately such polarised sources are not generally available with sufficient intensity and at the energies ($\omega_1 > 40$keV) required for Compton experiments. Despite this, various techniques have been devised in order to obtain useful sources of CPR (see review section 4.1) and preliminary measurements of the magnetic Compton profile, $J_{mag}(p_z)$ have been made. Recall the expression for $J_{mag}(p_z)$ derived in section 1.5.1 ,

$$J_{mag}(p_z) = \int \sum_j (n_{j\uparrow}(\mathbf{p}) - n_{j\downarrow}(\mathbf{p})) d^3\mathbf{p}. \qquad (4.3)$$

In these 'magnetic Compton' experiments $J_{mag}(p_z)$ is obtained by forming the difference of two scattered spectra recorded with either CPR of opposite hands or with the direction of the magnetisation within the sample reversed. This operation enables the core contribution from the paired electron spins to be removed. Therefore the magnetic Compton profile like its non-magnetic counterpart, $J(p_z)$ is particularly sensitive to the valence and conduction electrons and results in the isolation of the unpaired electron spin momentum density.

Although $J_{mag}(p_z)$ is only a 1-dimensional projection of the spin density it is strongly directionally dependent. A further important property of $J_{mag}(p_z)$ is that unlike neutron and x-ray diffraction experiments where the number of data points is limited to the few reflections sensitive to the magnetic interaction, $J_{mag}(p_z)$ offers a continuous function and enables a more quantitative comparison with theory. In addition magnetic x-ray scattering offers the possibility of obtaining separate information about the spin and orbital density distributions (see section 1.5) which is in contrast to neutron scattering experiments where

the neutron is scattered solely by virtue of its magnetic moment and therefore measures the total, spin plus orbital magnetisation density.

The magnetic Compton scattering cross section is small (a factor ω_1/m_0c^2 smaller than the Thomson term) and therefore a high flux of high energy CPR is required in order to obtain statistically accurate data. For example, at 60keV the magnetic intensity is only 1% of the total scattering. This means 10^6 counts must be accumulated to yield 10% accuracy in the magnetic difference profile (see figure 4.1) and to obtain 1% accuracy requires 10^8 counts. In this study the 'inclined view method', which is described in detail in the remainder of this section, has been used to obtain this high flux, high energy CPR.

4.2.2 General Properties of Synchrotron Radiation.

In storage rings such as the SRS (Synchrotron Radiation Source) at Daresbury, synchrotron radiation is produced by electrons traveling with highly relativistic velocities which are confined to a circular orbit by a series of dipole bending magnets. The 'classical' picture for the geometry of synchrotron emission is shown in figures 4.2a and 4.2b (taken from Tomboullan and Hartman, 1956). The angular distribution of the emitted intensity from a slow electron undertaking a circular orbit is shown in figure 4.2a. For a relativistic electron traveling with a velocity close to the speed of light the emission is distorted into a narrow cone in the direction tangential to the electron orbital plane (see figure 4.2b). The emitted intensity is not confined to the fundamental frequency of revolution but as a consequence of the relativistic motion of the electron the emitted spectrum is strongly Doppler shifted and depending on the machine dimensions and the energy of the electron, extends typically from the infra-red region ($\sim$10eV) to the hard x-ray region ($\sim$100keV), see figure 4.3a.

For x-ray studies synchrotron radiation has three important attributes, namely, it is an intense, tunable source of high energy radiation. It is a highly collimated source of small angular size (e.g. for the SRS operating at an energy of 2GeV, $\frac{mc^2}{Energy}$ =0.025mrad) and therefore is an extremely bright source of low emittance (e.g. SRS emittance of 2.6×10^{-3} mrad^{2}mm^2 from a bending magnet). As indicated by figure 4.3b, the brightness of the source (i.e the number of photons /s/mrad^2/mm^2/mA/0.1% bandpass) is typically several orders
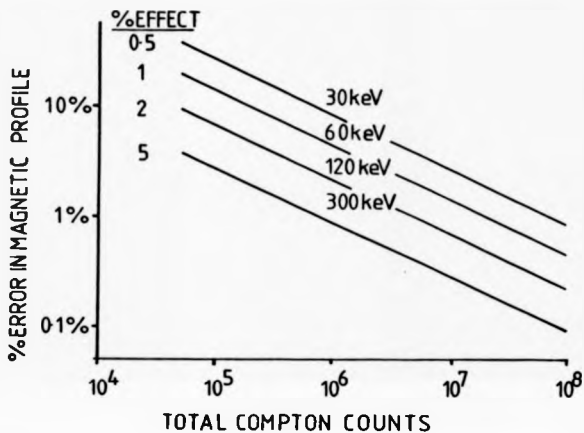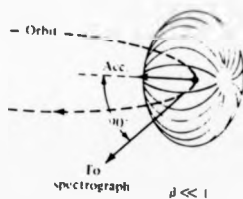
70

Figure 4.1 Relationship between the error in the magnetic Compton profile and the total integrated Compton intensity. The % effect is given by $\frac{\Delta n_{\uparrow}}{n_{\uparrow}} \frac{N_{\mp}}{Z}$. This figure emphasises the need for a source of high flux, high energy CPSR.

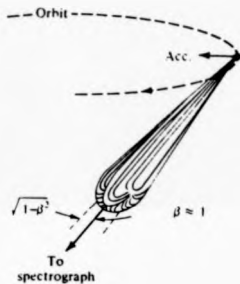**Figure 4.2** The 'classical' picture for the geometry of synchrotron radiation emission (from Tomboulian and Hartman, 1956). (a) The angular distribution of emitted intensity from a slow electron undertaking a circular orbit is distorted into (b) a narrow cone in the instantaneous direction of motion for a relativistic electron moving with a velocity close to the speed of light ($\beta = \frac{v}{c} \sim 1$).
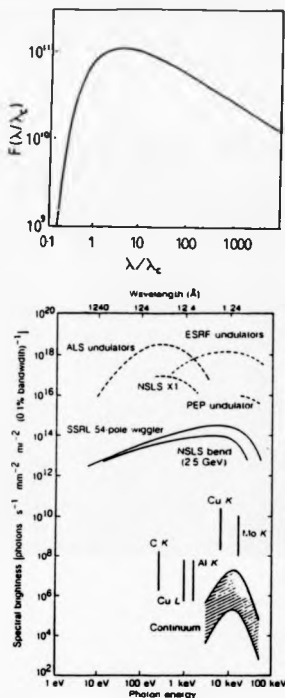
Figure 4.3 Properties of synchrotron radiation. (a) The universal intensity curve for synchrotron radiation sources. The function $F(\lambda/\lambda_c)$ is proportional to the photon flux integrated over all azimuthal angles. (b) The spectral brightness for several synchrotron radiation sources and conventional sources. The indicated two orders of magnitude ranges show the approximate variation that can be expected among stationary anode tubes (lower end of range), rotating anode tubes (middle) and rotating anode tubes with microfocussing (upper end of range). Clearly synchrotron radiation sources are several orders of magnitude brighter than even the brightest conventional x-ray source (from Kim, 1986).

of magnitude higher than that obtainable from a conventional x-ray source. The radiation is also completely linearly polarised in the plane of the orbit and elliptically polarised above and below this plane.

It is possible to shift the emission to higher photon energies by incorporating other magnetic lattices (e.g. wiggler magnets) into straight sections of the electron beam line. This is particularly important for Compton studies where high intensity, high energy ($\omega_1 > 40$keV) photon beams are required. Figure 4.4a is a schematic representation of the magnet lattice arrangement of the 3-pole asymmetric 5T superconducting wiggler magnet which is incorporated into a straight section of the SRS. The central 5T pole provides the displacing field, the 2.5T side magnets restore the electron to its original trajectory (i.e. $\oint \mathbf{B}.\mathbf{dl} = 0$). The variation in the vertical field through the wiggler magnet is shown in figure 4.4b together with the trajectory of the electron beam. At the point of maximum displacement (9mm) the magnetic field is a maximum 5T and the radius of the electron beam is only 1.3m . This is compared with a constant radius of curvature of 5.5m when inside a conventional 1.2T dipole magnet. The effect on the emitted spectrum is shown in figure 4.4c, where the emission of the 3-pole wiggler ($\lambda_c = 0.93\text{\AA}$) is compared to the emission of a 1.2T dipole bending magnet ($\lambda_c = 3.88\text{\AA}$). This figure demonstrates how the wiggler shifts the overall spectrum to shorter photon wavelengths.

4.2.3 The Inclined View Method.

Many different photon spectroscopy experiments benefit from the intense, bright, tunable source of photons that synchrotron radiation offers. In addition, magnetic Compton studies benefit from the unique polarisation of the beam. It was mentioned earlier that in the plane of the machine the emitted radiation is almost entirely linearly polarised with the electric field vector parallel to the machines orbital plane ($E_\parallel$). If radiation is sampled above or below the machines orbital plane it is found to contain a component which has its electric field vector perpendicular ($E_\perp$) to the orbital plane and is in quadrature (i.e. 90° out of phase) with $E_\parallel$. Radiation sampled above or below the orbital plane will in general be elliptically polarised with a degree of circular polarisation (see section 1.4 for a mathematical description

71
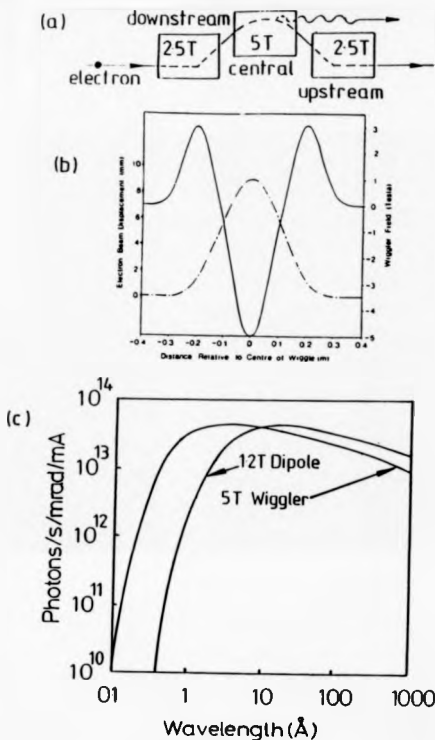
Figure 4.4 The SRS wiggler magnet. (a) A schematic plan view of the 3 pole, 5T (λ_c=0.93Å) wiggler magnet installed in the SRS at Daresbury. (b) The variation of the wiggler field (solid line) and the electron trajectory (broken line) relative to the centre of the magnet (from Greaves, Bennett, Duke, Holt and Suller, 1983) and (c) the intensity per mrad per second produced by this wiggler compared with that obtained from a 1.2T (λ_c=3.88Å) dipole bending magnet (after Holland, 1986).

of circular polarisation) P_3 given by

$$P_3 = \frac{2(I_\parallel I_\perp)^{\frac{1}{2}}}{I_\parallel + I_\perp} \tag{4.4}$$

where $I_\parallel$ and $I_\perp$ are the intensities of radiation polarised parallel and perpendicular to the orbital plane respectively. Experiments using CPSR in the VUV (vacuum ultra-violet) region ($\lambda \sim 10^3 \mathring{A}$) have already been performed (see Heinzmann, Schafers and Hess, 1980 for an example). It is far easier to extract CPSR at these longer wavelengths than at x-ray wavelengths (e.g. $0.15\mathring{A}$) as both $I_\parallel$ and $I_\perp$ are spread over an angular range of several mrads. In the x-ray regime the angular spread is a fraction of a mrad ($\frac{1}{4}$ to $\frac{1}{2}$ mrad for $P_3 > 0.5, \omega_1 = 60\text{keV}$) Shown in figure 4.5a is the variation of $I_\parallel$ and $I_\perp$ with ψ for photon wavelengths of $0.1\mathring{A}$, $0.3\mathring{A}$ and $0.5\mathring{A}$ calculated for the 5T Daresbury wiggler magnet and the pre-HBL (high brightness lattice, see chapter 5) by Holt and Cooper, 1986. Figure 4.5b shows the degree of circular polarisation P_3 and linear polarisation P_l as a function of ψ for two photon wavelengths, $0.2\mathring{A}$ (dashed line) and $0.1\mathring{A}$ (dotted line). This figure demonstrates how P_l is exchanged for P_3 as radiation is sampled further off axis. Together figures 4.5a and b indicate that a significant degree of circularly polarised synchrotron radiation (CPSR) (i.e. $P_3 > 0.5$) can only be obtained at the expense of a significant loss in photon flux, i.e. approximately a factor of 50 for $\omega_1 = 40\text{keV}$. This value is for the pre-HBL SRS, the flux loss for the post-HBL SRS is only a factor of 5 for $\omega_1 = 60\text{keV}$. The reason for this difference and the effect of the HBL are described in chapter 5. The cut of in the $0.1\mathring{A}$ curve in figure 4.5b corresponds to the limit of useful intensity.

The band of the CPSR depends upon the curvature of the electron beam such that a reversal in the curvature of the electron beam results in a change in band of CPSR. Each magnet in the wiggler lattice produces its own emittance of radiation and there will be some cancellation of CPSR of one band emitted from the two end magnets with CPSR of the opposite hand emitted from the central magnet. For the asymmetric wiggler at Daresbury the intensity distribution emanating from the central 5T magnet ($\lambda_c = 0.93\ \mathring{A}$) is shifted in energy relative to that emanating from the 2.5T ($\lambda_c = 1.86\ \mathring{A}$) upstream and downstream magnets. For this reason the cancellation effects are confined to emitted photon energies

72
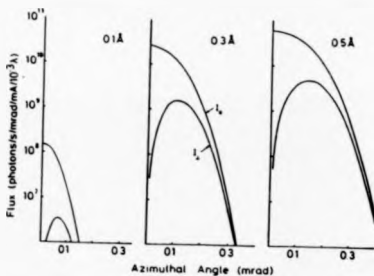
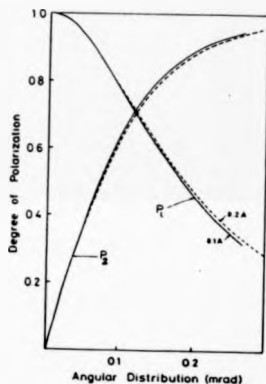Figure 4.5 (a) The intensities of beams polarised parallel ($I_{\parallel}$) and perpendicular ($I_{\perp}$) to the orbital plane as a function of azimuthal angle at wavelengths of 0.1Å, 0.3Å and 0.5Å for the 5T SRS wiggler magnet. (b) The corresponding variation in the degree of circular polarisation, P_3 and linear polarisation, P_1 with azimuthal angle for 0.1Å and 0.2Å radiation (from Holt and Cooper, 1983).

less than 10keV and above this energy there exists a 'polarisation window' (see figure 4.6). A result of this cancellation is that symmetric wigglers and undulators are not capable of producing CPSR.

To summarise, it is possible to exchange photon flux for a high degree of CPSR and vary the band of CPSR from left through linear to right by moving through the orbital plane. The azimuthal angles involved are small ($\sim \frac{1}{4}$ to $\frac{1}{2}$ mrad) but synchrotrons are large machines and the experimental stations may be positioned tens of metres from the tangent point of the ring. At these distances these small angles transform to a workable number of mm (at 37m, $\frac{1}{4}$ mrad corresponds to $\sim$6mm).

4.3 Experimental Details.

4.3.1 Preliminary Considerations.

The ratio of the spin dependent Compton scattering cross section $d\sigma_s$ to the ordinary cross section $d\sigma_0$ was shown earlier as a function of energy and scattering angle in figure 1.5 for the situation where s_j parallel to k_0. Notice that the ratio is largest for large scattering angles and high photon energies. In addition the spin dependent Compton scattering cross section is linearly dependent upon the degree of circular polarisation P_3 of the photon beam. The Compton cross section is generally considered as being small ($\sim$0.1 Barn per electron) and for ω_1=50keV the spin dependent Compton scattering cross section is almost two orders of magnitude smaller than this cross section. To maximise the magnetic scattering requires an experimental strategy where large scattering angles ($\phi > 150°$) and an intense, high energy ($\omega_1 >$40keV) photon beam with a substantial degree ($P_3 >$0.5) of circular polarisation are employed.

In the previous magnetic study (Holt et al, 1986) a high resolution ($\frac{\Delta E}{E} \sim 1 \times 10^{-4}$), vertically displacing Si 220 double crystal monochromator was employed. The energy resolution of Compton studies is usually limited by the energy resolution of the detector (see section 2.5) and the high resolution of the monochromating device used by Holt et al (1986) was unnecessary. A far better strategy would have been to match the energy resolution of
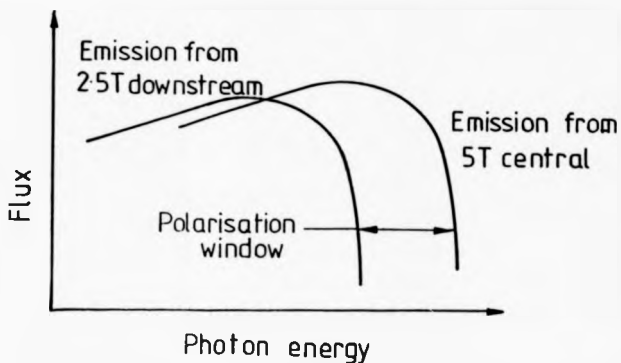
Figure 4.6 Schematic picture of the intensity distribution emanating from the central 5T wiggler magnet (λ_c=0.93Å) and the 2.5T down stream end magnet (λ_c=1.86Å). Cancellation of CPSR of one hand emanating from the central magnet with CPSR of the opposite hand from the end magnets is restricted to energies below ~10keV. Above 10keV there exists a polarisation window where the polarisation cancellation is minimal.

the monochromator to the energy resolution of the detector thereby increasing the integrated intensity at the expense of the energy spread of the 'monochromated beam'.

In fact, optimisation of the monochromator resolution was not undertaken until a later study and is discussed in detail in a later section (5.2.5). However the need for some optimisation was realised and the question of which monochromator design and material would be most suitable was addressed. The angular widths, ω_s, the relative energy resolution $\Delta E/E$ and the integrated reflecting power, R for CuKα radiation are given in table 4.1 for a few reflections of Si and Ge,

For a given energy the angular widths of the Ge reflections are some 50% larger than the corresponding Si reflection, as are the reflecting powers. Because the energy resolution of the monochromator is negligible compared with the energy resolution of the detector ($\frac{\Delta E}{E} = 6 \times 10^{-3}$ @ 60keV) the larger reflecting power offered by Ge makes it a superior choice of monochromator to Si for these studies.

The double crystal monochromator design chosen by Holt et al (1986) is unsuitable for obtaining high energy monochromatic radiation. To obtain an intense high energy reflection (e.g. $\omega_1 > 50$keV) from such a device necessitates a small Bragg angle $\sim 3.5°$. To maximise the incident flux onto the sample, the sample slits must be opened as wide as is practicable. However at such small Bragg angles the reflected beam from the first crystal tends to overshoot the second crystal and so a compromise between photon energy and intensity must be made.

A long (80mm), 25mm wide single crystal of Ge 111 was used for this study. The surface of the crystal was already roughed slightly. This reduced the energy resolution of the 333 reflection from the intrinsic width of $\frac{\Delta E}{E} = 2 \times 10^{-5}$ to $\frac{\Delta E}{E} \sim 500 \times 10^{-5}$ thereby increasing the integrated intensity of the reflection. The 333 Bragg reflection was chosen as it afforded a higher Bragg angle for the same energy than the primary 111 reflection (i.e. for $\omega_1 = 50keV$ 2.2° (111) compared with 6.6° (333)). The deficit in flux suffered as a result of using the 333 Bragg reflection (factor of 4) was almost countered by the larger portion (more than a factor of 3) of the synchrotron beam which could be used. This is discussed in more detail in connection with   the new spectrometer in the next chapter.

material	hkl	$\Delta E/E$ $\times 10^5$	R $\times 10^5$	ω_s secs.
silicon	111	14.1	39.9	7.395
	220	6.04	29.7	5.459
	333	0.88	9.9	1.989
	440	0.96	14.0	2.675
germanium	111	32.64	85.9	16.338
	220	14.46	67.4	12.449
	333	2.00	20.2	4.127
	440	2.14	27.5	5.339

Table 4.1 Properties of selected reflections of CuKα radiation from intrinsic monochromator crystals (adapted from Matsushita and Hashisume, 1983).

4.3.2 Experimental Environment.

The wiggler beam line W9 has an aperture of 64mrad which is centred on the emitted fan of 102mrad and transmits 70% of the total power emitted from the wiggler (see Greaves, Bennett, Duke, Holt and Suller, 1983).

In a previous study (Holt et al, 1986) performed on the powder diffraction station (W9.1) a certain degree of polarisation cancellation was noted. This was attributed to CPSR from the central bending magnet canceling with CPSR of the opposite hand emitted by the upstream 2.5T magnet. Further experimental problems associated with station W9.1 were also encountered. Because W9.1 is only 16m from the tangent point, the beam heating can be quite severe. This heating was responsible for the malfunction of the main slit mechanism which in turn reduced the extent to which the experimental conditions could be varied. Also the experimental 'hutch' was small and cramped which made access to the apparatus difficult and made optimising the experiment at the beginning of each machine refill time consuming and arduous. As a result of these problems more than half the available intensity was lost.

The decision to perform the present study on W9.4 alleviates many of the problems encountered on W9.1 . The risk of polarisation cancellation was removed because W9.4 receives only radiation emitted by the central 5T magnet and does not view either of the side magnets. Station W9.4 is some 37m distant from the tangent point and the vertical displacement required to obtain CPSR by the inclined view method at W9.4 is more than twice the corresponding displacement on W9.1. Thus a larger vertical source height can be employed. Furthermore, at this extended distance from the tangent point the effects of beam heating are less severe. In general, W9.4 is fully automated and more spacious than W9.1 and offers a more suitable working environment for magnetic Compton studies which are non-standard experiments for W9.4 (i.e. not topography) performed with non-standard apparatus.

4.3.3 Experimental Method.

The experimental arrangement is shown schematically in figure 4.7. The photon beam was selected by a series of three collimating slits of which only one is shown in figure 4.7. The
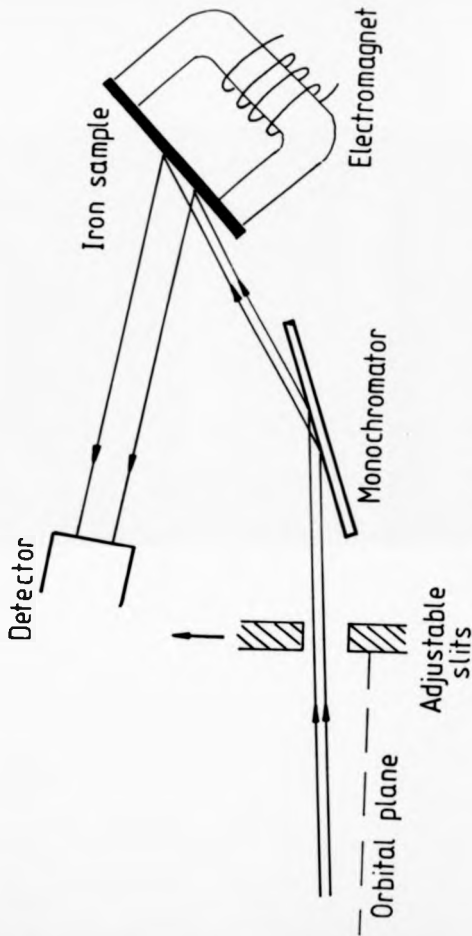
Figure 4.7 Schematic diagram of the experimental arrangement on the topography port, W9.4 on the wiggler beam line used to detect magnetic Compton scattering from polycrystalline iron.

first slits (source slits) were situated near the tangent point of the electron orbit and enabled the beam intensity to be controlled. The other two sets of collimating slits were situated inside the experimental hutch. The slits nearest the sample (sample slits) were adjusted to define a beam size of 7mm wide × 5mm high . The other slits (antiscatter slits) were similarly adjusted and served to reduce small angle scattering of radiation from the inside of the vacuum beam line.

To obtain CPSR the inclined view method described in section 4.2.3 was employed. The white beam of synchrotron radiation was monochromated by a Ge 111 single crystal which was oriented at an angle of 7.3° to select an energy of approximately 45keV with the 333 Bragg reflection. Aside from the useful high energy photons arising from the 333 and 444 Bragg reflections a substantial degree ($\sim$ 90%) of the monochromated beam was comprised of low energy photons ($\sim$15keV) selected by the 111 reflection. These low energy photons were removed by a 2mm thick aluminium filter placed in the scattered beam path. For this filter $\frac{I}{I_0}$=0.16 for ω_1=20keV and $\frac{I}{I_0}$ = 0.82 for ω_1=50keV. The post-monochromated radiation was collimated to remove any spurious reflections and scatter from the monochromator and also from the surrounding lead shielding by a set of finely adjusted tungsten slits situated near the sample. The sample used in this study was a piece of polycrystalline soft iron 40mm wide × 100mm long × 5mm thick which was strapped across the poles of a horseshoe shaped electromagnet. The saturation magnetic field was achieved by passing a current of 0.5A through the 800 turns of the electromagnet. For such a current the magnetic field at the surface of the sample was measured to be $\sim$0.4T (Cardwell, 1987). This was more than twice the field required to completely saturate the sample (0.17T). The magnetic field was reversed at 10 and 20 second intervals in an asynchronous cycle of period 80 seconds and the data switched between two memory stores of an Ortec 4096 mca at each reversal.

A BBC computer was used to control both the data switching and the magnetic field reversal. The magnetisation direction and the scattering vector were aligned as parallel as possible so as to maximise the magnetic scattering (i.e maximise $s_1.B$ in equation 1.46). The scattering angle was 151° ± 2° which was as close to backscattering as practicable, (recall, $d\sigma_s/d\Omega_0$ is a maximum for $\phi = 180°$ (refer to figure 1.5)). The scattered radiation

was detected by a high purity germanium solid state detector and the intensity onto the monochromator was continuously monitored throughout the experiment by an ionisation chamber positioned immediately after the sample slits.

After an initial experiment 'on orbit' which yielded the anticipated null result because $P_3 = 0$ in equation 1.46 , the apparatus was moved up 9mm in the vertical plane to collect radiation emerging at an angle of 0.24mrad from the source some 37m away. As the SRS operates on 8 hour cycles each run was timed for 6 hours. Two such runs were performed and with the SRS operating at an energy of 2GeV and an initial beam current of >300mA and a total of 2×10^9 counts were accumulated under both the spin up and spin down profiles.

4.4 Results.

Figure 4.8a shows a typical spectrum taken from one half of the 4096 channel mca and represents the scattered intensity from one spin orientation in the magnetised iron. The 333 and 444 elastic lines are at 46.4keV and 61.9keV and are clearly separable from their respective, broader Compton profiles which for the scattering angle of $151° \pm 2°$ are centred at 39.7keV and 50.4keV respectively. The difference profile of two 6 hour runs is shown in figure 4.8b which was accumulated in two 8 hour shifts. Notice that the elastic lines have canceled (as did the Fe x-ray fluorescence lines which are not shown) because at small values of $\sin\theta/\lambda \sim 4 \lambda^{-1} (\theta = \phi/2)$ only the spin paired core electrons have a significant form factors. Two magnetic Compton profiles from the 333 and 444 Bragg reflections of the monochromator are left in the difference spectrum and are centered on their respective total profiles. Even in the raw data the predicted central dip in the magnetic Compton profile is quite visible.

Subtracting the spin up and spin down spectra not only isolates the unpaired electron spin contribution to the scattering but also removes any systematic errors inherent in the two data sets. Short term fluctuations in intensity caused by instabilities in the electron beam and longer term fluctuations caused by drift in the electronics and the decay of the source were effectively removed by using a short period asymmetric switching cycle. The evidence for this statement is in the complete cancellation of the elastic lines which confirms
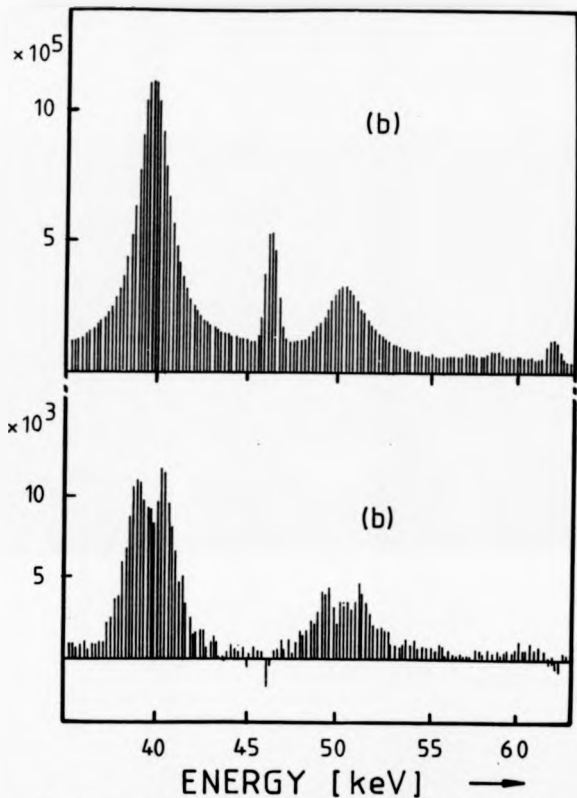
77

Figure 4.8 Experimental Compton profiles of iron: (a) the total profile of one spin orientation and (b) the magnetic difference profile. The elastic lines at 46.4keV and 61.8keV correspond to radiation selected by the 333 and 444 reflections of the Ge monochromator. The corresponding Compton profiles are at 38.7keV and 50.4keV respectively. Each count refers to a 100eV energy bin.

that the data is free from systematic errors. The only discrepancy is around 60keV where the difference profile should be zero but in fact is slightly positive. This small contribution is a further magnetic Compton profile arising from the 77keV radiation produced by the 555 Bragg reflection of the monochromator and is approximately 10% of the 444 magnetic Compton profile. Additional measurements were made to confirm that this was in fact a magnetic effect. Firstly a measurement 9mm below the orbital plane was performed and secondly one with the magnetic field cycle reversed. In each case all of the magnetic Compton profiles including the 555 profile were inverted .

A total of 3.6×10^5 counts were accumulated under the 333 difference profile. This is a factor of ~30 improvement over the previous experiment performed using CPSR extracted from the SRS (Holt et al, 1986). The difference profile was about 1% of the total Compton scattered intensity which is in line with calculations for CPSR of this particular energy (see equation 4.2).

Before comparison with theory the data were corrected for the energy variation of both the Compton cross section and sample absorption. The data were then converted to a momentum scale using equation 1.20 and the magnetic Compton profiles were then normalised to have the same area as the theory in the range $|p_z| < 5.0$a.u. i.e. 2.10 electrons. No corrections for either detector or system resolution or multiple scattering were made. To improve the statistical accuracy of the data the final profiles were averaged from left to right and then displayed on a 0.2a.u. momentum interval. The combined momentum resolution of the germanium detector and that due to geometrical broadening limited the profile resolution to 1.0a.u. FWHM for the lower energy 333 profile and 0.8a.u. FWHM for the 444 profile. The momentum resolution of these results is considerably worse than in nonmagnetic experiments but this can be tolerated because the magnetic Compton profile is twice the width of the all electron profile.

The final processed 333 magnetic Compton profile is shown in figure 4.9a and the less statistically accurate 444 magnetic Compton profile is shown in figure 4.9b. Also shown in figures 4.9a and b is the theoretical prediction for the magnetic Compton profile of polycrystalline iron (Wakoh and Kubo, 1977) calculated by the APW method. For comparison with
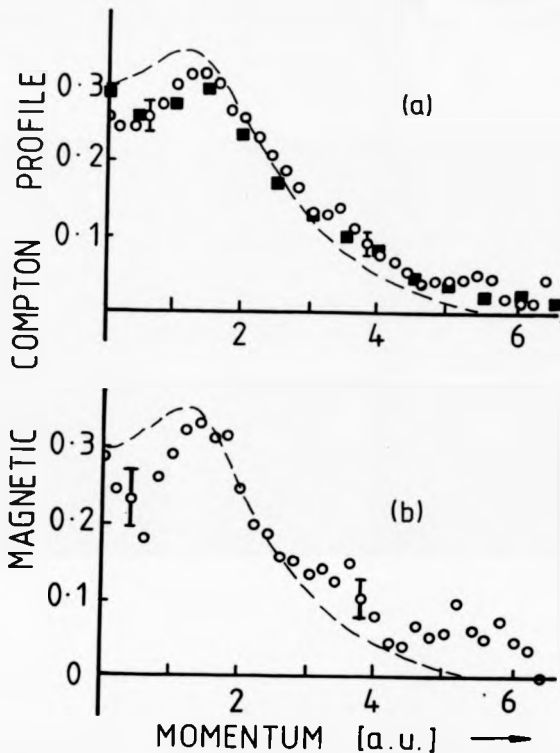
Figure 4.9 Processed data for (a) 333 and (b) 444 magnetic Compton profiles compared with the results of an APW calculation (Wakoh and Kubo, 1977). The band calculation has been convoluted with Gaussians of (a) 1.0a.u. and (b) 0.8a.u. FWHM before comparison with experiment. The present synchrotron data are shown as the open circles, the filled squares in (a) represent the radioisotope data of Sakai et al (1984) which were reported at the same resolution and similar statistical accuracy.

the experiment the theory has been convoluted with Gaussians of FWHM which match the experimental resolution. The statistical error per 0.2a.u. momentum interval is $\pm 8\frac{1}{2}\% J_{mag}(0)$ which is one quarter of the predicted dip. This accuracy was sufficient to establish, for the first time in a photon scattering experiment, the lineshape of the magnetic Compton profile of iron and to verify the existence of a central dip in the magnetic Compton profile. The achievements of magnetic Compton studies performed prior to this study are summarised in table 4.2. In particular this table emphasises the difficulty in obtaining statistical accuracy in $J_{mag}(p_z)$.

The statistical accuracy of $J_{mag}(p_z)$ is dependent upon the error in the total profiles (i.e. $J_{\uparrow}(p_z)$ and $J_{\downarrow}(p_z)$) and the size of the magnetic effect such that to halve the error in $J_{mag}(p_z)$ requires either the counting time to be quadrupled or the magnetic effect to doubled. In turn, the size of the magnetic effect is dependent upon ω_1 and P_2. For CPSR obtained by the inclined view method the intensity, ω_1 and P_2 are also dependent upon one another and must be optimised to achieve the minimum error in $J_{mag}(p_z)$.

Preliminary optimisation measurements of the beam intensity and the size of the magnetic effect were not possible in this study due to the limited scheduled user beam. In the absence of these measurements the experiment was performed as far off the orbital axis as possible (i.e. maximise P_2), without too great a loss in measured intensity (approximately two orders loss in intensity compared with the orbital intensity was considered tolerable).

4.5   Discussion.

The band structure of ferromagnetic iron was calculated by Wakoh and Yamishita in 1966 and the theoretical results were found to be in satisfactory agreement with experimental results for the electronic specific heat, the magnetoresistance, de Haas-van Alphen effect and the scattering form factors. In a later publication (Wakoh and Kubo, 1977) the spin dependent Compton profiles and positron annihilation angular distributions were calculated by the APW method for ferromagnetic iron. These calculations were performed to encourage Compton and positron studies which have the ability to test the calculated band structure over the

Reference	P_2	$I_\uparrow - I_\downarrow$	t/hours	ω_1/keV	% error in $J_{mag}(0)$	% effect	int. a.u.
Sakai,Ono 1976	0.3	8×10^4	139	122.0	±28%	—	0.5
Sakai et al 1983	0.8	6×10^5	165	129.0	±10%	2.59%	0.5
Holt et al 1986	0.5	1.5×10^4	8	33.7	±40%	~1%	0.5
Cooper et al 1986	0.6	3.6×10^5	16	46.4	±4%	~1%	0.5

Table 4.2 Magnetic Compton studies of polycrystalline iron upto 1986.

complete extent of the occupied regions. The same APW technique was used as that employed by Wakoh and his co-workers to calculate Compton profiles and positron annihilation profiles for several of the transition metals, with the exception that a spin dependent potential was used to describe the effect of exchange on the spin distribution. The electron wavefunctions were evaluated for each spin state at 55 k-points in the irreducible volume equivalent to $\frac{1}{48}^{th}$ of the Brillouin zone and the Compton profiles for each band were formed by summing over all the momentum space wavefunctions. The calculation was performed for a net magnetisation of 2.2 Bohr magnetons (μ_B).

The magnetic Compton profile of iron calculated by Wakoh and Kubo (1977) is shown in figure 4.10. The individual contributions from the d-, s/p hybrid and core electrons to the total magnetic Compton profile are represented in figure 4.10 by the dashed, dotted and dashed/dotted lines respectively. As the majority of the conduction electrons in transition metals reside in the 3-d orbitals it is expected, as figure 4.10 confirms, that these electrons will form the major constituent of the magnetic Compton profile. Closer examination reveals that there is a degree of negative polarisation associated with electrons in the s/p hybrid band which can be explained as follows. The polarisation of the s/p hybrid electrons arises via two interactions. Firstly, the exchange field splits the s/p hybrid producing a positive polarisation in the same direction as that produced in the d-band (see figure 4.11) and secondly according to Wakoh and Yamishita (1966) the s/d hybridisation 'pushes' the s/p electron energy states out of the occupied region as indicated by the arrows in figure 4.11. This produces a slightly larger polarisation in the opposite direction to that produced by the exchange splitting and results in a net negative polarisation. The solid line in figure 4.10 represents the total spherical averaged magnetic Compton profile of iron and it is clear that it is the negative polarisation of the s/p hybrid electrons which is responsible for the volcano like central dip in the profile. In real space this is manifest as a negative magnetisation density in the interatomic regions (see figure 4.12 taken from Schull and Mook,1966).

Both the 333 and 444 profiles verify the existence of the central dip and suggest that its depth is approximately twice that predicted by the APW model whilst its width is correctly predicted. As the depth of the dip is a measure of the negative spin polarisation of the s/p
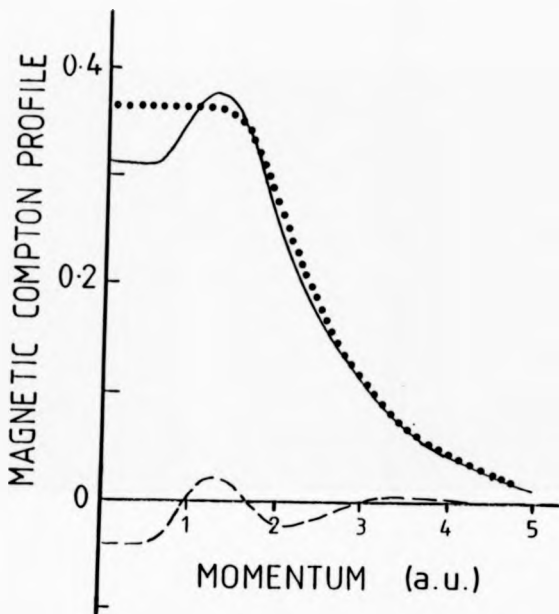
Figure 4.10 The partial contributions to the magnetic Compton profile of iron from the 3d (dotted line) and the s/p hybrid electrons (dashed line). The total distribution is represented by the solid line (from Wakoh and Kubo, 1977).
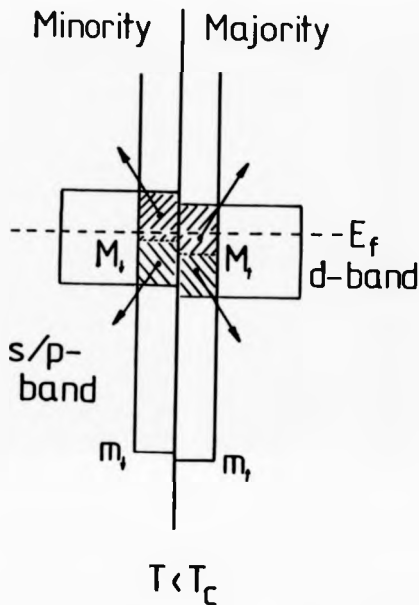
Figure 4.11 Schematic density of states curves for ferromagnetic iron below the Curie temperature, T_c. $m_{\downarrow}$ and $m_{\uparrow}$ denote the bottoms of the s-bands in the minority and majority states respectively. $M_{\downarrow}$ and $M_{\uparrow}$ denote the middle points of the d-bands and E_f denotes the Fermi level. If s-like components are pushed out of the d-bands as indicated by the arrows, the amount of s-like components in the majority band below E_f are reduced to the states from $m_{\uparrow}$ to $M_{\uparrow}$ and that in the minority band is reduced to those from $m_{\downarrow}$ and $M_{\downarrow}$ leaving a net negative magnetisation (from Wakoh and Kubo, 1977).
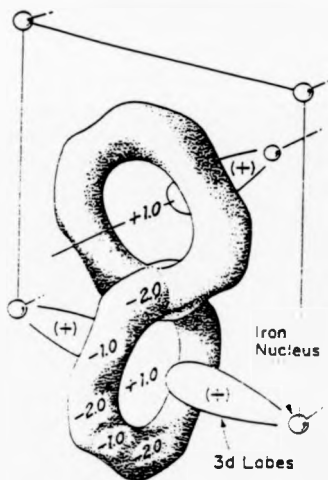
Magnetization in kilogauss

Figure 4.12 Model of the magnetization distribution in the bcc unit cell of Fe. The concentration of the very large, positive, 3d-shell magnetization along the cube edges is overemphasized to show its relationship to the negative magnetization rings in the interstitial regions (from Shull and Mook, 1966).

hybrid electrons. The discrepancy between the experiment and the theory can be explained by the APW model underestimating the contribution from the negatively polarised 4s-p band. The radioisotope data obtained by Sakai Terashima and Sakisawa (1984) has been left right averaged and displayed in figure 4.9a for comparison. The statistical accuracy of the radioisotope result is insufficient to characterise the central dip however it is interesting to note that all the experimental results show considerable extra electron density at high momentum ($p_z >$4a.u.) than the theory. Because this extra density occurs only at high momentum it can be attributed to more positively polarised d-electron components than predicted by the theory i.e. the d-electron contribution in figure 4.10 extends further out in momentum space than predicted. The momentum density is calculated from an expansion of eigenfunctions over what has to be a finite number of reciprocal lattice vectors. This results in the omission of some of the high momentum components of the d-electron wavefunctions. This disagreement between experiment and theory does not contradict the generally good agreement observed between the same band structure calculation (Wakoh and Yamishita, 1966) and spin polarised positron measurements by Mijnarends (1973) for the following reason. The positively charged positron is repelled by the positive ion core of the iron and therefore is less sensitive to the high momentum components of the wavefunction which are associated with this core.

4.6 Summary

These measurements were not limited by low photon fluxes as were the radioisotope experiments by Sakai and his co-workers and were at the time the most accurate magnetic Compton profile measurements. Experimental work at the SRS was interrupted soon after the results presented in this chapter were obtained for the installation of the high brightness magnetic lattice (HBL). In the months of down time that followed attention was directed to ways of obtaining better resolution and statistically accurate data with the ultimate aim of obtaining directional magnetic Compton profiles. It has already been mentioned that this experiment was performed in an experimental environment designed primarily for x-ray topography in which only the on axis synchrotron beam is used. Finding the orbital position and the moving

each piece of apparatus off axis individually proved to be time consuming and cumbersome. It also prevented an accurate up-to-date check of the orbital position. To overcome these problems and to reduce the 'dead time', a table, movable in the vertical plane, on top of which was mounted all the experimental apparatus was designed and built. The design considerations of this piece of apparatus are discussed in the next chapter.

Chapter 5

A MAGNETIC COMPTON SPECTROMETER.

5.1 Introduction.

In July 1986 the SRS at Daresbury was shut down for the installation of a high brightness magnet lattice (HBL). Additional focusing magnets capable of reducing the source size were installed in the synchrotron ring. The consequence of this, was a reduction in the divergence of the emitted radiation and therefore an increase in the brightness of the source. (i.e. the photon flux per unit phase space volume, photons s^{-1} $mrad^{-2}$ mm^{-2} (0.1% bandwidth)$^{-1}$). The HBL is also responsible for a reduction in the emittance, ξ of the source, where ξ is defined as $\xi = \sigma_x \sigma_y \sigma_{x'} \sigma_{y'}, (mrad^2 mm^2)$. Where σ_x and $\sigma_{x'}$ are the positions and angles of trajectory of the electron beam in the horizontal plane and σ_y and $\sigma_{y'}$ correspond to the same quantities in the vertical plane. The electron beam under takes small oscillations within the source and these oscillations lead to a cancellation of CPSR of one hand emitted below the electron trajectory with CPSR of the opposite hand emitted from above the electron trajectory (see figure 5.1a). The reduction in ξ offered by the HBL reduces the severity of this cancellation and therefore the HBL is able to offer a brighter source of radiation with a higher degree of circular polarisation at a given flux. This is confirmed in figure 5.1b where P_2 is plotted as a function of azimuthal angle, ψ for a source of zero emittance (solid line), the pre-HBL source (dashed line) and the post-HBL source (dotted line). The improvement in P_2 is particularly beneficial to magnetic Compton studies as the magnetic scattering cross section is directly proportional to P_2.

(a)

emittance, σ_y electron beam   orbital plane
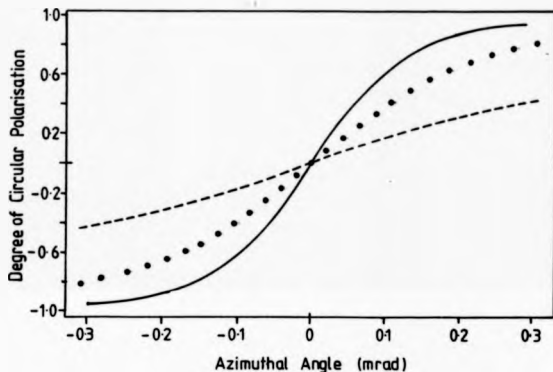
A   B
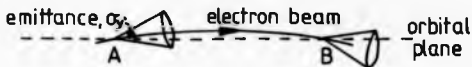
(b)

Figure 5.1 The effect of source emittance and the HBL on the degree of circular polarisation. (a) Vertical oscillations in the electron beam result in a cancellation of CPSR of one hand emitted below the electron trajectory (A) with CPSR of the opposite hand emitted above the electron trajectory (B). The reduction of the vertical emittance, σ_y, brought about by the HBL, reduces the severity of the polarisation cancellation. (b) The degree of circular polarisation as a function of azimuthal angle for a source of zero emittance (solid line), pre-HBL source (dashed line) and post-HBL source (dotted line).

The 12 month installation period of the HBL was used to review and improve the present experimental technique. The experimental environment in which the experiments were performed was designed primarily for x-ray topography for which only the intense 'on axis' synchrotron beam is required. In the past the orbital position was found by scanning the synchrotron beam vertically with a pin-hole mounted on a crude scissor jack behind which was placed an ionisation chamber. To extract CPSR each piece of apparatus had to be moved individually to the 'off axis' position. In the pre-HBL study much valuable user beam was wasted in moving and realigning the apparatus in this off axis position and checking the orbital position after each refill of the SRS.

To reduce this wasted time a table, movable vertically through the orbital position was designed and built and the entire experimental apparatus and radiation shielding was mounted on top it. In the next section the main criteria, aside from cost limitations, around which the new spectrometer was designed are discussed.

5.2 Optimisation of Experimental Parameters.

5.2.1 Azimuthal Angle, Energy and Flux.

In both the pre-HBL experiments performed on the SRS the azimuthal angle ψ was chosen to maximise the value of P_3 . The degree of circular polarisation, P_3 is a slowly increasing function of ψ whereas the intensity is a rapidly decreasing function of it (refer to figures 4.5a and 4.5b). To improve the signal/noise ratio a better strategy would be to minimize the fractional error in the magnetic Compton scattered intensity. This quantity is dependent upon the size of the magnetic effect, the energy employed and the scattered signal . The azimuthal angle required to optimise the experiment can be found by maximising the quantity defined as r where

$$r = \frac{\text{Magnetic signal}}{\text{Compton noise}} = \frac{\hbar\omega_1}{m_0 c^2} \frac{P_3 I}{\sqrt{I}} \propto P_3 \sqrt{I}. \tag{5.1}$$

I is either the total Compton intensity under the spin up ($I_\uparrow$) profile or the spin down profile ($I_\downarrow$) profile. The degree of CPSR is proportional to the size of the magnetic effect $\frac{I_\uparrow - I_\downarrow}{I_\uparrow}$ and

84

hence,

$$r \propto \frac{I_\parallel - I_\perp}{\sqrt{I_\parallel}} \tag{5.2}$$

The variation of r with ψ for various photon energies has been calculated for radiation received at station W9.4 (Laundy, private communication). The calculations are for the post-HBL status of the SRS. The x-ray flux from a source with zero emittance was calculated using expressions for the components of the intensity emitted parallel and perpendicular to the electron orbit derived by Kim (1986). To account for the finite emittance of the electron beam Laundy integrated the radiation distribution over all possible positions and directions of motion of the electrons traveling within a finite beam size. The horizontal emittance was assumed to be negligible and the positions and angles of trajectory in the vertical plane were assumed to have Gaussian distributions with standard deviations of σ_y and $\sigma_{y'}$ respectively. The values of σ_y and $\sigma_{y'}$ have been calculated for the post-HBL SRS wiggler by Mackay (1987) as $\sigma_y = 0.16$mm and $\sigma_{y'} = 0.06$mrad.

Station W9.4 is some 37m from the tangent point of the synchrotron ring and the angular divergence of 0.06mrad corresponds to a projected beam height at the station of ~2.2mm. Therefore in this case the divergence of the electron beam dominates over the actual source size of 0.16mm. The azimuthal dependence of P_3 was calculated from the polarisation density matrix D which is given by equation 1.25 and finally r was evaluated using equation 5.1. Due to the oblique scattering angles chosen for these studies the effective sample thickness t_{eff} may be assumed to be infinite, i.e. for $\phi = 150°$, $t_{eff} = 6$mm $\gg \frac{1}{\mu_{Fe(60keV)}}$, where $\mu_{Fe(60keV)} = 9.2$cm^{-1} is the absorption coefficient of iron at 60keV. If X represents the scattering from a small element dx a distance x into the sample, the total scattering is proportional to $\int_0^{t_{eff}} X e^{-\mu x} dx = \frac{X}{\mu}$ for $t_{eff} \to \infty$. Thus the energy dependence of absorption in the sample is included by forming $r' = \frac{r}{\mu}$.

The theoretical predictions for the ψ dependence of r' (the figure of merit)for photon energies of 40, 50, 60, 70, 80 and 100 keV for station W9.4 are shown in figure 5.2a. According to this figure the optimum energy for studies on iron is between 55–60keV and the experiment should be performed with CPSR extracted at an angle of ~0.14mrad to the orbital plane.
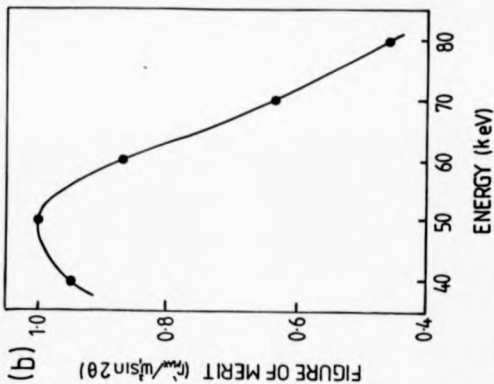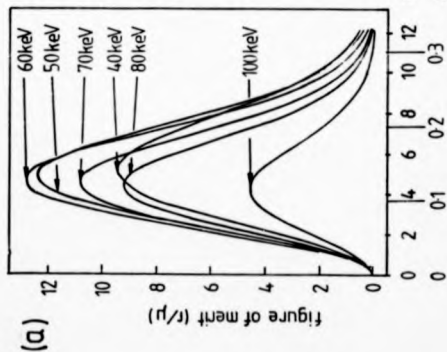
Figure 5.2 (a) The figure of merit, r^* calculated by Laundy (private communication) for photon energies between 40keV and 100keV as a function of azimuthal angle. According to the calculation, the experiment should be performed with a photon beam of energy 55-60keV extracted 6mm (0.14mrad) above the orbital plane. (b) Including the reflectivity as $R \propto \frac{1}{q^2 \sin 2\theta}$ reduces the optimum energy to ~50keV for the 333 reflection.
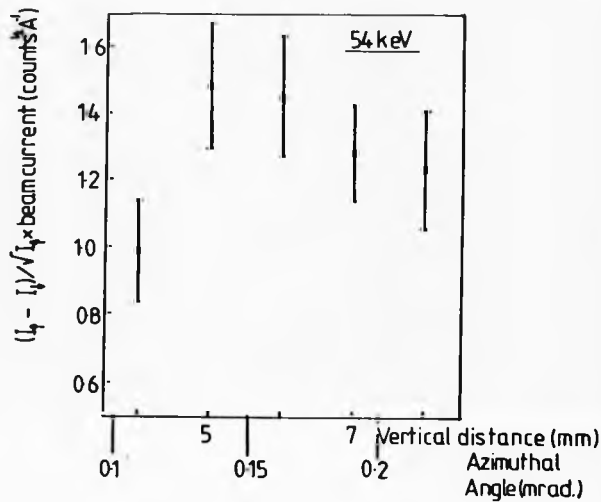
Figure 5.3 The experimental figure of merit for an incident energy of 54keV. Each data point has been divided by the SRS beam current.

This calculation does not entirely reproduce the true experimental situation because it does not account for the energy dependence of the reflectivity, R of the monochromator. For a large perfect crystal this is $R \propto \frac{1}{\sqrt{\epsilon} \sin 2\theta}$ (see Matsushita and Hashitsume, 1983). For the 333 Ge reflection the inclusion of this factor reduces the optimum energy to around 50keV, see figure 5.2b. Here the figure of merit is given by $\frac{r'_{max}}{\sqrt{\epsilon} \sin 2\theta}$, where r'_{max} are the maximum values of r' in figure 5.2a. The curve is normalised to unity at ω_1=50keV. No account was taken for the finite vertical size of the synchrotron beam. Experimentally a vertical beam size in the range 3–5mm is chosen depending upon the sample size.

Using a vertical beam size of 5mm, $I_\uparrow$ and $I_\downarrow$ were obtained by integrating the respective Compton signals recorded by the MCA for various elevations of the sample slits above the orbital plane. In figure 5.3 the experimental ψ dependence of r' is shown for ω_1=54keV. Each data point corresponds to the azimuthal angle of the centre of the sample slits. The total intensity obtained by sampling a 5mm vertical slice of the beam will be the integrated value for all photons emitted within the angular range dictated by the slit size, whilst the degree of CPSR will be the weighted average value of P_2, i.e. $\frac{\int I(\psi) P_2(\psi) d\psi}{\int I(\psi) d\psi}$. Despite the poor statistical accuracy of this 'quick' preliminary measurement figure 5.3 indicates that the optimum azimuthal angle for the present study was within the range 0.14–0.16mrad, i.e. a vertical displacement of 6mm at the station. This is in line with the theoretical prediction by Laundy of $\sim$0.14mrad ($\sim$6mm). For these measurements the new spectrometer must be capable of obtaining photon energies in the range 40–80keV and of displacing the entire apparatus vertically in the range -10mm to 10mm with an accuracy of ±0.1mm.

5.2.2 The Case for Horizontal Dispersion.

The responsibility for the poor resolution of the pre-HBL results may be attributed, in part, to the poor quality of the solid state detector supplied by Daresbury laboratory (FWHM>450eV @ 60keV). To overcome this problem this detector was exchanged for a new higher resolution solid state detector (FWHM=360eV @ 60keV). This detector was coupled to a large 30 litre liquid nitrogen dewar. This large dewar was deemed necessary to avoid frequent refilling, a process which degrades the resolution of the detector for some time after filling (upto 90

minutes). Unlike the vertical scattering geometry used in the pre-HBL study, this detector is suited for operation in the horizontal plane. Fortunately, there is a small advantage in choosing a horizontal scattering geometry. The radiation extracted off axis is elliptically polarised with the intensity of the parallel component larger than the intensity of the corresponding perpendicular component (refer to figure 4.5a in the previous chapter). Diffraction in the horizontal plane reduces the intensity of the larger horizontal component by a factor $\cos 2\theta$ producing a larger degree of circular polarisation than a vertical scattering geometry where the situation is reversed. As the Bragg angles employed in these studies are small ($2\theta \sim 10°$) the improvement in P_3 is only a few percent. For example, with $\theta = 5.4°$ (333 Ge reflection), $\omega_1 = 60$keV, a vertical scattering geometry would yield $P_3 = 0.66$, whilst the horizontal situation would yield $P_3 = 0.68$ and an improvement in the signal/noise ratio r (equation 5.1) of $\sim 1\%$. In principle it should be possible to obtain $P_3 = 1$ by multiple reflections although in practice at these high energies more than 100 reflections would be required.

5.2.3 Geometrical Broadening.

As in γ-ray Compton studies (see chapter 2), the final momentum resolution of the data, Δp_{tot} is the combination of the geometrical resolution of the spectrometer, Δp_{geom} and the detector resolution, Δp_{det} such that $\Delta p_{tot}^2 = \Delta p_{geom}^2 + \Delta p_{det}^2$. In order to preserve the inherent resolution of the new solid state detector (i.e. $\Delta p_{det} = 0.57a.u.$ for $\omega_1 = 60$keV) and simultaneously maximise the detected count rate, the optimum detector solid angle must be calculated. For an angular variation $\Delta\theta$, which leads to an energy spread $\Delta\omega_2$, the momentum resolution of the spectrometer is given by,

$$\Delta p_{geom} = \frac{\partial p_{geom}}{\partial \omega_2} \Delta\omega_2 + \frac{\partial p_{geom}}{\partial \phi} \Delta\phi. \tag{5.3}$$

For $\omega_1 \sim \omega_2$ and $\cos\phi \sim -1$ the relationship between energy and momentum, equation 1.20 leads to the following expressions,

$$\frac{\partial p_{geom}}{\partial \omega_2} = \frac{mc\omega_1}{2mc^2} \sin\phi \tag{5.4}$$

$$\frac{\partial p_{geom}}{\delta \phi} = \frac{mc}{2\omega_1}. \tag{5.5}$$

Now, $\Delta \omega_2 = \frac{\partial \omega_2}{\delta \phi} \Delta \phi$ and from Compton shift relationship, equation 1.1

$$\frac{\delta \omega_2}{\delta \phi} = \frac{\omega_1^2 \sin \phi}{mc^2}. \tag{5.6}$$

Therefore,

$$\Delta p_{geom} = \frac{3}{4} \frac{mc}{mc^2} \omega_1 \sin \phi \Delta \phi. \tag{5.7}$$

For the small angular variations involved $\Delta \phi \sim \frac{d}{l}$, where d is the size of the detector crystal and/or the detector collimator and l is the sample detector distance, therefore

$$\Delta p_{geom} = \frac{3}{4} \frac{mc\omega_1 \sin \phi}{mc^2} \frac{d}{l} \tag{5.8}$$

In table 5.1 Δp_{geom} is given as a function of l for the situation where $d=10$mm , $\omega_1=60$keV and $\phi=150°$. Also given in table 5.1 is combined momentum resolution, Δp_{tot}. From the figures in table 5.1, a sample-detector distance of 250mm appears to offer a satisfactory momentum resolution, (0.75a.u.) and would result in approximately a 30% increase in the detected signal over the pre-HBL study where $l \sim 300$mm.

In conclusion, in the design of the spectrometer careful consideration should be given to the degree of scattered beam collimation and to the scattered beam path length. The result will be an improvement in both the detected signal and in the resolution of the experiment.

5.2.4 Scattering Angle and Beam Dimensions.

The magnetic Compton scattering cross section and the ratio $\frac{d\sigma_m}{d\sigma_c}$ attain their respective maxima as the scattering angle, ϕ approaches 180° (refer to figures 1.5a and 1.6). In addition equation 5.8 suggest that the geometrical resolution of the spectrometer is smallest for high scattering angles. However, if the optimum detector sample separation ($\sim$ 250mm) is to be retained, the maximum scattering angle obtainable is 150°. The reason for this restriction is indicated by the schematic diagram shown in figure 5.4a. This figure suggests that any

l/mm	Δp_{geom}/a.u.	Δp_{tot}/a.u.
100	1.20	1.33
150	0.80	0.98
200	0.60	0.83
250	0.48	0.75
300	0.40	0.70

Table 5.1 Optimisation of sample detector separation, l. Δp_{geom} is the geometrical resolution calculated from equation 5.8 with ω_1=60keV, d=10mm and $\phi = 150°$. Δp_{tot} is the combination of the detector resolution, Δp_{det} plus the geometrical resolution for ω_1=60keV i.e. $\Delta p_{tot}^2 = \Delta p_{geom}^2 + \Delta p_{det}^2$, where Δp_{det}=0.57a.u..

further increase in ϕ beyond $\sim 150°$ will result in the intersection of the monochromated beam by the large detector dewar.

Future studies employing small single crystal samples necessitate the pole gap of the electromagnet to be limited to ~ 23mm (see chapter 6). To eliminate the possibility of magnetic scattering from the pole pieces of the electromagnet, it is necessary to include a few mm safety margin of unilluminated sample at each pole piece. The result is an effective scattering area of 20mm horizontally × 10mm vertically.

To extract the electron momentum density distribution of the unpaired spins from the scattering cross section, equation 1.47, k_1 must be aligned anti/parallel to the direction of the electron spins and the applied field. In practice this is not possible and k_1 is aligned at a small angle η to the sample face thereby diminishing the magnetic cross section by a factor $\cos \eta$. Fortunately, as long as η is small ($< 20°$) there is no significant reduction to the scattered intensity. However as η is reduced, the horizontal 'footprint' of the photon beam on the sample becomes enlarged such that for $\eta = 20°$, the maximum acceptable horizontal beam dimension is $h \sim 7$mm (see figure 5.4b). Furthermore, if CPSR is to be extracted primarily at the optimum azimuthal angle, the vertical beam size, v must be limited to ~ 5mm, i.e. a ψ range of 0.135mrad as indicated by the cross hatched area in figure 5.5) In conclusion, the proposed experimental arrangement dictates the beam size to be $v = 5$mm × $h = 7$mm, and the angles ϕ, η to be $150°$ and $\sim 20°$ respectively.

5.2.5 Bragg Angle.

The experimental optimisation dictates the need for a high intensity, high energy, monochromatic photon beam (see section 5.2.1). This can be achieved by employing a low order monochromator reflection (the reflecting power is strongest for principle reflections) and a small Bragg angle, θ (see table 5.2). At small θ, a long monochromator is necessary if a photon beam with a substantial horizontal width (i.e. $h \sim 7$mm) is to be accommodated.

Two differently oriented Ge monochromators (the choice of monochromator material was discussed in chapter 4 were available, the 111 crystal used in the previous study and a new 220 crystal. Both monochromators were of similar dimensions, namely 80mm long, 25mm
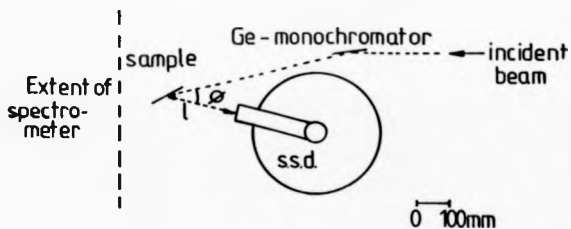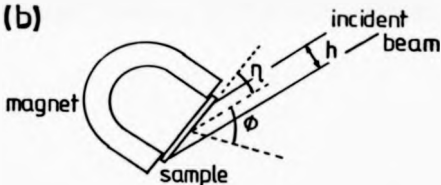
Figure 8.4 Optimisation of scattering angle and the horizontal beam dimension. (a) conflict between the scattering angle, ϕ and the optimum sample detector separation, l. (b) $\phi = 150°, \eta = 20°$ and a scattering area of maximum length 20mm implies a horizontal beam dimension of $h-7$mm.
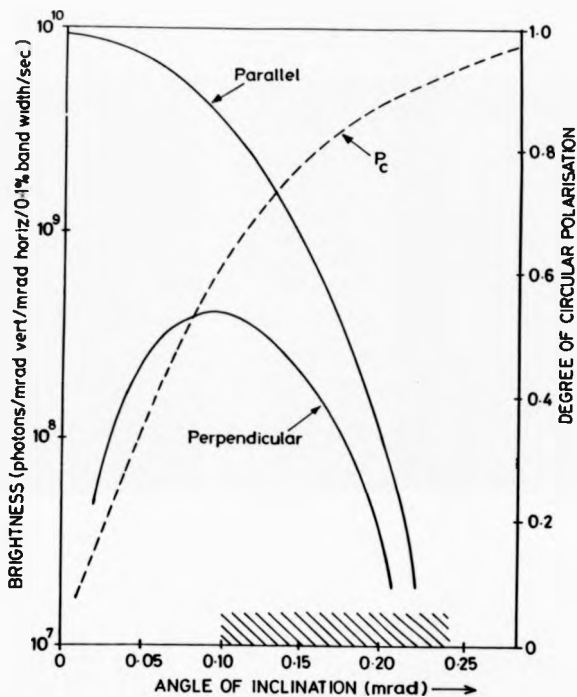
Figure 5.5 Vertical beam dimension. If CPSR is to be extracted primarily at the optimum azimuthal angle of 0.14mrad, the vertical acceptance of radiation must be limited to the azimuthal range indicated by the cross hatched area. This implies a 8mm high beam.

Reflection hkl	Bragg angle/°	R	h/mm	hR
111	1.82	1	2.54	2.54
220	2.97	0.74	4.14	3.08
333	5.46	0.17	7.62	1.29
440	5.94	0.21	8.28	1.74

Table 5.2 Assessment of the available Ge(111) and Ge (220) monochromators at $\omega_1 = 60$keV. The reflecting power, R has been normalised to unity for the 111 refelction (origional values of R from Matsushita and Hashizume, 1983). The values of h given above are for a monochromator of length 80mm i.e. $h = 80 \sin \theta$ and the quantity hR is proportional to the flux of the monochromated beam.

wide and 2mm thick. Also given in table 5.2 are the maximum values of h which can be accommodated by each crystal when tuned to select an energy of 60keV with the 111, 220, 333 and 440 reflections. The flux of the monochromated beam is proportional to hR where R is the reflecting power of monochromating Bragg reflection. This quantity has been calculated for the reflections listed in table 5.2 and is included in the last column.

Unlike the 333 reflection used in the pre-HBL study, there is no subharmonic of the 220 reflection. This is a great advantage in view of the fact that the pre-HBL study was limited to low Compton count rates by the risk of dead time problems caused by the high flux of low energy photons entering the detector ($\omega_1 < 15$keV). These 'unwanted' low energy photons arose primarily from the 111 subharmonic reflection. It is apparent from this fact and the information given in table 5.2, that the 220 reflection is best suited for the proposed experimental arrangement.

5.3 The Design and Construction of the Spectrometer.

User beam time for magnetic Compton studies is usually allocated in short, 5-8 day sessions. For this reason the new spectrometer had to be installed quickly onto the existing topography camera situated in the experimental hutch. The basic design adopted for the spectrometer is illustrated in figure 5.6 and consists of three coupled aluminium alloy plates. The bottom plate serves only as a base for the jacking mechanism which is fixed to the load bearing middle plate. The entire apparatus is mounted to the top plate which is connected to the middle plate by seven strong struts. The detector is positioned in the recess of the middle plate and can be jacked in unison with the monochromator, sample, etc. through the orbital position. The main components of the spectrometer i.e. the lifting mechanism, the top plate design, the collimation and shielding employed and the modified electromagnet are now described in detail.

Figure 5.6 Illustration of the basic design adopted for the magnetic Compton spectrometer.

5.3.1 Lifting apparatus.

The main contributions to the weight of the spectrometer are the detector (>40kg when full), sample slits, the aluminium plates which make up the spectrometer (~400kg) and the copious lead shielding. The total weight of the components was estimated to be approximately 750kg, unevenly distributed about the middle plate. Two different types of jacking system were considered : firstly a system containing one or two scissor jacks and secondly a system incorporating a series of vertical screw jacks. Either type would be fixed to the $\frac{1}{2}$″ thick base plate and raise the rest of the spectrometer with respect to this base.

Scissor jacks are inherently geared and relatively cheap compared to a system of screw jacks, particularly as the screw jacks require a separate gearing system. However because the weight would be unevenly distributed one scissor jack would prove unstable and a multi-scissor jack system would be difficult to level. One further limitation on the design was imposed by the height of the detector. Given that the topography base plate is fixed, it is necessary for the middle and base plates of the spectrometer to close together if the detector is to be accommodated below the orbital plane and an experiment performed with CPSR of the opposite hand. This is only possible with a system of vertical screw jacks mounted one in each corner of the middle plate and operating through it, as illustrated in figure 5.6. In addition this would provide a stable system capable of lifting uneven heavy weights provided it was geared properly.

Four $\frac{1}{2}$ tonne vertical screw jacks capable of a vertical displacement of 100mm were chosen and coupled together with a system of universal couplings, mild steel connecting rods and a gear box. The gearing was provided by two worm reduction gear boxes (see figure 5.7 for a schematic representation of the lifting system). The middle plate can easily be raised or lowered by virtue of a handle mounted at the front of the spectrometer and the gearing is such (1 turn=0.1mm) that a stepper motor could be incorporated to drive the jacks if required. With jacks fully closed the detector head is ~20mm below the orbital plane and ~60mm above when they are fully extended. These distances correspond to azimuthal angles in the range 0.54mrad below to 1.62mrad above the orbital plane and comfortably cover the
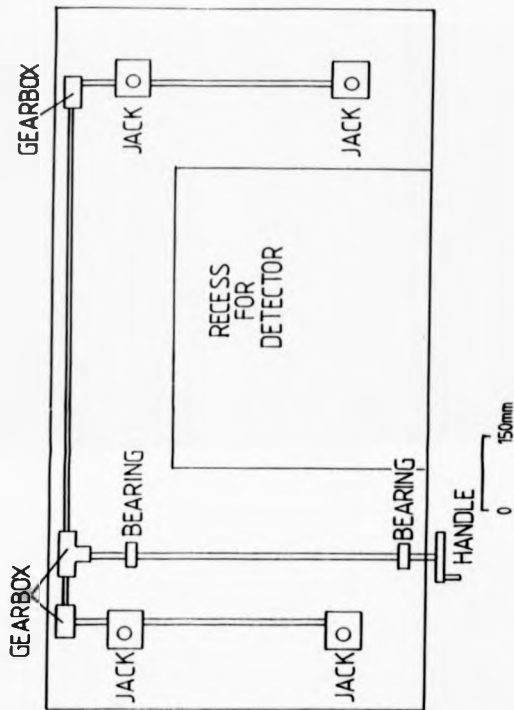
Figure 5.7 Schematic diagram of the lifting mechanism showing the positioning of the 4 vertical screw jacks and the gear boxes.

optimum angle of ~0.14mrad.

5.3.2 Top Plate Design.

The layout of the experimental work area or top plate is shown schematically in figure 5.8. The top plate consists of a $\frac{1}{2}$" thick, machined aluminium alloy plate mounted to the movable middle plate by 7 supporting struts or legs. It was shaped to accommodate the detector dewar. The sample slits (supplied by Daresbury laboratory) are comprised of two pairs of tungsten slits which move with respect to a fixed , common centre point . As it was necessary to retain these slits a 500mm section of X95 optical bench compatible with the mounting bracket of the sample slits was fixed onto the top plate. This optical bench was also useful for mounting an ionisation chamber and various pieces of lead shielding.

The monochromator holder is attached to a goniometer which in turn is mounted to a vertical stand. The goniometer is used to define the Bragg angle and to ensure the monochromator is vertical. As in γ-ray Compton studies the exact value of ω_1 is arbitrary and once chosen ω_1 is unaltered throughout the experiment. Hence a motor driven monochromator is unnecessary and the Bragg angle, θ is set by hand. The monochromator holder is constructed of brass and is shielded with lead to remove spurious reflections and reduce stray radiation. The radiation is diffracted at an angle of 2θ to the centre line of the X95 optical bench. The magnet and sample are positioned on a movable arm (marked as 'A' in figure 5.8) which pivots about a point directly below the mid point of the monochromator face. This arm is set to the required 2θ with the aid of an angular scale marked in $2°$ increments on the top plate. Zero is the centre line of the X95 optical bench. To enable the various slits and brackets supplied by Daresbury Laboratory to be used a small section of a suitable optical mount is fixed to the arm. In addition a scale defining the scattering angle of the spectrometer is fitted to this arm.

The magnet is attached to an angular table which was used to define the angle between the k_1 and the applied magnetic field. In later experiments performed with single crystal samples knowledge of this angle was essential to align K along a specific crystallographic direction (refer to chapter 6). To ensure a reasonable separation of the straight though and diffracted
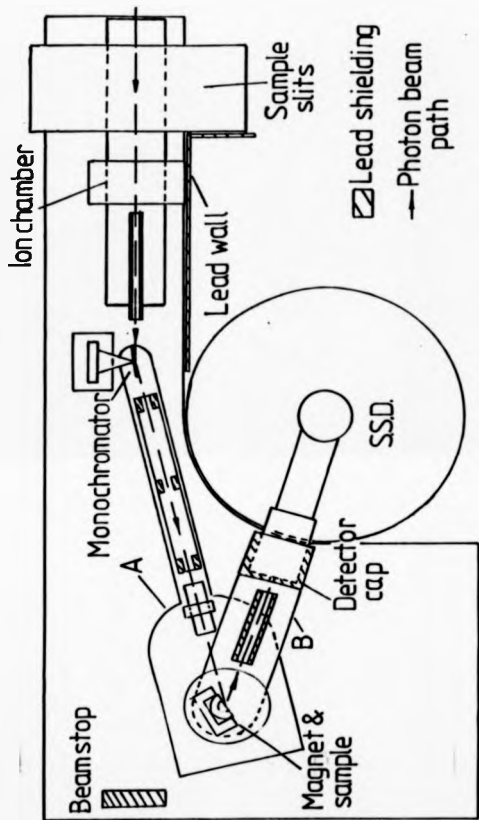
Figure 5.8 Schematic layout of the top plate of the spectrometer. The ion chamber and the motorised slits were supplied by Daresbury Laboratory. The function of the movable arms A and B are described in the text.

beams (~100mm for $2\theta=10.614°$ and $\omega_1=60$keV) the monochromator sample distance can be altered to suit the particular scattering geometry. The sample detector arm (marked as 'B' in figure 5.8) pivots about the centre of the angular table on a boss fixed through the other arm. The point of rotation is directly below the mid point of the sample face.

5.3.3 Radiation Shielding and Scattered Beam Collimation.

To reduce the background present in the pre-HBL spectra, only radiation which has been Compton scattered from the sample should be allowed to reach the detector. Although the photon flux diminishes rapidly with increasing energy a small percentage (< 0.1%) of the beam consists of very high energy photons ($\omega_1 > 100$keV). These photons are responsible for the significant amount of 'stray' radiation present in the hutch. In an attempt to reduce this scatter copious lead shielding is employed. In particular lead is placed around the sample slits to reduce the large amounts of x-ray flouresence created by radiation striking the slits. Lead shielding is also wrapped around the entire detector head, including the back of the head and the monochromator is also heavily shielded. The monochromated beam passes through a brass tube 500mm in diameter, inside of which is positioned 3 lead rings of internal diameter 25mm. These lead inserts serve to reduce small angle scattering and help to remove unwanted monochromator reflections. A set of finely adjusted tungsten slits are positioned just prior to the sample (see figure 5.8) and ensure only the required Bragg reflection (i.e. 111, 333 etc.) reach the sample.

The lead wall indicated in figure 5.8 is fitted with a lead roof 5mm thick which covers all the apparatus except the sample and the detector. Scatter from the straight through beam is reduced by a lead beam stop positioned at the end of the spectrometer. The large amounts of low energy (<10keV) radiation present in the synchrotron beam is reduced by a series of aluminium filters totalling 2mm in thickness which are placed prior to the sample slits. These filters remove the low energy radiation (e.g. I/I_0 @ 20keV$=15$%) but transmit the high energy photons required for the experiment (e.g. I/I_0 @ 60keV$=86$%). If the 333 reflection is employed, similar filtering of the scattered beam is necessary to reduce the significant number of low energy photons arising from the 111 sub-harmonic reflection.

The scattered beam is crudely collimated by a lead tube fixed to the optical mount on the sample-detector arm and accurately collimated by a tailor made cap which is fitted over the detector head. From the inside the cap consists of 1mm of aluminium followed by 3mm of brass then 2mm of lead and finally an outer protective brass cover 5mm thick. The lead absorbs most of the radiation striking it (e.g. I/I_0 @ 50keV$=10^{-8}$) and any l-shell fluorescence (energy $\sim$11keV) is completely absorbed by the copper and zinc in the brass. The x-ray fluorescence from the brass (8–9keV) is absorbed by the aluminium (e.g. I/I_0@ 8keV$=10^{-6}$). The scattered beam enters the detector crystal, which is 10mm behind the front of the cap through a circular hole cut in the end of the cap. The hole is the same diameter as the detector crystal i.e. 10mm .

5.3.4 Magnet and Magnet holder.

The magnet used in the previous study was exchanged for a smaller but similar horse shoe electromagnet, pole gap =23mm compared with 70mm for the former. This was necessary because future directional studies will require single crystal samples. These crystals can only be obtained in limited sizes. The pole pieces of the magnet are ground flat to ensure a good contact and hence minimize flux leakage. The number of turns of the electromagnet was been increased from 800 to 1200 turns of the same gauge wire. The field produced at the surface of this magnet was measured to be $\sim$ 0.6T, which is more than sufficient to saturate any of the ferromagnets to be studied (saturation fields for polycrystalline materials at room temperature, Fe=0.171T and Co=0.140T, values taken from Kittel chapt.15, 1976). The magnet is mounted in an aluminium cradle which is fixed to a circular plate by two brass struts.

5.4 Experimental Method.

Figure 5.9 is an illustration of the spectrometer, in situ, but with most of the lead shielding removed. The magnet and magnet holder are shown in an earlier illustration (see figure 5.6) Once positioned on the topography camera the spectrometer was aligned such that the centre

Figure 8.9 Illustration of the magnetic spectrometer positioned on the topography camera. The lead shielding has been removed for the purpose of this illustration.

line of the X95 optical bench (i.e. the spectrometer axis) was common to the synchrotron orbital plane. This was accomplished using a pre-aligned laser beam pointing at the tangent point. The laser was also used to position the sample slits, sample, monochromator, detector and various collimators at the correct height. The same plane Ge 111 monochromator used in the pre-HBL study was also used for this study. The Bragg angle of this monochromator was zeroed with the aid of the laser beam.

Rolled foil samples of Fe and Co were obtained from Goodfellow Metals with dimensions $50mm \times 25mm \times 1.5mm$ and $50mm \times 25mm \times 0.7mm$ respectively. The samples were checked for preferred orientation by the Laué method and in both samples none was detected. This check was omitted in the pre-HBL study of iron and because the magnetic Compton profile anisotropies are large (up to $40\%J(0)$ in the 111 direction , refer to figure 6.4) it is possible that the over estimation of the negative magnetisation contribution suggested by the experimental data could have been caused by a chance alignment of the scattering vector with a 111 preferred direction.

The large detector dewar was filled before the experiment and allowed to stabilise over night. The MCA was calibrated with the aid of a small $10\mu Ci$ ^{241}Am source. The high detected count rates of this experiment (typically 400cps compared to 0.5cps for a γ-ray experiment) result in large dead times in the ADC (analogue to digital converter) of the MCA. These were alleviated by reducing the shaping time of the detector amplifier from the $6\mu s$ normally used in γ-ray Compton studies to $2\mu s$. This reduced the dead time of the ADC to an acceptable level ($<4\%$ dead time) but at the expense of a small ($<30eV$) degradation in energy resolution of the detector.

The orbital position (i.e. the position of maximum intensity) was found by monitoring the intensity of the monochromated photon beam as a function of the elevation of the table and the measured intensities were normalised by division by the SRS beam current. This technique for finding the orbital plane was possible with the new spectrometer because now the whole apparatus can be quickly moved simultaneously through the orbital plane. Employing this technique, the orbital position to be found to within $\pm 0.25mm$ (see figure 5.10). There was a tendency for the orbital position to shift by up to 1.5mm after a machine refill and to ensure
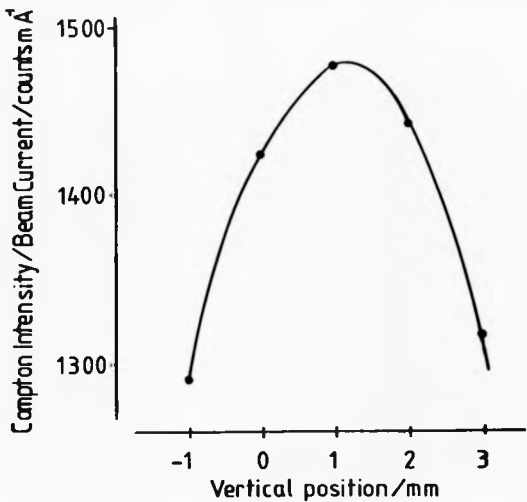
Figure 5.10 Location of the orbital position. The orbital position was relocated after each machine refill. This figure indicates the orbital position has moved up by ~1mm from its position at the start of the experiment.

the optimum position was always retained the orbital position was relocated after each refill.

A Bragg angle of ∼ 6° was set to select a photon energy in the region of 55keV with the 333 reflection. A beam of dimensions 5mm vertical, 7mm horizontal were chosen by adjustment of the sample slits. X-ray sensitive polaroid film was used to ensure the magnet was not viewed by the monochromated beam. After an initial on axis experiment which, as in the pre-HBL experiment, produced a null result, the spectrometer was jacked up until the centre of the sample slits was at the optimum position of 6mm (0.16mrad) above the orbital plane. With this vertical aperture circularly polarised photons with azimuthal angles in the range 0.09mrad< ψ <0.23mrad were selected by the sample slits. This implies a degree of circular polarisation of ∼0.57% (see figure 5.1b). The magnetisation direction was aligned as close as possible to k_1 which resulted in a scattering angle of 150°. The saturation magnetic field was obtained by passing a current of 1A through the new electromagnet. The data storage and switching of the magnetic field were controlled by the same computerised system developed for the pre-HBL study, (see Holt et al, 1986).

5.5   Results and Discussion.

5.5.1   Assessment of the New Spectrometer and the Effect of the HBL.

The results reported were obtained immediately after the recommissioning of the SRS. The poor lifetimes (<6 hours), small beam currents (injected at ∼80mA dumped at ∼30mA) and general instability of the electron beam made measurements difficult. Despite the difficulties ∼ 10^7 counts were accumulated in a typical 6 hour run under each of the spin up and spin down profiles. This is the same as that obtained in the pre-HBL study where the beam currents and lifetimes were much more favourable (see table 5.3). In addition the Ge 333 reflection was tuned to 54keV, almost 6keV higher in energy than the pre-HBL study. This move to higher photon energies imposed a flux penalty of ∼50% which arose from the strong energy dependence of the synchrotron flux (see figure 5.11). In addition the smaller Bragg angle required reduced the effective reflecting area of the monochromator by ∼ 15%. Table 5.3 indicates that despite the flux penalties it is advantageous to perform the experiment

Experimental parameter	Pre-HBL value	Post-HBL value	Approximate flux penalty (< 1), reward (> 1)
Electron beam current and source lifetime	upto 350mA 9–10 hours	<80mA ~6hours	0.125
Photon energy (333 reflection)	46.4keV	54.0kev	0.66
Bragg angle	7.1°	6.1°	0.85
Photoelectric absorption	2.2gcm^{-3}	1.37gcm^{-3}	1.50
P_2	0.38	0.57	1.50
Average viewing angle	0.24mrad (~ 9mm)	0.16mrad (~6mm)	5.00
$\frac{q_0}{\text{...}}$	0.09	0.10(5)	1.15
refectivity of monochromator $\propto \frac{1}{w_o^2 \sin 2\theta}$	–	–	0.85
sample detector separation	300mm	260mm	1.30

Table 8.3 Comparison of experimental parameters employed in the pre- and post-HBL studies. The approximate flux penalties or rewards associated with changes from the pre- to post-HBL arrangement are also listed.
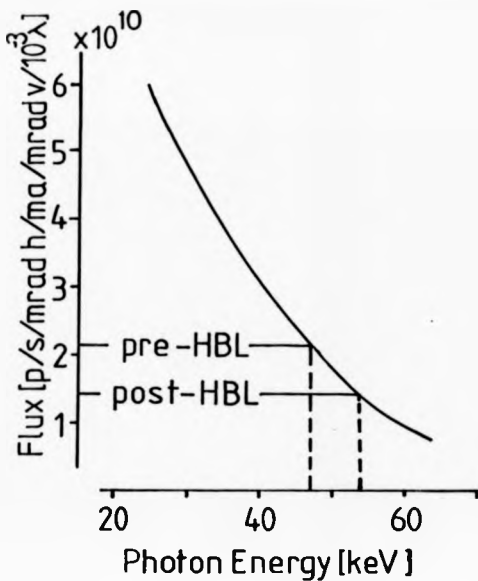
Figure 5.11 The variation of photon flux with energy over the range 20–60keV. The move from 44keV (pre-HBL) to 54keV (post-HBL) was accompanied by ~50% reduction in flux (adapted from figure 4 in Greaves et al, 1983).

with a higher incident energy (i.e. 54keV instead of 46keV used in pre-HBL study) for the following reasons; the detector resolution is improved ($\sim$10%), the magnetic Compton cross section is $\sim$15% larger and the photoelectric absorption in the sample is not so severe ($\sim$50% smaller).

It has already been mentioned (section 5.1) that the additional confinement of the electron beam results in a higher degree of CPSR at higher energies (for example ω_1=50keV P_2 is improved by $\sim$ 30% , see figure 5.1b). The consequence of this is that the optimum off axis position given by equation 5.1 was closer to the orbital plane and only a factor of 5 loss in flux was suffered in exchange for a photon beam with an average degree of circular polarisation of P_2=0.57, (value taken from figure 4.5a).

Totalling the flux penalties and rewards in table 5.3, it appears that, for the same geometrical configuration, the magnetic signal should be down on the pre-HBL study by approximately 75%. In fact the reduction of the sample to detector distance from $\sim$300mm (pre-HBL) to 260mm (post-HBL) restores the pre-HBL value. This reduction was made possible by optimising the amount of geometrical broadening which could be tolerated (see section 5.2.3). The momentum resolution of the 333 elastic line was Δp=0.8a.u. at 54keV and although there is still some degradation of the intrinsic resolution of the detector ($\Delta p = 0.6$a.u.) this is still an improvement over the pre-HBL study where $\Delta p \sim 1.0$a.u.. With this improvement in resolution and the relative increase in the detected signal all the main criteria around which the new spectrometer was designed have been achieved.

5.5.2 Magnetic Compton Profiles.

In a typical 6 hour run 1×10^7 counts were accumulated in the spin up and spin down profiles respectively. The data presented in this section relate to a total of 21 hours of useful beam for iron and 25 hours for cobalt. The energies of the 333 and 444 Ge reflections were 54.0keV and 71.9keV respectively. As the synchrotron flux diminishes so rapidly with increasing energy, the consequence of choosing to work with a slightly higher incident energy was that the intensity of the 444 reflection was reduced to $\frac{1}{5}$ the intensity of the 333 reflection compared to $\frac{1}{3}$ for the pre-HBL study.

As usual the spin up and spin down Compton profiles were corrected for the energy dependent scattering cross section and also for absorption of the beam in the sample. The difference profiles were evaluated and as in the previous study complete cancellation of the elastic and x-ray fluorescence lines was observed (see figure 5.12). The data sets should be identical except in the region of the magnetic Compton profiles, however figure 5.12 indicates small residual differences outside the region where magnetic effects are expected (i.e outside ±6keV of the profile peaks). As will now be explained these differences arise from two separate causes.

Firstly, higher energy circularly polarised photons selected by the high order reflections of the monochromator (i.e 444, 555 etc.) also undergo Compton scattering from the magnetised sample and result in additional magnetic Compton profiles at higher energies, (see chapter 4). Magnetic Compton profiles, like γ-ray Compton profiles, are 'contaminated' by the low energy tail of the detector response function (see section 2.6.4). This contamination is manifest as 'extra' momentum, primarily on the low energy side of $J_{mag}(p_z)$. As the magnetic scattering from the majority (spin up) band electrons exceeds that from the minority (spin down) band electrons, the degree of contamination to each profile will differ and be largest for $J_{\uparrow}(p_z)$. Therefore a residual magnetic contribution, which is largest on the low energy side of the profile, will remain on formation of the difference, $J_{\uparrow}(p_z) - J_{\downarrow}(p_z) = J_{mag}(p_z)$. The result is that the higher order magnetic Compton profiles (in particular the 444 profile) extend beneath the 333 magnetic profile and contribute to the observed magnetic background. Also, aside from coherent diffraction of the CPSR, incoherent scattering including Compton scattering from the monochromator is possible. This results in a small amount continuum CPSR, which in turn, also leads to a magnetic background in the difference profile.

The total spin dependent background is a smooth, almost linear, function of energy. The removal procedure was to fit first a straight line to the background of the total profile . This was then scaled accordingly and subtracted from the difference spectra. As $J_{mag}(0)$ is only $\sim \frac{1}{50}^{th} J(0)$, the size of the central dip was critically affected by this procedure and although the iron data obtained is statistically no improvement on the pre-HBL measurement they are felt to be more reliable.
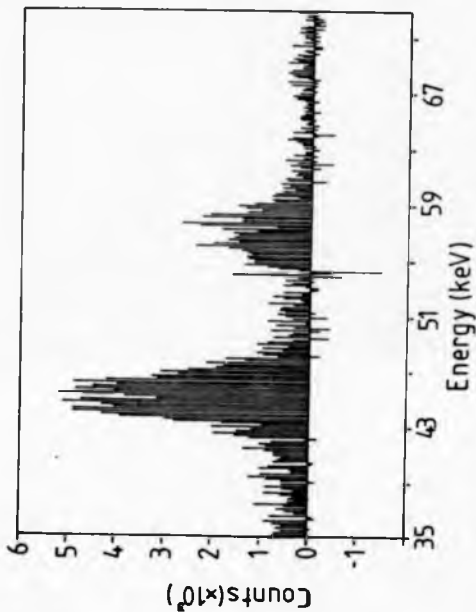
Figure 5.12 Experimental magnetic difference profile of polycrystalline iron. The elastic lines at 54keV and 71.9keV (not shown) have cancelled, however there are still small positive residual differences outside the region of the magnetic profile.

The corrected magnetic Compton profiles of iron and cobalt were then transformed to an electron momentum scale using equation 1.20. The total resolution due to the spectrometer and the detector resolution corresponds to a Gaussian of FWHM=0.7a.u.. No correction for multiple scattering was made in line with the prediction of Sakai (1987) that it should be negligible ($\sim 3\%$ of $J_{mag}(p_z)$). To improve the statistical accuracy of each data point the profiles were left-right averaged.

Iron Metal.

The magnetic profiles of polycrystalline iron reported in section 4.4 link the region of negative magnetisation associated with the s/p hybrid electrons with the 'volcano-like' profile structure. The central dip in this measurement is larger than that predicted by the APW calculation. Shull and Mook (1966) studied the neutron magnetic scattering amplitudes of ferromagnetic iron using an averaging process to remove effects caused by data-termination. They associated a negatively polarised contribution of $0.21\mu_B$ with the interatomic regions where as the band calculation predicts approximately half this value for the low momentum region (i.e $0.1\mu_B$, Wakoh and Yamishita, 1966). The amount of negative polarisation can be obtained from Compton data by estimating the area of the dip in the profile with respect to the $2.2\mu_B$ total area of the profile. For the previous study a value of $0.30\pm0.05\mu_B$ is obtained.

Two further magnetic Compton studies have been recently undertaken, one with circularly polarised 129.5keV γ-rays from a cooled oriented ^{129m}Ir nuclei (Sakai and Sekizawa, 1987) and the other with CPSR produced from linearly polarised radiation by virtue of a quarter-wave plate (Mills, 1987). Both studies present results on ferromagnetic iron with the cooled isotope data being the more statistically accurate (2×10^6 counts under $J_{mag}(p_z)$ cf $\sim 10^4$ counts). These results are reproduced in figure 5.13. The cenral dip in both measurements is approximately mid-way between the SRS Compton data ($0.17\pm0.05\mu_B$ isotope, $0.20\pm0.05\mu_B$ CPSR) and the theoretical predictions and represent a degree of negative polarisation which is close to that predicted by the neutron data.

It was mentioned in the previous chapter that the APW calculation is limited to $|p| < 5a.u.$ and is missing the high momentum components of the Compton profile at all momenta. This
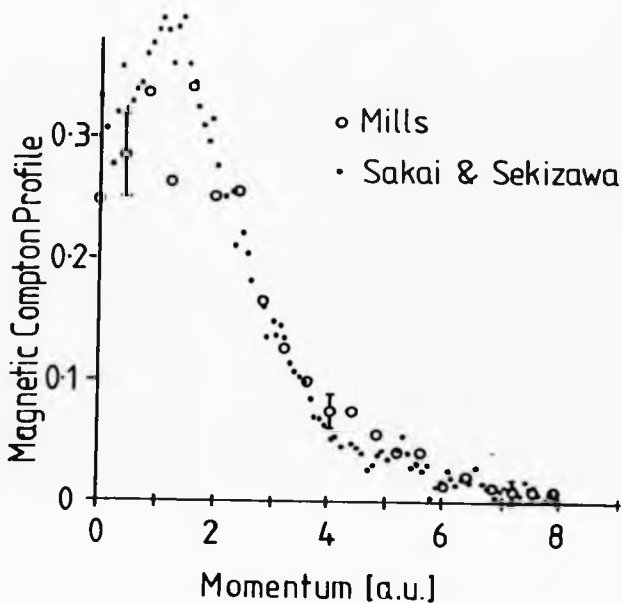
Figure 8.13 Previous measurements of the magnetic Compton profile of polycrystalline iron. The radioisotope data (filled circles) contains 2×10^8 counts under $J_{mag}(p_z)$ and is more statistically accurate than the CPSR result (open circles, $< 10^4$ counts). Both measurements were reported at a resolution of $1.05 a.u.$.

APW calculation has now been extended to $|p| < 7$a.u. (Wakoh, private communication) and the new magnetic Compton profile corresponds to a full moment of $2.2\mu_B$, i.e. it encompasses the whole of the spin dependent distribution. A further calculation of the magnetic Compton profile of ferromagnetic iron has been performed by Poulter and Staunton (1988) using the KKR approach to magnetic systems . This new calculation predicts a somewhat larger negative magnetisation ($\sim 0.15\mu_B$) than the APW calculation.

The magnetic Compton profile of iron obtained from this study is shown at intervals of 0.25a.u. in figure 5.14 where it is compared with the extended APW and the new KKR calculations of the momentum density. Both calculations have been convoluted with a Gaussian of FWHM=0.68a.u. to mimic the experimental resolution. The data, KKR calculation and the results of Mills and Sakai and Sekizawa (see figure 5.13) are all normalised to the area of the APW caculation in the range 0a.u.$< p_z < 7$a.u. . The comparisons of the experimental results and the theoretical models will be made on the following three points: The half width at half maximum (HWHM) of the profile, the dip around $p_z = 0$a.u. and finally the high momentum region $p_z > 5$a.u..

A good agreement is found between the HWHM (~ 3a.u.) of the present data , both theoretical profiles and the experimental results of Mills and Sakai and Sekizawa. The theoretical profiles are also in good agreement with the data at high momentum, $p_z > 5$a.u., in particular, the extended APW model now exhibits the high momentum components of the electron density which were missing from the original model. The discrepancy in the original model was also noted by Sakai and Sekizawa (1987) who suggested an underestimation of electron electron correlations in the theoretical calculation was responsible. However the discrepancy can now be attributed to the limitation of the original calculation.

There is now a general agreement on the size of the experimentally observed central dip which corresponds to a negative spin polarisation of the s/p hybrid electrons of $0.20 \pm 0.05\mu_B$ which agrees with the value of $0.21\mu_B$ obtained from neutron diffraction studies. All data show a peak at a value of $p_z = 1.5$a.u. but the decrease of the profile towards $p_z = 0$a.u. is more marked for the experiment than either of the theoretical profiles. The APW profile is still too high at the origin and possibly too low at intermediate values (2a.u.$< p_z < 4$a.u.) though
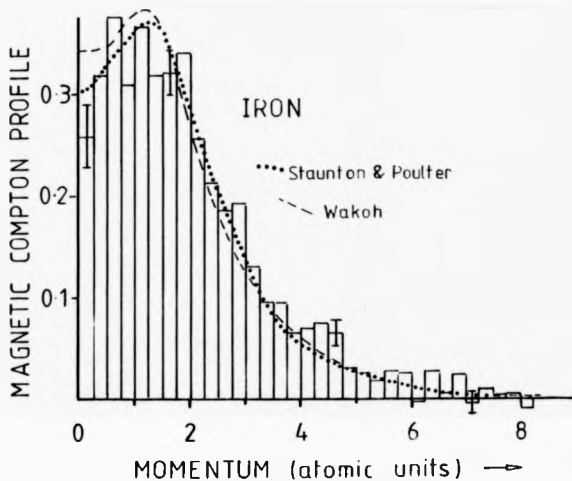
Figure 5.14 The magnetic Compton profile of iron shown at intervals of 0.25a.u. after left right averaging the data. The extended APW model due to Wakoh (broken line) and the KKR calculation of Poulter and Staunton (dotted line) have been convoluted with a Gaussian of FWHM=0.7a.u. which mimics the experimental resolution function.

the statistical accuracy in this region is insufficient to confirm this. In terms of APW band theory the discrepancy in the size of the dip means that the contribution from the negatively polarised 4s/p hybrid electrons is still underestimated.

Qualitative agreement between the experiment and the KKR profile is observed. The negative polarisation contribution of the 4s/p electrons appears to be only slightly underestimated, there is no discrepancy at intermediate values of momentum as with the APW model and good agreement is observed at high momentum. At first sight the KKR model appears to provide a better prediction of the momentum density of the unpaired electrons in ferromagnetic iron than does the APW model. However according to Staunton (private communication) there is an uncertainty in $J_\uparrow(p_z)$ and $J_\downarrow(p_z)$ of $\pm 0.5\%$ per 0.05a.u. interval. This error would be magnified to approximately $\pm 10\%$ on formation of $J_{mag}(p_z)$. The KKR spherical average of $J_{mag}(p_z)$ was calculated from a weighted average of the 100, 110 and 111 directional magnetic Compton profiles . This is in contrast to the APW case where the spherical average was formed from an integration of the electron momentum density over the whole Fermi sphere. As a result of the error in $J_\uparrow(p_z)$ and $J_\downarrow(p_z)$ the anticipated consistency in the areas of the individual directional profiles was not observed. In fact the area of the 111 profile was some 6% larger than the 110 profile and the 100 profile some 6% smaller. Therefore the spherical average $J_{mag}(p_z)$ shown in figure 5.14 contains too much 111 and too little 100 electron momentum density and is not a true representation of the spherical average of $J_{mag}(p_z)$.

In conclusion , although the KKR calculation of the electron momentum density results in a magnetic Compton profile which is in better agreement with the experimental result than the extended APW model it is somewhat fortuitous; the uncertainty in the directional KKR Compton profiles rules out a quantitative comparison with the experiment.

Cobalt Metal.

The magnetic Compton profile of polycrystalline cobalt is presented at intervals of momentum of 0.5a.u. in figure 5.15. The data is of lower quality than the iron despite the longer measurement period. This is due in part to the lower moment $(1.72\mu_B)$ of cobalt but mainly
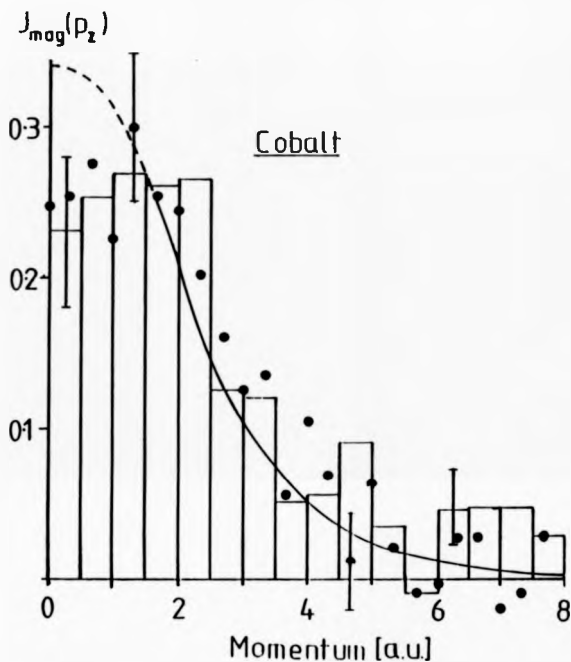
Figure 5.15 The magnetic Compton profile of cobalt shown at intervals of 0.5a.u. after left right averaging the data. The curve is the atomic 3d distribution convoluted with the experimental resolution function of 0.7a.u. FWHM. The filled circles represent the results of Mills which were reported at a resolution of 1.05a.u..

because the field induced by the electromagnet was insufficient to fully saturate the cobalt foil. The Laué photograph of the cobalt foil suggested a granular structure composed of many randomly oriented single crystals or crystalites. The easy direction for magnetisation in hexagonal cobalt is along the c-axis of the single crystal whereas the hard direction is in the basal plane (see figure 5.16). In this polycrystalline sample some of the crystallites would have been aligned in the easy direction, some in the hard direction and most somewhere in between. For this reason complete saturation of this polycrystalline sample was not possible.

Despite this problem the central dip characteristic of negative polarisation in cubic structured ferromagnets such as Fe and Ni (see Rennert, Carl and Hergert, 1983) is also evident in the hexagonal structured ferromagnetic material. Also shown in figure 5.15 (filled circles) is the only other known measurement of the magnetic Compton profile of cobalt (Mills, 1987). Within the statistical accuracy of the data both measurements are in agreement. The negative polarisation contribution of the s/p hybrid electrons in cobalt was estimated by Mills to be $0.10 \pm 0.06 \mu_B$.

There is no band calculation of the electron momentum density in cobalt, although one is now in progress as a result of this measurement (Wakoh, private communication). The curve superimposed in figure 5.15 is the 3d atomic Compton profile (Biggs, Mendelsohn and Mann, 1975) of cobalt. The atomic profile and both the experimental data sets are normalised to the magnetic moment of cobalt ($1.72 \mu_B$) in the range $|p_z| < 5$a.u.. At intermediate and low momentum the atomic profile is a good fit to the data suggesting that in this region the magnetisation is due almost entirely to the d-electrons as is the case for ferromagnetic iron. A band calculation is required to model the low momentum behaviour in particular to predict the negative magnetisation contribution of the s/p hybrid electrons.
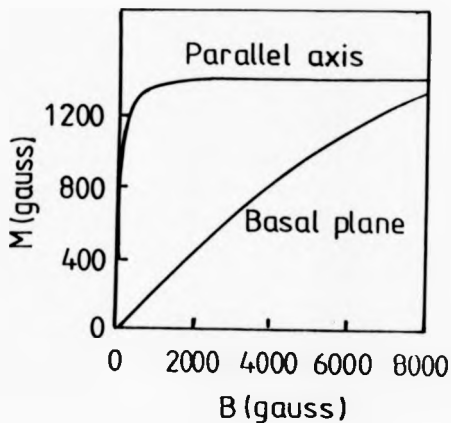
102

Figure 5.16 The magnetisation curve for a single crystal of cobalt. The difficulty in obtaining complete saturation in a granular polycrystalline sample stems from the difficulty in magnetising the crystallites along the hard magnetisation direction i.e. the basal plane (from Kittel, 1976).

Chapter 6

DIRECTIONAL MAGNETIC COMPTON STUDIES.

6.1 Introduction.

The level of interpretation of magnetic Compton profiles is limited by the poor resolution of the solid state detector. At present the low/modest count rates rule out the use of higher resolution devices, such as focusing crystal spectrometers because of their poor detection efficiency. However, this poor resolution may be tolerable if the information content of the results could be made more specific. For example, Wakoh and Kubo (1977) predict a marked magnetic anisotropy in the electron momentum density of iron (see figure 6.1). Thus, the enhanced information content obtained from directional measurements of the spin density will provide a more critical test of band theory than is possible with polycrystalline samples.

The anisotropy of the charge density of iron has already been observed in diffraction studies (Diana, Mazzone, 1974) where an inequality of 'paired' Bragg reflections occurring at the same momentum transfer was observed. As mentioned earlier, the spin density distribution of iron has also been studied with polarised neutrons (Shull and Yamada, 1962 and Shull and Mook, 1966). They interpreted their results in terms of an excess of majority spins along the 100 directions and a deficit, i.e. a negatively polarised magnetisation density, in the interatomic regions along the 110 and 111 directions. Electrons situated in the outer regions of the atomic cell will in general possess small momentum, therefore in a magnetic Comp-
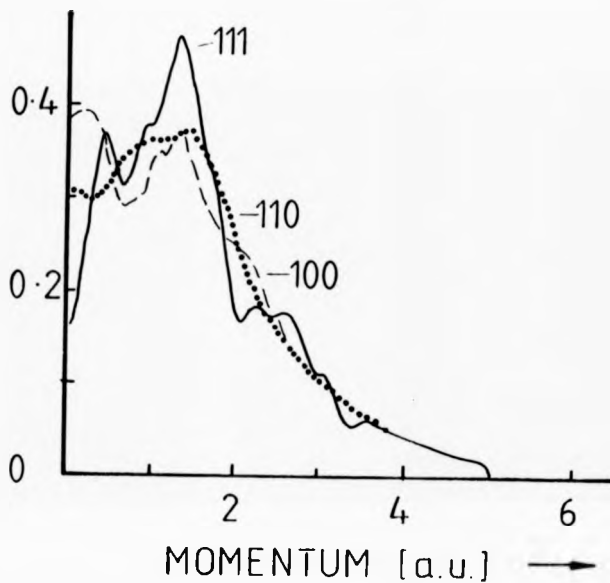
Figure 6.1 The magnetic anisotropy in the electron momentum density of ferromagnetic iron (after Wakoh and Kubo, 1977).

ton experiment, the measured anisotropy in the spin density will be manifest as directional differences near the origin of the profiles.

The annihilation of polarised positrons has also been used to study this negative polarisation in the interstitial regions (for example see Mijnarends, 1973 and references within). Due to parity conservation, most positron emitters emit positrons partially polarised along their direction of motion. Mijnarends (1973) used a 17kG magnetic field to focus the positron beam emitted by a 50mCi ^{22}Na source upon a magnetised iron sample. The energy spectrum of the beam was hardened using titanium filters, which also served to increase the average polarisation of the beam. In CPSR studies, aluminium filters are employed to harden the pre-monochromated and scattered beams. In a magnetised ferromagnetic crystal a polarised positron will, after achieving thermal equilibrium within the sample, annihilate with a spin aligned electron. Quantum mechanical selection rules allow annihilation by emission of 2-γ quanta from the singlet state and by emission of 3-γ quanta from the triplet state. If the probability of occurrence of the 3-γ process is assumed negligible, only electrons with spins aligned opposite to the positron spin may annihilate by the 2-γ annihilation process. Then if in a similar way to magnetic Compton scattering, the direction of the magnetic field is reversed, the other spin band can be sampled and the difference spectrum will reveal information on the spin density in momentum space.

The positively charged positron is unable to sample the components of the electron wavefunctions situated near the positive core and therefore is best suited to studying the valence and conduction band electrons in metals where changes in the Fermi surface shape can be investigated in detail. For example, Mijnarends (1973) demonstrates that positron annihilation can distinguish between different band structure models that produce nearly entirely identical Fermi surfaces.

The technique of positron annihilation has a number of advantages over Compton scattering. Firstly, the resolution of the results is almost an order of magnitude better (refer back to figures 3.1a and b). Secondly, positron annihilation experiments are able to measure a two dimensional projection of the momentum density in contrast to the one dimensional projection measured in Compton scattering studies. Fortunately for Compton scatterers, there

are also disadvantages. The mathematical removal of the positron wavefunction $\psi_+(\mathbf{r})$ from the measured electron momentum density i.e. $\rho(\mathbf{r}) = |\int e^{i\mathbf{p}\cdot\mathbf{r}}\psi_+(\mathbf{r})\psi(\mathbf{r})d^3\mathbf{r}|^2$ is very difficult requiring $\psi_+(\mathbf{r})$ to be evaluated self consistently within the crystal potential and field of the other electrons. There is also a significant degree of electron positron correlations which tend to oppose the effects of electron electron correlations within the sample. Finally, the positron has a tendency to become trapped in lattice defect sites where it preferentially annihilates and therefore does not sample the average ground state electron momentum density. In conclusion, Compton scattering, if performed at a similar resolution to positron annihilation, would offer the more critical test of band theory.

Wakoh and Kubo (1977) have calculated both spin dependent directional Compton profiles and directional positron annihilation angular distributions for ferromagnetic iron by the APW method. They claim good agreement between their theory and the positron annihilation results of Mijnarends (1973). In this chapter the directional magnetic Compton profiles of ferromagnetic iron are presented. These profiles are compared with the theoretical model of Wakoh and Kubo thereby providing a further and for the reasons given above, a more critical test of the band theory.

6.2 Transmission Magnetic Compton Scattering.

In the case of non-magnetic Compton scattering, the progression from polycrystalline to directional studies involving single crystal samples requires little more than additional care in aligning K along a specific crystallographic direction. The situation becomes complicated for directional magnetic Compton studies because the applied field, B_{app} the alignment direction of the electron spins, s_a and K must be simultaneously aligned in anti/parallelism. Unfortunately it is not possible to achieve this alignment with the magnet design and the scattering configuration employed for polycrystalline studies. However, directional magnetic Compton studies are possible if a transmission scattering geometry is adopted in preference to the more usual reflection geometry as can be seen in figure 6.2.

For this experiment a single crystal wafer oriented with the 110 crystallographic axis
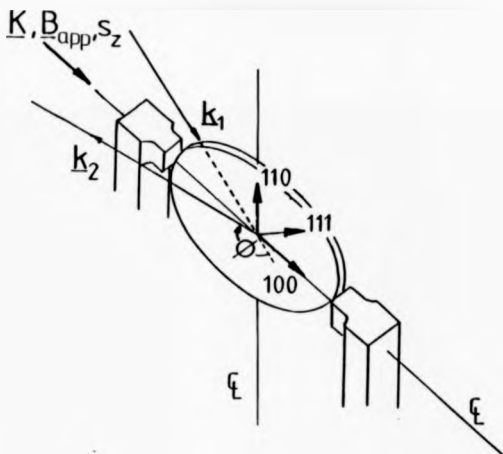
Figure 6.2 Directional magnetic Compton studies. A single crystal wafer oriented with the sample face perpendicular to the $1\bar{1}0$ crystallographic axis is placed across the pole pieces of an electromagnet. Each of the three main crystallographic axis may be brought in to parallelism with $\mathbf{K}$, B_{app} and s_z by simply rotating the sample by a predetermined angle. In the above situation, the momentum density distribution along the 100 direction is being probed.

perpendicular to the sample face is placed across the poles of a suitable magnet. The three main crystallographic directions (i.e. 100, 110 and 111) can be brought into parallelism with B_{app}, s_z and K by simply rotating the sample. The details for the design of a suitable magnet for this transmission scattering experiment will now be discussed.

6.2.1 Magnet Design.

As in the previous studies the controlled reversal of the applied magnetic field is necessary to isolate the unpaired spin contribution to the scattering. Although systems involving rotating permanent magnets and solenoids were considered, a current controlled electromagnet similar to the one employed for the polycrystalline studies and described in chapters 4 and 5, proved to be the most suitable.

The electromagnet designed and built for these single crystal studies is shown in plan and side views in figures 6.3a and b and is illustrated in figure 6.4. The pole pieces of the electromagnet may be adjusted to ensure the 'wasted' sample at the sample/pole contact is minimal ($\sim$ 2mm). This is necessary in view of the limited sample size and the fact that the largest crystals obtained were generally oval (e.g. iron diameters, 26mm maximum, 24mm minimum).

The alignment of B_{app}, s_z and K with a specific crystallographic axis is complicated. The difficulties arise through trying to achieve a large incident beam (i.e. maximum flux) incident at a small angle, η (for η small, $k_1.S(p)$ is a maximum, see equation 1.47) onto a single crystal sample of limited size and then detecting the radiation scattered at an angle close to back scattering. (i.e. to maximise G_z in equation 1.50), without inadvertently affording any view of the magnet. This conflict is illustrated schematically in figures 6.5a and b for a sample of given length, L. Figure 6.5a shows that a large incident beam (i.e. $\frac{L}{\sqrt{2}}$) implies η large (i.e 45°) and ϕ small ($\sim$ 120°), which in turn gives $G_z \sim \frac{1}{2}$ and $\cos \eta \sim \frac{1}{\sqrt{2}}$. Figure 6.5b shows that if the incident beam is reduced by a factor of 2 (i.e. $\frac{L}{2\sqrt{2}}$), a large scattering angle is possible ($\phi \sim 150°$), $G_z \rightarrow$ maximum and $\cos \eta \sim 1$. Unfortunately, at small values of η and large values of ϕ, the incident and scattered beams tend to interfere with the magnet poles as shown in figure 6.5b. To overcome this problem the pole pieces were 'cut away'
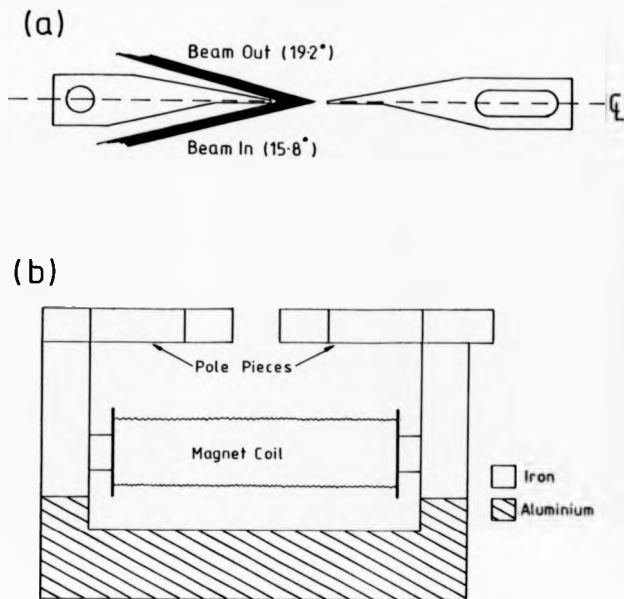
106

Figure 6.3 Magnet design for transmission magnetic Compton scattering. (a) Plan view of the magnet pole pieces. For $\omega_1 = 59 \text{keV}$ and $\phi = 145°$, the incident and scattered wavevectors must be aligned at angles of $\eta_1 = 15.8°$ and $\eta_2 = 19.2°$ to the sample to ensure that $\mathbf{K}$ is correctly aligned. (b) Side view of the magnet. The pole gap is adjustable.

Figure 6.4 Illustration of the magnet employed for directional magnetic Compton studies.

The single crystal wafer is seen held between the pole pieces by two spring steel clips.
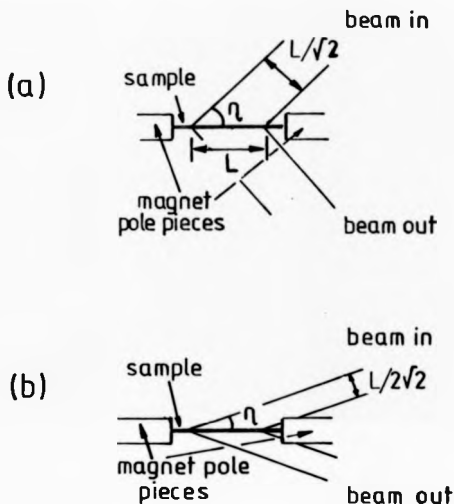
Figure 6.5 Photon flux and geometrical considerations. (a) A photon beam of significant width (e.g. $\frac{L}{\sqrt{2}}$, where L is the sample length) implies η large ($45°$ here) and ϕ small ($\sim 120°$). (b) The appropriate geometry i.e. $\eta < 20°$, $\phi > 150°$ can only be achieved if the beam width is reduced to $\frac{L}{2\sqrt{2}}$. However at such small inclinations the incident and scattered beams tend to interfere with the magnetic pole pieces.

(see figure 6.3a) such that for scattering angles upto $\phi \sim 150°$ and η as small as 15–$20°$, the magnet is not in view of either the incident or scattered beam. Shaping the pole pieces in this manner has a further advantage; it gradually restricts the lines of magnetic flux thereby increasing the flux density within the thin sample and minimising the flux loss. Therefore the thin sample ($\sim \frac{1}{2}$mm) saturates at a somewhat lower field than the bulk of the magnet.

The number of turns, N of 0.5mm insulated copper wire required to saturate the electro-magnet with zero pole gap (i.e. no sample and the pole pieces pushed together) was calculated for a current of 1A to be 1500 ($B_s = \frac{\mu_0 NI}{2\pi R}$ with $B_s = 0.06$T to saturate pure iron). The actual number of turns used was 2500, this is more than sufficient to ensure saturation along all directions in single crystal iron (see figure 6.6). To check that the sample was saturated, a small coil was wrapped around the sample and the current induced in this coil was measured as a function of the current in the electromagnet coil. The induced current maximised for $I > 0.3A$ (i.e. the saturation current). Finally, spring steel clips were attached to each pole piece to secure the sample during field reversal.

6.2.2   The Optimum Sample Thickness.

Unlike reflection Compton scattering experiments the Compton scattered intensity obtained in a transmission experiment is critically dependent upon the sample thickness. If the maximum Compton scattered intensity is to be achieved this thickness must be optimised for the proposed scattering configuration and incident energy.

Consider a beam of intensity I_0, incident at an angle η_1 to the surface of a sample of uniform thickness t. The Compton scattered intensity from an element dx a distance x into the sample is given by,

$$I_c = I_0 \exp(-\mu_1 x \, cosec\eta_1)\mu_c \exp(-\mu_2(t-x)cosec\eta_2), \qquad (6.1)$$

where μ_1 and μ_2 are the attenuation coefficients of the sample material at ω_1 and ω_2 respectively, μ_c is the Compton linear absorption coefficient at ω_1 and η_2 is the angle between the scattered beam and the sample. The total Compton scattered intensity I_c is given by,
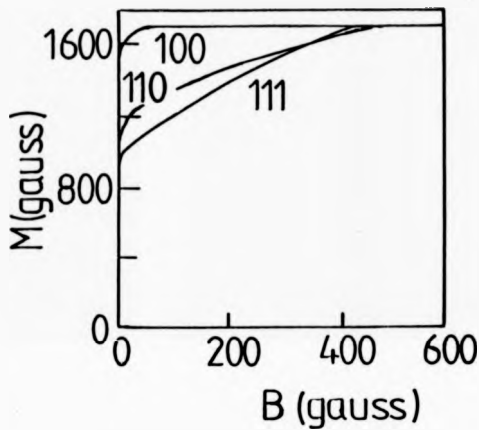
Figure 6.6 The magnetisation curve for a single crystal of iron. The saturation magnetisation of iron is ~1600 gauss or 0.16T (1 gauss ~ 10^{-4}T), from Kittel, (1977).

$$I_c = I_0 \mu_c \int_0^t \exp(-\mu_1 x \cos ec \eta_1) \exp(-\mu_2 (t-x) \cos ec \eta_2) dx. \qquad (6.2)$$

Assuming $\eta_1 = \eta_2 = \eta$, the above integral gives,

$$I_c = I_0 \frac{\mu_c}{\mu_2 - \mu_1} \sin \eta \exp(-\mu_2 t \cos ec \eta)[\exp(-\mu_1 t \cos ec \eta) - \exp(-\mu_2 t \cos ec \eta)]. \qquad (6.3)$$

Shown in figure 6.7 is I_c as a function of t for scattering from iron where $\eta = 20°, \omega_1, \omega_2 = 60$, 50keV and $\omega_1, \omega_2 = 50$, 40keV. In each case, the maximum value of I_c has been normalised to unity. At the optimum thickness t_{opt}, $\frac{dI_c}{dt} = 0$ therefore,

$$t_{opt} = \sin \eta \frac{\ln(\frac{\mu_2}{\mu_1})}{\mu_2 - \mu_1}. \qquad (6.4)$$

For $\omega_1 = 50$keV (i.e. the optimum energy, see section 5.2.1) $\Phi = 150°$ and $\eta = 15$–$20°$, equation 6.4 and figure 6.7 predict $t_{opt} \sim 0.15$mm.

To estimate the ratio of transmission to reflection Compton scattered intensities $\frac{I_{trans}}{I_{ref}}$ the approximation $\mu_1 \sim \mu_2 = \mu$ is made. Then, for $t = t_{opt}$, equation 6.4 gives

$$I_{trans} = \sin \eta \frac{I_0 \mu_c}{e \mu} \qquad (6.5)$$

and for thick sample reflection,

$$I_{ref} = \sin \eta \frac{I_0 \mu_c}{\mu_1 + \mu_2} \sim \sin \eta \frac{I_0 \mu_c}{2 \mu}. \qquad (6.6)$$

Therefore $\frac{I_{trans}}{I_{ref}} \sim \frac{2}{e} = 0.74$ which represents a tolerable reduction in scattered intensity.

6.3 Experimental Technique.

6.3.1 Sample Preparation.

Commercially available single crystals of pure iron are limited to a maximum diameter of ~ 8mm. However much larger single crystals are necessary to obtain a significant magnetic Compton scattered signal. In order to grow large single crystals of iron it is necessary to add
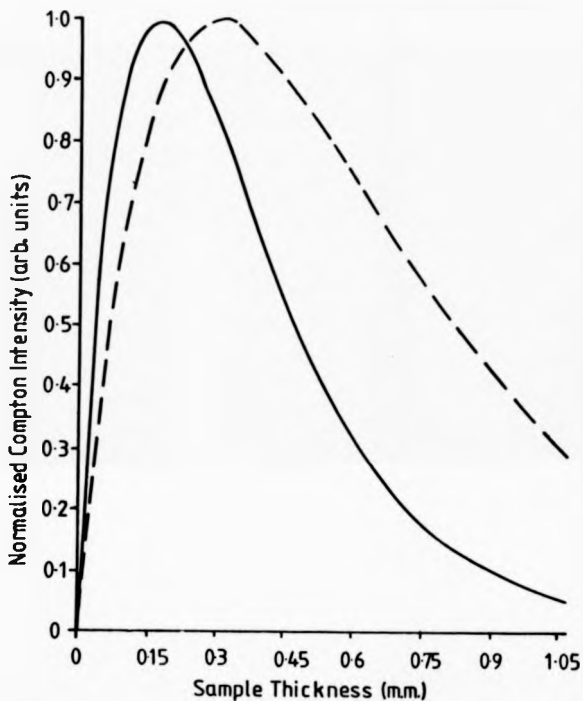
Figure 6.7 The optimum sample thickness. The Compton scattered intensity, I_c as a function of sample thickness, t from iron for $\omega_1, \omega_2 = 60, 50\text{keV}$ (solid line) and $\omega_1, \omega_2 = 50, 40\text{keV}$ (dashed line). In each case the maximum value of I_c has been normalised to unity.

a small percentage of silicon (a few atomic %) to the melt. The silicon stabilizes the body centered cubic (bcc) iron lattice and as it is substitutional (see Tebble and Craik, 1969) there is little change to the original lattice.

A randomly oriented single crystal of silicon stabilised iron 24mm diameter by 60mm long was purchased from Metal Research, Cambridge. A compositional analysis of the crystal performed using an electron microscope revealed the crystal contained $3.0\pm0.1\%$ atomic silicon. The crystal was oriented using the Laué method, the continuum radiation being provided by a 1.0kW Mo anode x-ray source. An oval single crystal wafer, 26mm×24mm oriented with a 110 crystallographic axis perpendicular to the face was cut from the crystal by spark erosion. This wafer was carefully spark eroded to a thickness of 0.25 ± 0.02mm using a rotating brass cathode and a low H.T. setting to minimise the surface damage.

The Laué method was again used to check the wafer for grain boundaries and twinning, none were detected and finally the 100, 110 and 111 directions were identified in the plane of the wafer (refer to figure 6.2).

6.3.2 Experimental Measurements.

This study was, like the previous polycrystalline studies, performed on the topography station W9.4 of the SRS. Figure 6.8 shows a schematic diagram of the apparatus which has been elevated to the optimum position (see section 5.2.1), some 6mm above the orbital plane. As usual the orbital position was relocated after each machine refill and the elevation of the apparatus adjusted accordingly.

The 220 Ge monochromator described in section 5.2.5 was chosen for this study and was tuned to a Bragg angle of $3.0°$ to select an energy of 59keV with the 220 reflection. Unlike the 333 reflection used for the previous study there is no subharmonic of the 220 reflection. In addition, for $\omega_1=59$keV (220 reflection) the 440 reflection of 118keV radiation is diminished by both the lack of synchrotron flux at these high photon energies and the poor reflecting power of the 440 reflection ($R = 67.4\times10^5$ and 27.5×10^5 respectively, see table 4.1). Thus any magnetic scattering arising from this reflection can be neglected. Therefore the 220 reflection offers a reduced magnetic background and a reduced risk of dead time problems resulting
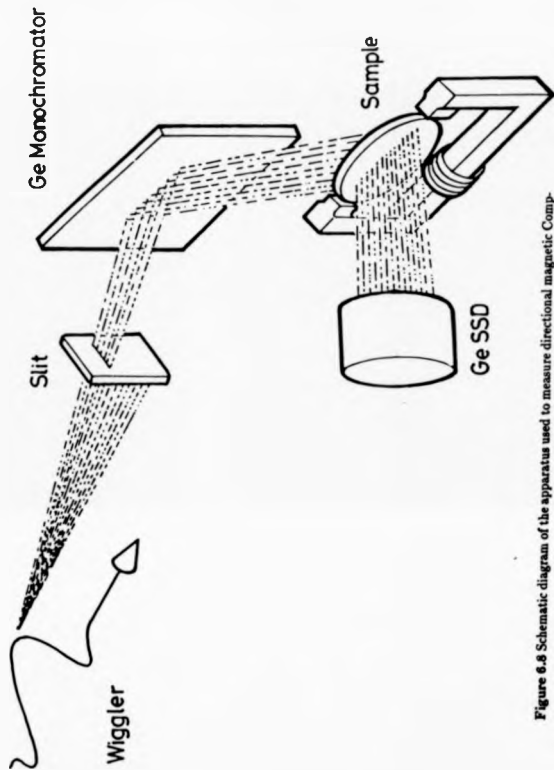
109

Figure 6.5 Schematic diagram of the apparatus used to measure directional magnetic Compton profiles from single crystal samples of iron.

from unwanted low energy photons.

A scattering angle of 145° was chosen and to align $\mathbf{K}$ in the plane of the sample, the angles between the sample and $\mathbf{k_1}$ and $\mathbf{k_2}$ (i.e. η_1 and η_2) were set to 15.8° and 19.2° respectively, see figure 6.3a. To ensure that the magnetic poles were not in view of the monochromated beam, polaroid photographs of the photon beam were taken before and after transmission of the photon beam through the sample.

The Compton scattered radiation was detected by the same intrinsic Ge detector used previously and as before the data was channelled into alternate memories of an Ortec MCA according to the magnetic field direction. Individual measurements of $J_{mag}(p_z)$ for each crystallographic direction were alternately made thereby providing a check of the reproducibility of the results.

6.4 Results.

This study was performed 6 months after the recommissioning of the SRS by which time the beam currents (upto 200mA on injection), lifetimes (upto 20 hours) and general stability of the electron beam (see figure 6.9) had been greatly improved. This in turn was manifest as a factor of 5 increase in the available incident intensity. This increase compensated for reductions in the Compton scattered intensity resulting from; the change to a transmission scattering geometry (refer to section 6.2.2), the move to a higher photon energy (59keV from 54keV, which was necessary in order to improve the detector resolution) and the limitations imposed on the source size (5mm×3mm compared with 5mm×7mm) by the smaller sample size.

Each machine fill, now every 12 hours, resulted in ~8 hours of useful data collection. The individual spin up and spin down profiles from each fill were corrected for small peak shifts resulting from slight changes in the scattering angle and then added together. A total of ~24 hours of data collection was obtained for each crystal direction which corresponds to a total of $\sim 10^7$ counts under each directional spin up and spin down profile. The degree of circular polarisation of the beam was $P_1=0.57$ (taken from figure 5.1b) and an average magnetic effect
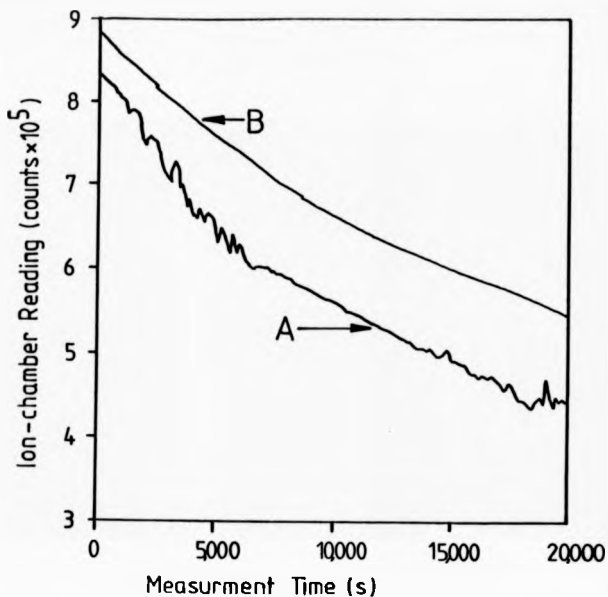
Figure 6.9 Beam stability. Curve A was measured soon after the recommissioning of the SRS whereas curve B was measured during the present experiment. An improvement in source stability and lifetime (A has a steeper gradient than B) is evident from a comparison of A and B.

of $\frac{I_1 - I_2}{I_1} \sim 1.7\%$ were observed, i.e. $\sim 2 \times 10^5$ counts under each directional difference profile.

A data processing package developed by S. Collins (private communication) was applied to the total profiles. This routine corrected the profiles for the energy dependent scattering cross section and also for the attenuation of the beam in the sample. The directional difference profiles $J_{mag}(p_z)$ were evaluated and as usual complete cancellation of the elastic and x-ray fluorescence lines was observed, indicating that systematic errors were absent from the difference spectra. Due to the absence of a 330 reflection and the minimal flux arising from the high energy 440 (118keV) reflection a magnetic background correction (see section 5.5.2) was deemed unnecessary.

In an attempt to remove the effect on $J_{mag}(p_z)$ of the detector response function, a simple tail stripping routine (S. Collins, private communication) was applied to the data. This routine treats the detector response function as a delta function positioned at the photopeak energy, ω_1, plus a constant tail extending 10 keV below the delta function. This pseudo-response function was systematically subtracted from each data point in the directional spin up and spin down profiles. Obviously, the correct procedure is that employed to correct γ-ray Compton profiles (see chapter 2), namely a deconvolution of the data with a detector response function measured at the compton peak energy. However, the statistical errors in $J_{mag}(p_z)$ ($\pm 10\% J_{mag}(0)$) are much larger than the corresponding errors in $J(p_z)$ ($\pm 0.20\% J(0)$) and such a complicated deconvolution procedure is unnecessary in view of the current scale of sophistication of the measured magnetic Compton profiles.

The corrected directional magnetic Compton profiles were transformed to a momentum scale using equation 1.20 and to improve the statistical accuracy of each data point, the data was left-right averaged and displayed on a momentum interval of 0.2a.u. . The momentum resolution of the final profiles was obtained by estimating the contributions to the resolution at the Compton peak energy ($\omega_2 = 48.8$keV) from the detector, monochromator and geometrical effects.

The detector resolution at the Compton peak energy was obtained as ~ 380eV by measuring the FWHM of the 59.54keV and 26.36keV γ-emissions of a 10μCi ^{241}Am calibration source and extrapolating to find the FWHM at $\omega_2 = 48.8$keV. The broadening of the measured

111

220 elastic line was attributed to the energy resolution of both the detector, $\Delta\omega_{det}$ and the monochromator, $\Delta\omega_{mono}$ and the resulting FWHM was, $\Delta\omega_{elas}$=402keV. Assuming $\Delta\omega_{det}$ and $\Delta\omega_{mono}$ add in quadrature, the energy resolution of the monochromator was estimated to be $\sim$180eV at 59keV, indicating a rocking curve width of $\Delta\theta = 33$secs.This is in reasonable agreement with the observed rocking curve width of $\Delta\theta$=27secs which was measured with CuKα (8.05keV) radiation (Hart, private communication). Finally, the geometrical resolution of the spectrometer at energy ω_2 was estimated to be $\sim$180keV (see section 5.2.3) and the total resolution of the measured profiles obtained by adding each contribution in quadrature to give $\sim$ 460 $\pm$ 30eV (0.69$\pm$0.05a.u.).

Figure 6.10 shows the three directional magnetic Compton profiles obtained after data processing. Also shown in figure 6.10 are the directional magnetic Compton profiles of iron calculated by the APW method by Wakoh (1987, private communication). This calculation, like the polycrystalline result quoted in chapter 5, is an extension of an earlier calculation (Wakoh and Kubo, 1977). As usual the theoretical profiles have been convoluted with a Gaussian of FHHM=0.69a.u. to mimic the experimental resolution. All profiles are listed in table 6.1.

6.5 Discussion.

6.5.1 Directional Magnetic Compton Profiles.

It is evident from the results shown in figure 6.10 that all three directional profiles are similar at intermediate and high momentum (p_z >2.5a.u.) and agree with the APW prediction within the statistical error of the data. However the experimental profiles do appear to be systematically slightly broader than the APW calculation in the momentum range 2.5a.u.< p_z <4a.u. . This may be attributed to an underestimation of the experimental resolution, in particular an underestimation of the degree of geometrical broadening of the spectrometer.

The directional profiles do exhibit marked differences at low momentum. the central dip is greatest for the 111 profile ($\sim$ 50%$J_{mag}(0)$) and it is entirely absent from the 100 result. The APW calculation reproduces the observed behaviour for the 111 profile but overestimates the
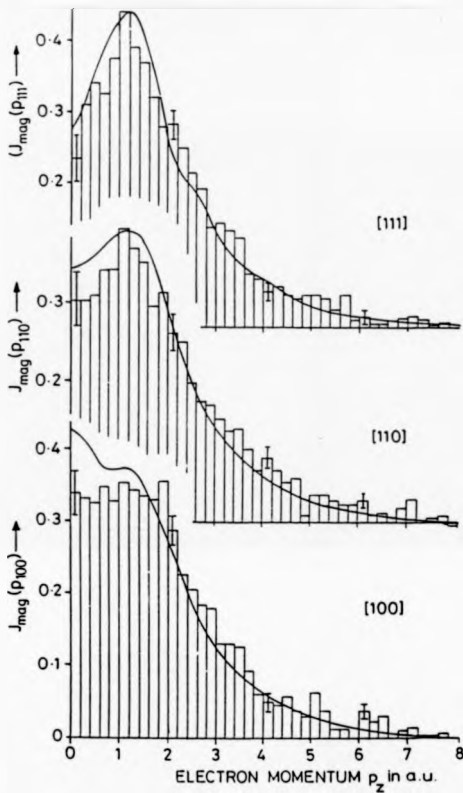
112

Figure 6.10 The histograms show the directional magnetic Compton profiles of iron as a function of p_z, whilst the solid line represents the extended APW calculation convoluted with the experimental resolution function which had a FWHM=0.7a.u.. The magnetic anisotropy is manifest as a variation in the size of the central dip.

P_z	100		110		111		Spher. Ave.	
	Exp.	APW	Exp.	APW	Exp.	APW	Exp.	APW
0.0	0.334 ± 0.008	0.398	0.298	0.322	0.273	0.254	0.294 ± 0.012	0.340
0.2	0.347	0.389	0.307	0.325	0.308	0.277	0.316	0.341
0.4	0.313	0.377	0.315	0.332	0.325	0.315	0.317	0.344
0.6	0.342	0.353	0.337	0.344	0.317	0.349	0.332	0.351
0.8	0.352	0.346	0.371	0.357	0.366	0.376	0.365	0.361
1.0	0.368	0.350	0.387	0.367	0.408	0.401	0.369	0.376
1.2	0.370 ± 0.012	0.352	0.355	0.370	0.411	0.416	0.376 ± 0.10	0.381
1.4	0.353	0.340	0.381	0.364	0.401	0.403	0.381	0.372
1.6	0.349	0.314	0.337	0.342	0.336	0.358	0.339	0.347
1.8	0.303	0.284	0.309	0.307	0.293	0.297	0.302	0.309
2.0	0.277	0.253	0.284	0.265	0.266	0.244	0.277	0.267
2.2	0.226	0.223	0.242	0.223	0.249	0.210	0.241	0.227
2.4	0.216	0.192	0.199	0.188	0.216	0.190	0.208	0.194
2.6	0.171	0.162	0.166	0.180	0.178	0.174	0.173	0.167
2.8	0.155 ± 0.010	0.135	0.161	0.137	0.147	0.152	0.155 ± 0.08	0.145
3.0	0.131	0.116	0.144	0.119	0.149	0.127	0.142	0.126
4.0	0.078	0.068	0.078	0.059	0.067	0.063	0.075	0.061
5.0	0.031	0.030	0.048	0.028	0.035	0.027	0.037	0.029
6.0	0.024	0.013	0.022	0.013	0.023	0.012	0.023	0.013
7.0	-0.002	0.004	0.022	0.004	0.010	0.004	0.013	0.004

Table 6.1 Experimental and theoretical magnetic Compton profile of iron along 100, 110 and 111 and the spherical average of these profiles. The theory has been convoluted with a Gaussian of FWHM 0.60a.u. to mimic the experimental resolution half width.

value about the origin of both the 110 and 100 profiles with the latter deviation being more marked. This observation is consistent with earlier results obtained by several independent measurements (Sakai, Terashima and Sekizawa, 1984, Timms, Brahmia, Collins, Collins, Cooper, Holt, Kane, Clark and Laundy, 1988 and Mills, 1988) of polycrystalline iron in which the measured central dip was at least $\sim 10\%$ smaller than the calculated central dip (see section 5.5.2).

A spherical average profile was calculated by averaging the directional profiles after weighting each in the usual manner, i.e. for cubic iron $\frac{6(100)+12(110)+8(111)}{26}$. The resulting profile is plotted in figure 6.11 together with the APW spherical average profile which has been convoluted with a Gaussian of 0.69a.u.. This figure confirms the conclusions drawn from earlier measurements that the APW model underestimates the contribution of the negatively polarised 4s/p band electrons thereby underestimating the size of the central dip. It was estimated that the central dip corresponds to a negative spin polarisation of $0.20\pm0.05\mu_B$, in agreement with the previous measurement of polycrystalline iron presented in chapter 5. This estimation was obtained by comparing the shape of the spherical average profile with the magnetic profile due to the 3-d electrons of iron, i.e. where no negative polarisation is expected (refer to figure 4.10).

6.5.2 Fermi Geometry.

The origin of the directional variation in the size of the central dip can be qualitatively understood by considering the calculated Fermi geometry of the minority and majority electrons in ferromagnetic iron (see figure 6.12, after Wakoh and Yamishita, 1966). The complex Fermi geometry of iron is characteristic of the 3d transition metals and arises as a consequence of the interaction of the 3d and 4s electrons (Cracknell and Wong, 1973). The Fermi surfaces of the minority bands (labelled A in figure 6.12) are characterised by hole pockets around the reciprocal lattice symmetry points N and octahedral holes around H. The Fermi surface of the majority bands consist of the s-d electron surface (B), two small hole pockets around the H points (C) and the hole arms connecting the H points in the 110 direction (D).

According to Rollason (1984) the minority band electrons are responsible for the low
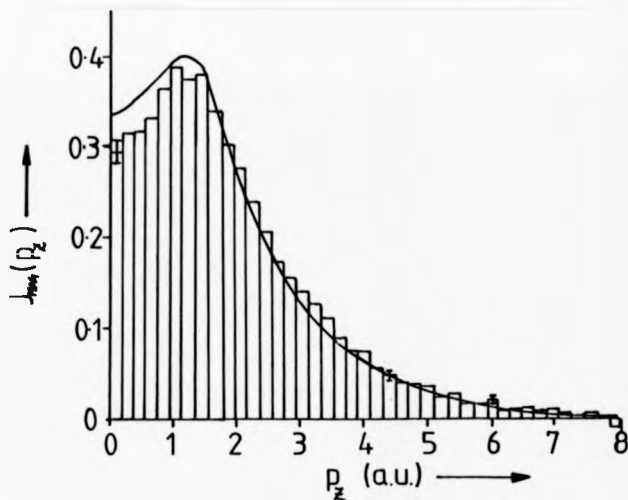
Figure 6.11 Spherical average magnetic Compton profile formed from a weighted average of the individual directional profiles. The solid line represents the extended APW polycrystalline result convoluted with a Gaussian of FWHM=0.7a.u..
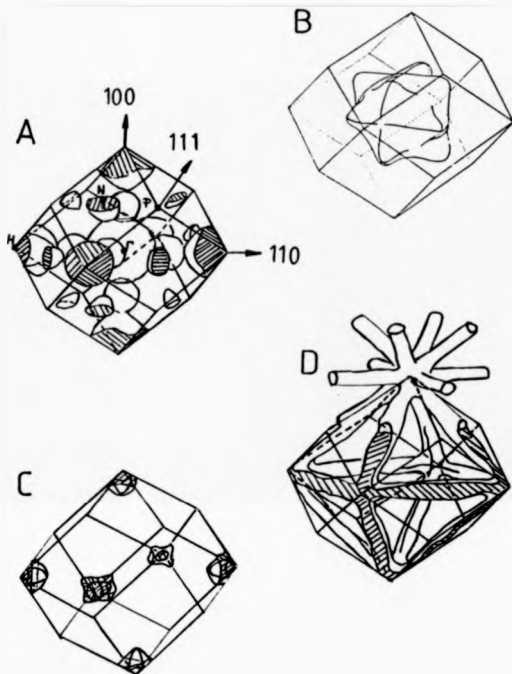
Figure 6.12 A schematic illustration of the Fermi surfaces of iron. The minority band Fermi surface is labelled A. The majority band Fermi surfaces are labelled B, C and D (from Wakoh and Yamishita, 1966).

momentum anisotropy; in contrast the majority band electrons are relatively isotropic. This assumption is enforced by the observation that the minority Fermi surface has large holes at the H-points of the Brillouin zone, whereas much smaller holes are observed at the H-points of the majority Fermi surface. These holes represent a deficit of electrons and therefore result in a positive contribution to the difference profile (remember $J_{mag}(p_z)$ is the integral of $n_\uparrow(p_z) - n_\downarrow(p_z)$).

The Fermi surface due to Tawil and Callaway (1973) is similar in appearance to that of Wakoh and Yamishita and their Fermi surface cross sections in the 100, 110 and 111 planes are reproduced in figure 6.13 where the dashed and solid lines represent the minority and majority bands respectively. De Haas van Alphen measurements of these cross sectional areas by Gold, Hodges, Panousis and Stone (1971) confirm this general appearance.

The Fermi surface cross sections show the distribution of electrons with wavevectors perpendicular to a particular crystallographic plane. The Compton experiment samples the momentum distribution of electrons along K which is aligned parallel to the crystallographic direction. Therefore electrons with wave vectors perpendicular to this plane will contribute to the centre of the profile. The magnitude of the central dip will thus depend upon the number of H-points that exist in the plane through the Brillouin zone perpendicular to K (i.e. perpendicular to the z-direction). From figure 6.13, the 100 direction with 4 H-points should exhibit the largest peak, the 111 with zero H-points the smallest and the 110 with 2 H-points, somewhere in between. This interpretation assumes a free electron density of states below the Fermi surface however, the trend of the measured profiles is in agreement with the above predictions.

6.5.3   Separation of the Majority and Minority Spin Compton Profiles.

The magnetic Compton experiment measures a quantity which is proportional to $n_\uparrow(\mathbf{p}) - n_\downarrow(\mathbf{p})$ whereas the measurable quantity in a nonmagnetic Compton experiment is proportional to $n_\uparrow(\mathbf{p}) + n_\downarrow(\mathbf{p})$. Therefore, it should be possible to isolate the scattering contributions from the majority ($n_\uparrow(\mathbf{p})$) and minority ($n_\downarrow(\mathbf{p})$) spin electrons by forming the sum and differences of $J_{mag}(p_z)$ and $J(p_z)$ respectively, i.e.
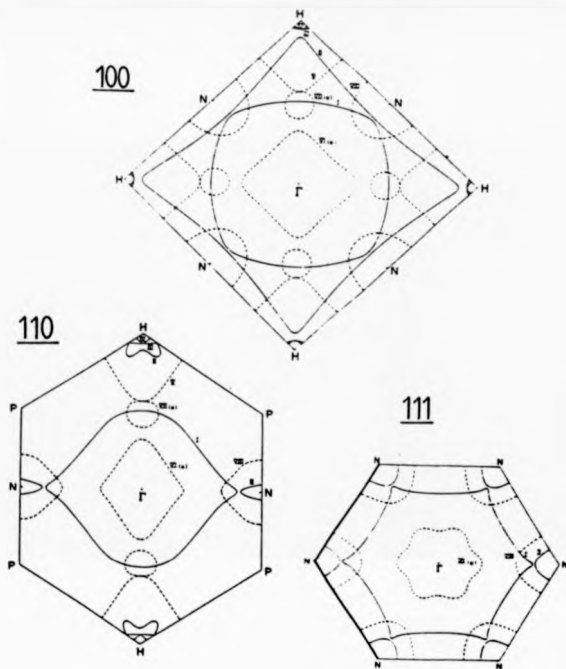
Figure 6.13 Fermi surface cross sections in the 100, 110 and 111 planes in ferromagnetic iron. The solid and dashed lines correspond to the majority and minority electron surfaces respectively. The minority Fermi surface contains large holes at the H-points of the Brillouin zones. The number of H-points in the 100, 110 and 111 planes are 4, 2 and 0 respectively (from Tawil and Callaway, 1973).

$$J_\uparrow(p_z) = \frac{J(p_z) + J_{mag}(p_z)}{2},\qquad(6.7)$$

$$J_\downarrow(p_z) = \frac{J(p_z) - J_{mag}(p_z)}{2},\qquad(6.8)$$

where $J_\uparrow(p_z)$ and $J_\downarrow(p_z)$ are the Compton profiles of the majority and minority spin electrons respectively plus, in each case, an isotropic contribution from the core electrons.

To attempt this separation nonmagnetic Compton profile data $J(p_z)$ was taken from Rollason, Holt and Cooper (1983). Their directional profiles had been deduced from Compton scattering measurements on single crystal slices of pure ferromagnetic iron performed with the 412keV γ-ray spectrometer outlined in chapter 2. The resolution of this data was 0.4a.u. and the profiles were presented on a momentum interval of 0.1a.u.. The data were first converted to the same momentum interval as $J_{mag}(p_z)$ (i.e. 0.2a.u.) and in order to match the resolution of $J(p_z)$ with that of $J_{mag}(p_z)$ (i.e. 0.69a.u.) the data were convoluted with a Gaussian of FWHM=0.56a.u..

The nonmagnetic profile was normalised such that in the momentum range 0–7a.u. it had an area equal to half the atomic number of iron (i.e. 13). Similarly the magnetic data were normalised over the same momentum range to have an area equal to half the number of unpaired electrons (i.e. 1.1). The quantities $J_\uparrow(p_z)$ and $J_\downarrow(p_z)$ were then evaluated using equations 6.7 and 6.8. As in nonmagnetic Compton studies (see chapters 2 and 3) the isotropic contribution from the core electrons was removed by the formation of directional difference profiles. The difference profiles from the majority and minority spin electrons are presented in figure 6.14 where they are compared with the extended APW results of Wakoh (solid line). The theory has been convoluted with a Gaussian of FWHM=0.69a.u..

It is apparent from figure 6.14 that, as predicted by Rollason, the minority band electrons are responsible for the major part of the anisotropy in the electron momentum density of ferromagnetic iron. At intermediate and high momentum ($p_z > 1.5$a.u.) the theory is able to predict the observed anisotropy but this is not so at low momentum ($p_z < 1.5$a.u.). Here the theory appears to underestimate the size of the 100 spin down profile, which is consistent with
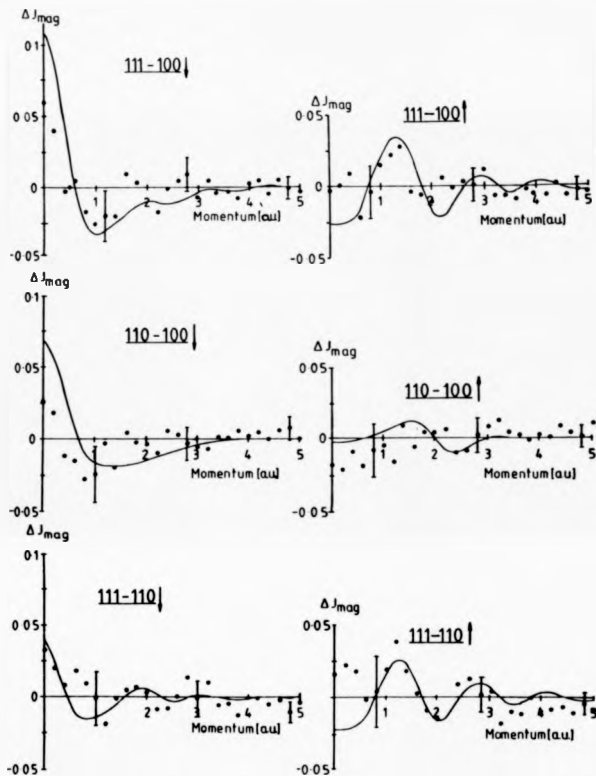
115

Figure 6.14 The majority and minority spin directional difference profiles of ferromagnetic iron. The solid line represents the extended APW calculation convoluted with the experimental resolution function of 0.7a.u. FWHM.

the overestimation of the 100 magnetic profile observed at low momentum (see figure 6.10). There are also some low momentum discrepancies between the experimental and theoretical the spin up anisotropies, although within the statistical accuracy of the data it is not possible to associate these discrepancies with a particular directional profile.

The experimental technique has since been further developed and more precise data (factor of ~1.5 improvement in statistical accuracy) on ferromagnetic iron has been obtained. These data are presently being analysed and it is anticipated that they will enable a quantitative interpretation of the anisotropy in the spin density of iron.

6.6 Conclusions.

The long standing disagreement between the measured magnetic Compton profile of polycrystalline iron and the APW spherical average profile can now be attributed to the APW model underestimating the contribution from the negatively polarised 4s/p electrons along the 100 direction and to a lesser extent along the 110 direction. More specifically, an examination of the individual spin profiles reveals that most of the disagreement can be attributed to the APW model underestimating the contribution from the negatively polarised 4s/p minority spin electrons along the 100 direction. Only a qualitative understanding of the origin of these differences can be obtained from an examination of the Fermi geometry and more elaborate investigations are required for a fuller understanding of the differences between experiment and theory. Despite the inferior resolution and statistical accuracy of magnetic Compton profiles compared with routine γ-ray profiles , it may still be necessary to consider electron correlation effects and spin orbit interactions neglected in the APW theory.

Since the early demonstration measurements of Holt et al (1986) the degree of difficulty in measuring $J_{mag}(p_z)$ has been significantly reduced. Now, a directional magnetic Compton profile of iron may be measured with modest resolution and statistical accuracy in under a day. However, additional precision is required before a quantitative interpretation of the magnetic difference profiles can be made. In the present study, a combination of limited monochromator length and sample size resulted in low/modest count rates.

Chapter 7

Current Developments and Future Work.

7.1 Gamma Ray Work.

The past decade has seen a continual improvement in the accuracy and reliability of γ-ray Compton data. Indeed, in the present work, a better understanding of the many data processing procedures has enabled absolute profiles to be confidently quoted to a reliability of better than $\frac{1}{2}\% J(0)$. This high degree of statistical precision is essential if small directional differences such as those present in disordered alloys (i.e. $< 1\% J(0)$) are to be resolved.

In the past, Compton scattering studies have proven to be a critical test of band theory. This is particularly true in the field of metals, where interaction between experiment and theory has highlighted deficiencies in band calculations and associated them with the band theory's treatment of Coulomb correlations. Unfortunately, the interpretation of Compton data is severely restricted by poor resolution which conceals the information contained within the small effects. At present resolution widths are $\sim \frac{1}{2}$a.u., which represents a sizable fraction of the Brillouin zone. The way forward for this technique lies not with further improvement in precision, but with an increase in the sensitivity of the experiment to place less importance on the accuracy of the interpretive process. This may be achieved by either: improving the resolution to the order of 0.1a.u. (i.e. $\frac{1}{10}^{th}$ of the Fermi momentum of aluminium), or by enhancing the information content of the results (e.g. magnetic Compton studies).

Improvements in resolution of this order can be achieved using focusing x-ray optics and steps in this direction are already being taken (see table 7.1). Such focusing devices

Method	Energy (keV)	Momentum Resolution (a.u.)	Signal:Noise ratio	Compton count rate	Reference
^{198}Au + SSD	412	0.4	500:1	10	Holt et al, 1979
CuKα x-rays focussing spectrometer	8	0.07	15:1	1	Pattison et al, 1981
S.R. (LURE) focussing spectrometer	10	0.15	100:1	30	Loupias et al, 1984
S.R. (Photon Factory) focussing specrometer	29.5	0.08	–	200	Itoh et al, 1988

Table 7.1 Comparison of Compton spectrometers in use and/or in developement (adapted from Cooper, 1989).

normally make use of bright synchrotron sources in order to combat their poor detection efficiency. For example, at LURE, Loupias, Chomilier and Guerard (1984) have used a double crystal monochromator, a curved crystal analyser, a position sensitive detector and 10keV synchrotron radiation to achieve integrated Compton intensities of ~30cps at a resolution of 0.15a.u.,(cf 10cps @ 0.4a.u. for the high energy spectrometer). Itoh et al (1988) have developed a similar spectrometer but employ imaging plates as their position sensitive detector. This spectrometer uses 29.5keV synchrotron radiation extracted from a wiggler line at the Photon Factory, Japan. They quote count rates of 220cps at a momentum resolution of 0.08a.u.. Similar spectrometers are also planned for the European Synchrotron Radiation Facility (ESRF) (see Schülke1986) and laboratory based focusing spectrometers using $CuK\alpha$ and $WK\alpha$ radiation are already in use in Berlin (Pattison, Bleif and Schneider, 1981) and Helsinki (see Manninen et al, 1987).

Although the future will see a move towards the use of focusing devices, the 'traditional' γ-ray spectrometer will still be used to study physically interesting systems where, in the first instance, a high resolution measurement is unnecessary, for example phase transitions. These systems have yet to be performed with a high degree of reliability , which as illustrated by this work, is now possible. Such a study, concerned with a measurement of the electron momentum distribution above and below the Curie temperature of the rare earth ferromagnet gadolinium is presently underway at the University of Warwick.

7.2 Magnetic Compton Studies.

The development of magnetic Compton scattering with CPSR is undoubtably the most exciting and significant advance in Compton spectroscopy during this work. In addition to the results presented here, directional Compton profile measurements of iron have recently been undertaken with improved statistical accuracy (approximately a factor of 2) and a measurement of gadolinium at ~ 90° below the Curie temperature (T_c=292K) has also been performed.

At present, the statistical precision of these data merit, in general, only qualitative inter-

pretation of the data. The difficulties associated with obtaining statistical accuracy in the magnetic difference profile stems from the small size of the cross section. This was discussed in chapter 4 (see figure 4.1). Unlike γ-ray studies where the measurement period is limited by the patience of the investigator or the thermal drift in the detection electronics, synchrotron studies are governed by strict beam time schedules. To achieve statistical precision in a limited measurement period requires high count rates.

In the short term, significant improvements in count rates may be achieved by employing a horizontal focusing monochromator with an energy resolution matched to the detector resolution. This device has two advantages over a flat monochromator: firstly, for the same Bragg angle, this device can accept a wider incident beam and therefore offers an increase in the monochromated beam intensity and secondly, this beam will be focussed thereby easing limitations imposed by the sample size.

The improvements in count rates that should evolve will facilitate the study of other ferromagnets with relatively few unpaired electron spins such as nickel $(0.7\mu_B)$ and iron-nickel alloy $(\sim 1\mu_B)$. More importantly, it will be possible to interpret the separation of the majority and minority spin contributions on a quantitative basis, thus providing a fine test of band theory.

In the long term, improvements in the resolution are necessary if magnet Compton experiments are to provide detailed information about the spin density distribution complementary to the information extracted in neutron diffraction experiments. As mentioned earlier, significant improvements in resolution are possible with focusing optics. However, such a device would require a flux of CPSR orders of magnitude better than presently obtained by the inclined view method ($\sim 10^9$photons s^{-1} mrad^{-2} mm^2 0.1%bandwidth). A helical wiggler with a brightness of 10^{13}photons s^{-1} mrad^{-2} mm^{-2} 0.1% bandwidth delivering a beam of predominantly CPR is presently being installed at the photon factory (Kawata, 1988). Such a device would render focusing optics practicable.

Magnetic Compton scattering is still in its infancy but with improvements in statistical accuracy and resolution the technique will mature to provide a critical test of band theories which in time may more than equal neutron scattering studies.

REFERENCES

Aikala, O., 1982, Phys. Stat. Sol. (b), **110**, K107.

Harlas, A. D., Rueckner, W. and Wellenstein, H. F., 1977, Phil. Mag., **36**, 201.

Bauer, G. E. W., 1984, Phys. Rev. **B30**, 1010.

Bauer, G. E. W., Schneider, J. R. and Welter, J., 1984, Phys. Letts., **100A**, 207.

Benedek, R., Prasad, R., Manninen, S., Sharma, B. K., Bansil, A. and Mijnarends, P. E., 1985, Phys. Rev., **B32**, 7650.

Berko, S., 1967 in Positron Annihilation, ed., Stewart, A. T., Academic Press, New York.

Bhatt, G., Grotch, H., Kazes, E. and Owen, D. A., 1983, Phys. Rev., **A28**, 2195.

Biedenharn, L. C., Rose, M. E. and Arfken, G. B., 1951, Phys. Rev., **83**, 683.

Biggs, F., Mendelsohn, L. B. and Mann, J. B., 1975, Atomic Data and Nuclear Data Tables, **16**, 201.

Bloch, B. J. and Mendelsohn, L. B., 1974, Phys. Rev., **A9**, 129.

Blume, M. and Gibbs, D., 1988, Phys. Rev. **B37**, 1779.

Bohr, J., Gibbs, D., Moncton, D. E. and D'Amico, K. L., 1986, Physica, **140A**, 349.

Brunel, M. and De Bergevin, M., 1981, Acta. Cryst., **A37**, 324.

Brunel, M., Patrat, G., De Bergevin, F, Rousseaux, F. and Lemmonier, M., 1983, Acta. Cryst., **A39**, 84.

Cardwell, D. A., 1987, Ph. D. Thesis, University of Warwick, England.

Cardwell, D. A. and Cooper, M. J., 1986, Phil. Mag., **B54**, 37.

Cardwell, D. A., Cooper, M. J. and Wakoh, S., 1989, J. Phys. condens. matt., **1**, 541.

Chaddah, P. and Sahni, V. C., 1978, Phil. Mag., **B37**, 305.

Christensen, N. E., Sapathy, S. and Pawlowska, Z., 1986, Phys. Rev., **B34**, 5977.

Compton, A. H., 1923, Phys. Rev., **21**, 201.

Cooper, M. J., 1985, Rep. Prog. Phys., **48**, 415.

Cooper, M. J., 1989, Proceedings of Workshop on Momentum Distributions, ed. by Silver and Sokol, to be published by Plenum.

Cooper, M. J., Collins, S. P., Timms, D. N., Brahmia, A., Kane, P. P., Holt, R. S. and Laundy, D., 1988, Nature, **333**, 151.

Cooper, M. J., Laundy, D., Cardwell, D. A., Timms, D. N., Holt, R. S. and Clark, G., 1986, Phys. Rev., **B34**, 5984.

Cooper, M. J., Pattison, P., Williams, B. and Pandey, K. C., 1974, Phil. Mag., **29**, 1237.

Cracknell, A. P. and Wong, K. C., 1973, The Fermi Surface, publ. Oxford University Press.

Crangle, J. and Hallam, G. C., 1963, Proc. R. Soc., London Ser., **A272**, 119.

Currat, R. De Cicco, P. D. and Kaplow, R., 1971, Phys. Rev., **B3**, 243.

Currat, R, De Cicco, P. D. and Weiss, R. J., 1971, Phys. Rev., **B4**, 4256.

De Bergevin, F. and Brunel, M., 1972, Phys. Letts., **A39**, 141.

De Bergevin, F. and Brunel, M., 1981, Acta. Cryst., **A37**, 314.

Diana, M. and Mazzone, G., 1974, Phys. Rev, **B9**, 3898.

Dumond, J. W. M., 1929, Phys. Rev., **33**, 643.

Dupré, F., Menzinger, F. and Saccetti, F., 1981, J. Phys., **F11**, 2179.

Eisenberger, P. and Platzman, P. M., 1970, Phys. Rev., **A2**, 415.

Eisenberger, P. and Reed, W. A., 1972, Phys. Rev., **A2**, 415.

Eisenberger, P. and Reed, W. A., 1974, Phys. Rev., **A9**, 3237.

Felsteiner, J. Pattison, P and Cooper, M. J., 1974, Phil. Mag., **30**, 537.

Franz, W., 1938, Ann. der Physik, **33**, 689.

Gasiorowicz, S., 1974, Quantum Physics, Wiley Publ., New York.

Gell-Mann, M. and Goldberger, M. L., 1954, Phys. Rev., **96**, 1433.

Gibbs, D., Bohr, J. Axe, J. D., Moncton, D. E. and D'Amico, K. L., 1986, Phys. Rev., **B34**, 8182.

Gibbs, D. Harshman, D. R., Isaacs, E. D., Mc Whan, D. B., Mills, D. and Vettier, C., 1988, submitted to Phys. Rev. Letts.

Gibbs, D., Moncton, D. E. and D'Amico, K. L., 1985, J. Appl. Phys., **57**, 3619.

Gibbs, D., Moncton, D. E., D'Amico, K. L., Bohr, J. and Grier, B. H., 1985, Phys. Rev. Letts., **55**, 234.

Gold, A. V., Hodges, L., Panousis, P. T. and Stone, D. R., 1971, Intern. J. Mag., **2**,357.

Golovchenko, J. A., Kincaid, B. M., Levesque, R. A., Meixner, A. E. and Kaplan, D. R., 1986, Phys. Rev. Letts., **57**, 202.

Greaves, G. N., Bennett, R., Duke, P. J., Holt, R. S. and Suller, V. P., 1983, Nucl. Inst. Meths., **208**, 139.

Grotch, H., Kazes, E., Bhatt, G. and Owen, D. A., 1983, Phys. Rev., **A27**, 243.

Gunst, S. B. and Page, L. A., 1953, Phys. Rev., **92**, 970.

Hannon, J. P., Trammell, G. T., Blume, M. and Gibbs, D., 1988, submitted to Phys. Rev. Letts..

Hansen, N. K., Pattison, P. and Schneider, J. R., 1987, Z. Phys. B, cond. mat., **66**, 305.

Hecht, E. and Zajac, A., 1974, Optics, Addison-Wesley Publishing Company.

Heinzmann, U., Schafers, F. and Hess, B. A., 1980, Chem. Phys. Letts., **69**, 284.

Hohenberg, P. and Kohn, W., 1964, Phys. Rev. **136**, B864.

Holland, D. M. P., 1986, submitted to Phys. Scripta.

Holt, R. S., 1979, Ph. D. Thesis, University of Warwick, England.

Holt, R. S. and Cooper. M. J., 1983, Nucl. Inst. Meths., **213**, 447.

Holt, R. S., Cooper, M. J., Du Bard, J. L., Forsyth, J. B., Jones, T. L. and Knights, K., 1979, J. Phys., **E12**, 1148.

Holt, R. S., Laundy, D., Cardwell, D. A., Cooper, M. J., Naylor, T., Manninen, S. and Hatton, P., 1986, Nucl. Instr. Meths., **A243**, 608.

Itoh, F., Cooper, M. J., Holt, R. S., Laundy, D., Cardwell, D. A and Kawamiya, N., 1984, Phil. Mag., **A50**, 703.

Itoh, F., Sakura, M., Sugawa, T., Suzuki, K., Sakai, N., Itoh, M., Mao, O., Shiotani, N., Tanaka, Y., Sakurai, Y., Kawata, H., Nanao, S., Amemiya, Y. and Ando, M., 1988, in print, Nucl. Instr. Meths..

Jauch, J. M. and Rohrlich, F., 1955, Theory of Photons and Electrons, Addison-Wesley Publ., Cambridge, Massachusetts.

Jauncey, C. E. M., 1925, Phys. Rev., **25**, 723.

Johnson, D. D., Pinski, F. J. and Staunton, J. B., 1987, J. Appl. Phys., **61**, 3715.

Kaline, E., 1974, J. Phys., **F4**, 167.

Kawata, H., 1988, Proc. of workshop on applications of high energy x-ray scattering at the ESRF, Grenoble, edited by A. K. Freund.

Klein, O. and Nishina, Y., 1929, Z. Physik, **52**, 853.

Kim, K. J., in X-ray Data Booklet, ed. Vaughan, U. S. Dep. of Energy.

Kittel, C., 1976, Introduction to Solid State Physics, Wiley Publishers, New York.

Kohn, W. and Sham, L. J., 1965, Phys. Rev., **140**, A1133.

Kubo, Y. and Wakoh, S., 1983, Rep. of Univ. Lib. and Inf. Sci., **2**, 11.

Kubo, Y. and Yamishita, J., 1986, J. Phys., **F16**, 2017.

Landau, L. P. and Lifshitz, E. M., 1982, Course of Theoretical Physics, **2**, 2nd edn. by Berestetskii, V. B., Lifshitz, E. M and Pitaevskii, L. P., Oxford:Pergamon.

Lasser, R., Lengeler, B and Arnold, G., 1980, Phys. Rev., **B22**, 663.

Lederer, C. M., Hollander, J. M. and Perlman, I., 1967, Table of Isotopes, 6th ed., Wiley Publ., New York.

Lipps, E. W. and Tolhoek, H. A., 1954, Physica, **20**, (a) 85 and (b) 395.

Lock, D. G., Crisp, V. H. C. and West, R. N., 1973, J. Phys., **F3**, 561.

Loupias, G., Chomilier, J. and Guerard, D., 1984, Physique Lett., **45**, L301.

Loupias, G. and Petiau, J., 1980, J. Physique, **41**, 205.

Lovesey, S. W., 1986, Theory of Neutron Scattering from Condensed Matter, **2**, Oxford University Press.

Lovesey, S. W., 1987, J. Phys., **C20**, 5625.

Low, F. E., 1954, Phys. Rev., **96**, 1428.

Mac Kay, J. S., 1987, SERC Daresbury Lab. Int. Rep., srs/apn/87/83.

Manninen, S., Cooper, M. J and Cardwell, D. A., 1986, Nucl. Instr. Meths., **A245**, 485.

Manninen, S., Hamalainen, K., Paakkari, T. and Suortti, P., 1987, J. de Physique, **69**, 823.

Manninen, S., Paakkari, T. and Kajantie, K., 1974, Phil. Mag., **29**, 167.

Manninen, S., Sharma, B. K., Paakkari, T., Rundquist, S. and Richardson, M. W., 1981, Phys. Stat, Sol. (b), **107**, 749.

Manninen, S., Suortti, P., Cooper, M. J., Chromilier, J. and Loupias, G., 1986, Phys. Rev., **B34**, 8351.

Matsushita, T. and Hashizume, H., 1983, in Handbook on Synchrotron Radiation, ed. Koch, E-E., N. Holl. Publ., New York.

Mc Master, M. H., 1961, Rev. Mod. Phys., **38**, 8.

Mendelsohn, L. B., 1978, private communication to M. J. Cooper. Mendelsohn, L. B. and Biggs, E. A., 1973, U. S. Atomic Energy Conf. 720404, **3**, 1142.

Mendelsohn, L. B., Biggs, F. and Mann, J. B., 1974, Chem. Phys. Letts., 26, 521.

Mendelsohn, L. B., Biggs, F. and Mann, J. B., 1974, Int J. Quan. Chem, **7**, 395.

Mendelsohn, L. B. and Bloch, B. J., 1975, Phys. Rev., **A12**, 551.

Mendelsohn, L. B., Bloch, B. J. and Smith, V. H. jr., 1973, Phys. Rev. Lett., **31**, 1036.

Mijnarends, P. E., 1973, Physica, **63**, 248.

Mills, D. M., 1988, Phys. Rev., **B36**, 6178.

Moncton, D. E., Gibbs, D and Bohr, J., 1986, Nucl. Inst. Meths., **A246**, 839.

Nageswar Rao, M., Mohapatra, D. P., Panda, B. K. and Padhi, H. C., 1985, Sol. Stat. Comm., **55**, 241.

Nara, H., Shindo, K. and Kobayashi, T., 1979, J. Phys. Soc. Japan, **46**, 77.

Ono, F., 1979, J. Phys. Soc. Japan, **47**, 1480.

Paakkari, T. and Manninen, S., 1974, J. Phys., **F4**, L133.

Pandey, K. C., 1973, Bull. Am. Phys. Soc., **18**, 323.

Pattison, P., Bleif, H J. and Schneider, J. R., 1981, J. Phys., **E14**, 95.

Pattison, P., Hansen, N. K. and Schneider, J. R., 1981, Chem. Phys, **59**, 231.

Pattison, P. and Schneider, J. R., 1978, Sol. Stat. Comm., **28**, 581.

Pattison, P. and Schneider, J. R., 1979, J. Phys., **B12**, 4013.

Pattison, P. and Weyrich, W., 1979, J. Phys. Chem. Solids, **40**, 213.

Pattison, P., Weyrich, W. and Williams, B. G., 1977, Sol. Stat. Comm., **21**, 967.

Phillips, W. C. and Weiss, R. J., 1968, Phys. Rev., **120**, 790.

Platzman, P. M., 1972, Comments on S. S. Physics, **4**, 85.

Platzman, P. M. and Tzoar, N., 1970, Phys. Rev., **D2**, 3556.

Platzman, P. M. and Tzoar, N., 1985, J. Appl. Phys., **57**, 3623.

Podloucky, R. and Neckel, A.a 1979, Phys. Stat. Sol. (b), **95**, 541.

Poulter, J. and Staunton, J. B., 1988, J. Phys., **F18**, 1877.

Reed, W. A. and Eisenberger, P., 1972, Phys. Rev., **B6**, 4596.

Reed, W. A., Eisenberger, P., Pandey, K. C. and Snyder, L. C., 1974, Phys. Rev., **B10**, 1507.

Rennert, P., Carl, G. and Hergert, W., 1983, Phys. Stat. Sol., **120**, 273.

Ribberfors, R., 1975, Phys. Rev., **B12**, (a) 2067, (b) 3136.

Rollason, A. J., 1984, Ph. D. Thesis, University of Warwick, England.

Rollason, A. J., Holt, R. S. and Cooper, M. J., 1983, J. Phys., **F13**, 1807.

Rollason, A. J., Schneider, J. R., Laundy, D., Holt, R. S. and Cooper, M. J., 1987, J. Phys., **F 17**, 1105.

Sakai, N., 1987, J. Phys. Soc, Japan, **56**, 2477.

Sakai, N. and Ono, K., 1976, Phys. Rev. Letts., **37**, 351.

Sakai, N. and Ono, K., 1977, J. Phys. Soc. Japan, **42**, 770.

Sakai, N. and Sekizawa, H., 1987, Phys. Rev., **B36**, 2164.

Sakai, N, Shiotani, N., Ito, M., Ito, H. F., Sakurai, M, Sugawa, T. Kawata, H., Amemiya, Y. and Ando, M., 1988, proceeds of Sagamore X, Portugal Phys., in print.

Sakai, N., Terashima, O. and Sekizawa, H., 1984, Nucl. Instr Meths., **221**, 419.

Schülke, W., 1977, Phys. Stat. Sol. (b), **82**, 229.

Schülke, W., 1986, Nucl. Inst. Meths., **A246**, 491.

Schütz, G., Wagner, W., Wilhelm, W., Kienle, P., Zeller, R., Frahm, R. and Materlik, G., 1987, Phys. Rev. Letts., **58**, 737.

Seth, A. and Ellis, D.E., 1977, J. Phys., **C10**, 181.

Shull, C. G. and Mook, H. A., 1966, Phys. Rev. Lett., **16**, 184.

Shull, C. G. and Yamada, Y., 1962, J. Phys. Soc. Japan, **17**, 1.

Simon, T. and Daniel, H., 1977, Phys. Rev., **A15**, 1015.

Tawil, R. A. and Callaway, J., 1973, Phys. Rev., **B7**, 4242.

Timms, D. N., Brahmia, A., Collins, P., Collins, S. P., Cooper, M. J., Holt, R. S., Kane, P. P., Clark, G. and Laundy, D., 1988, J. Phys., **F18**, 157.

Tolhoek, H. A., 1956, Rev. Mod. Phys., **28**, 277.

Tomboulian, D. H. and Hartman, P. L., 1956, Phys. Rev. **102**, 1423.

Trebble, R. S., Craik, D. J., 1969, Magnetic Materials, publ. Wiley Interscience, London.

Vettier, C., Mc Whan, D. B., Gyorgy, E. M., Kwo, T., Buntschuh, B. M. and Batterman, B.

W., 1986, Phys. Rev. Letts., **56**, 757.

Wakoh, S. and Kubo, Y., 1977 J. Magn. Magn. Mater., **5**, 202.

Wakoh, S. and Matsumoto, M., 1988 private communication to M. J. Cooper.

Wakoh, S. and Yamishita, J., 1966, J. Phys. Soc. Japan, **21**, 1712.

Wang, C. S. and Callaway. J., 1975, Phys. Rev., **B11**, 2417.

Wepfer, G. G., Euwema, R. N., Surrat, G. T. and Wilhite, D. L., 1974, Phys. Rev., **B9**, 2670.

Weiss, R. J., 1975, Phil Mag., **32**, 247.

Weiss, R. J., Cooper, M. J. and Holt, R. S., 1977, Phil. Mag, **36**, 193.

Williams, B. G. (editor), 1977, Compton Scattering, Mc Graw Hill Publ., U. K..

Appendix A

From equation 1.30, the scattering cross section may be written,

$$\frac{d\sigma}{d\Omega} = \frac{r_0^2}{2} Tr(\mathbf{I} + \mathbf{P}.\hat{\sigma})(\bar{\beta}^*\mathbf{I} + \bar{\alpha}^*.\hat{\sigma})(\hat{\beta}\mathbf{I} + \hat{\alpha}.\hat{\sigma}), \qquad (A.1)$$

expanding gives,

$$= \frac{r_0^2}{2} Tr(\mathbf{I} + \mathbf{P}.\hat{\sigma})(\bar{\beta}^*\hat{\beta} + \bar{\beta}^*\hat{\alpha}.\hat{\sigma} + \bar{\alpha}^*.\hat{\sigma}\hat{\beta} + \bar{\alpha}^*.\hat{\sigma}\hat{\alpha}.\hat{\sigma}) \qquad (A.2)$$

As the trace operates only on the polarisation states i.e. $\mathbf{I}$ and $\hat{\sigma}$, the trace operations may be performed using the following properties of the Pauli matrices (see Lovesey, 1986 for a description of these properties),

1. $Tr\hat{\sigma} = 0$

2. $Tr(\mathbf{I}) = 2$

3. $Tr\hat{\sigma}_1\hat{\sigma}_2 = 2\delta_{1,2}$

4. $Tr\hat{\sigma}_1\hat{\sigma}_2\hat{\sigma}_3 = 2i x^{1,2,3}$, where $x^{1,2,3} = \begin{cases} +1 & \text{if } 1,2 \text{ and } 3 \text{ are in cyclic order.} \\ -1 & \text{if } 1,2 \text{ and } 3 \text{ are not in cyclic order.} \\ 0 & \text{otherwise.} \end{cases}$

Treating each term in equation A2 separately, the trace operations may be performed using the properties of $\hat{\sigma}$ given above, i.e.

- $Tr(\mathbf{I}\bar{\beta}^*\hat{\beta}) = 2\bar{\beta}^*\bar{\beta}$.

- $Tr(\mathbf{I}\bar{\beta}^*\bar{\alpha}.\hat{\sigma}) = \bar{\beta}^*\bar{\alpha}.Tr\hat{\sigma} = 0$.

- $Tr1\tilde{\alpha}^*.\tilde{\partial}\tilde{\beta} = \tilde{\alpha}^*.Tr\tilde{\partial}\tilde{\beta} = 0.$

- $Tr1\tilde{\alpha}_1^*.\tilde{\sigma}_1\tilde{\alpha}_2.\tilde{\sigma}_2 = \sum_{1,2}\alpha_1^*\alpha_2^*Tr1\sigma_1\sigma_2 = 2Tr\delta_{1,2}1 = 2\tilde{\alpha}.\tilde{\alpha}^*.$

- $Tr(\mathbf{P}.\tilde{\partial})(\tilde{\beta}^*\tilde{\beta}) = 0.$

- $Tr(\mathbf{P}.\tilde{\partial})(\tilde{\beta}^*\tilde{\alpha}.\tilde{\partial}) = \sum_{1,2}P_1\beta^*\alpha_2 Tr\sigma_1\sigma_2 = 2\tilde{\beta}^*(\tilde{\alpha}.\mathbf{P}).$

- $Tr(\mathbf{P}.\tilde{\partial})(\tilde{\alpha}^*.\tilde{\partial}\tilde{\beta}) = \sum_{1,2}P_1\alpha_2^*Tr\sigma_1\sigma_2 = 2(\tilde{\alpha}^*.\mathbf{P})\tilde{\beta}$

- $Tr(\mathbf{P}.\tilde{\alpha})(\tilde{\alpha}^*.\tilde{\partial}\tilde{\alpha}.\tilde{\partial}) = \sum_{1,2,3}P_1\alpha_2^*\alpha_3 Tr\sigma_1\sigma_2\sigma_3 = 2i\mathbf{P}.(\tilde{\alpha}^* \wedge \tilde{\alpha}).$

Summing these terms gives the general form of the scattering cross section (equation 1.31) which is valid for any initial photon polarisation, i.e.

$$\frac{d\sigma}{d\Omega} = r_0^2(\tilde{\alpha}^*.\tilde{\alpha} + \tilde{\beta}^*\tilde{\beta} + \tilde{\beta}^*(\tilde{\alpha}.\mathbf{P}) + (\tilde{\alpha}^*.\mathbf{P})\tilde{\beta} + i\mathbf{P}.\tilde{\alpha}^* \wedge \tilde{\alpha}). \qquad (A.3)$$

Appendix B

The magnetic Compton cross section to order $\frac{\hbar\omega_1}{m_0 c^2}$ can be obtained by substituting the expressions for $\bar{\alpha}$ and $\bar{\beta}$ (equations 1.41–1.44) into the general scattering cross section, equation 1.31. For a circularly polarised photon beam, $P_1 = P_3 = 0$ and P_2 is finite. Consider each term in equation 1.31 individually,

1. $\bar{\alpha}^* \bar{\alpha} = \bar{\alpha}_1^* \bar{\alpha}_1 + \bar{\alpha}_2^* \bar{\alpha}_2 + \bar{\alpha}_3^* \bar{\alpha}_3 = \frac{1}{4}[n(\mathbf{p})(1 - \mathbf{k_1}.\mathbf{k_2})]^2$

2. $\bar{\beta}^* \bar{\beta} = \frac{1}{4}[n(\mathbf{p})(1 + \mathbf{k_1}.\mathbf{k_2})]^2$

3. $\bar{\beta}^*(\bar{\alpha}.\mathbf{P}) = \bar{\beta}^*(\bar{\alpha} P_2) = -\frac{1}{4}\frac{\hbar\omega_1}{m_0 c^2}(1 - \cos\phi)[\mathbf{S}(\mathbf{p}) + \mathbf{L}(\mathbf{p})].(\mathbf{k_1} + \mathbf{k_2})P_2 n(\mathbf{p})(1 + \mathbf{k_1}.\mathbf{k_2})$

4. $(\bar{\alpha}^*.\mathbf{P})\bar{\beta} = (\bar{\alpha}_2^* P_2)\bar{\beta} = -\frac{1}{4}\frac{\hbar\omega_1}{m_0 c^2}(1 - \cos\phi)[\mathbf{S}(\mathbf{p}) + \mathbf{L}(\mathbf{p})].(\mathbf{k_1} + \mathbf{k_2})P_2 n(\mathbf{p})(1 + \mathbf{k_1}.\mathbf{k_2})$

5. $i(\mathbf{P}.\bar{\alpha}^* \wedge \bar{\alpha}) = i P_2(\bar{\alpha}_3^* \bar{\alpha}_1 - \bar{\alpha}_1^* \bar{\alpha}_3) = 2 P_2 n(\mathbf{p})(1 - \mathbf{k_1}.\mathbf{k_2})\mathbf{S}(\mathbf{p}).(\mathbf{k_1} - \mathbf{k_2})$

adding 1. to 5. gives,

$$
\begin{aligned}
\frac{d\sigma}{d\Omega} = {} & \frac{r_0^2 n(\mathbf{p})}{2}(n(\mathbf{p})(1 + (\mathbf{k_1}.\mathbf{k_2})^2) \\
& -\frac{\hbar\omega_1}{m_0 c^2}P_2(1 - \cos\phi)[(1 - \mathbf{k_1}.\mathbf{k_2})\mathbf{S}(\mathbf{p}).(\mathbf{k_1} - \mathbf{k_2}) \\
& -(1 + \mathbf{k_1}.\mathbf{k_2})\mathbf{S}(\mathbf{p}).(\mathbf{k_1} + \mathbf{k_2}) + (1 + \mathbf{k_1}.\mathbf{k_2})\mathbf{L}(\mathbf{p}).(\mathbf{k_1} + \mathbf{k_2})]).
\end{aligned}
\tag{B.1}
$$

This expression may be simplified to leave the magnetic Compton cross section (equation 1.46), i.e.

$$
\begin{aligned}
\frac{d\sigma}{d\Omega} = {} & \frac{r_0^2 n(\mathbf{p})}{2}(n(\mathbf{p})(1 + \cos^2\phi) \\
& -\frac{2\hbar\omega_1}{m_0 c^2}P_2(1 - \cos\phi)[\mathbf{S}(\mathbf{p}).(\mathbf{k_1}\cos\phi + \mathbf{k_2}) \\
& + \cos^2(\phi/2)\mathbf{L}(\mathbf{p}).(\mathbf{k_1} + \mathbf{k_2})])
\end{aligned}
\tag{B.2}
$$

THE BRITISH LIBRARY DOCUMENT SUPPLY CENTRE

TITLE COMPTON SCATTERING STUDIES OF SPIN AND CHARGE

MOMENTUM DENSITIES

AUTHOR David N. Timms

INSTITUTION and DATE University of Warwick 1989

D90080